Disentangling spatiotemporal signals in global atmospheric methane columns

Thesis by
Katherine M. Saad

In Partial Fulfillment of the Requirements for the
degree of
Environmental Science and Engineering

CALIFORNIA INSTITUTE OF TECHNOLOGY
Pasadena, California

2017
Defended February 23, 2017

Katherine M. Saad
ORCID: 0000-0002-2501-6223

ACKNOWLEDGMENTS

I dedicate this dissertation to my family, for instilling in me the seeds of faith, hope, and love, without which I would not have reached this point. Their indefatigable work ethic has been a constant inspiration, especially during my time in graduate school. My parents instilled in me independence, perseverance, and a questioning mind, unknowingly planting the seeds of a scientist, and I am grateful for all they have done to invest in my education. Nardine Saad Riegels has supported me since my earliest research pursuits: picking me up from college and driving me to my field site when I had no other means of getting there; hanging out in a hot, dirty patch of reclaimed wetland filled with roaming cows; and carrying around the archaically heavy laptop that recorded the measurements I was taking. She has cheered me on through academic difficulties and achievements, and in the last sprint towards my defense, her reminder of David's attitude toward Goliath kept me moving forward when I felt overwhelmed and ill-equipped for this undertaking. She and Nick have produced a nephew and niece who have been integral fixtures of my graduate experience: Theo, whose caring and curiosity have buoyed me, and Phoebe, who at the age of two (and more than a half) is already an inspiration as one of the strongest women I know.

I am truly grateful to my advisor, Paul Wennberg—for bringing me to Caltech, for pushing me to stretch outside of my comfort zone, for imparting numerous opportunities to invest in my evolution as a scientist, and for consistently having my back. From him I have learned how to evaluate and improve my work with a critical eye and the importance of distilling every scientific result into a meaningful story. I am a better scientist because of him.

When listing the members of my Thesis Advisory Committee to inquisitive colleagues, I would be immediately told how lucky I was, and I would reply that I could not agree more. Immediately after our first meeting during my prospective visit, I regretted that I was not more interested in monsoon dynamics because of how much I respected Simona Bordoni, and it is kismet that the trajectory of my graduate career led to her as the chair of my committee. Mitchio Okumura's thoughtful engagement and encouragement of interaction with his group have broadened my scientific development. Geoff Toon, who patiently walked through the retrievals with me on a weekly basis, who really approached all of our interactions with a patience and generosity of time from which I continue to benefit. While not on my

committee, Don Blake taught me more about methane than the many hundreds of hours of literature reviews I have spent on the topic, and I also thank him for getting me hooked on aircraft campaigns.

Cohesive despite the divergence of scientific interests, the Wennberg group has been a vibrant and respectful environment. Paul has curated a group of curious, generous, and thoughtful scientists with whom I have enjoyed exchanging ideas: Jacob Hedelius, Alex Teng, Eric Praske, Coleen Roehl, Camille Viatte, Becky Schwantes, Hannah Allen, Kelvin Bates, John Crounse, and the many other members with whom I have had the fortune to overlap. I am especially indebted to Debra Wunch, who has mentored me since I was a random prospective graduate student whom she had to take for coffee, and later when I was a random MIT graduate student sitting across from her at breakfast at the NDACC meeting. I have learned so much from her in our time together at Caltech, and I aspire to emulate the integrity she brings both to her work and her interactions with fellow scientists.

I have been continually amazed at the dedication of Caltech's staff, and Nora Oshima typifies the superhuman ability on which I have come to rely. Without her and Kathy Young, no one in Linde-Robinson would be able to function. I am also grateful to Liz Boyd for helping make the transition to Caltech so smooth, and then doing the same for every academic task thereafter. I have relied on the support and mentorship of Felicia Hunt and Cassandra Horii, and they will perpetually be role models throughout my future endeavors.

In final push towards my defense, the "Last of 2010 Cohort" became a critical support system, and I thank Jennifer Walker, for putting up with my ridiculous quirks and encouraging me to take care of myself, and Wilton Mui, one of the most considerate people I have come to know on this journey. I appreciate the time and energy that Arde Boghossian, Elle Chimiak, Erin-Kate Escobar, Matt Gethers, Magnus Haw, Joe O'Rourke, and Giuliana Viglione have poured into this campus, and me with it. I also thank Sebastian Pineda, who was my most reliable thesis-writing buddy, for being a sounding board and source of moral support.

Having had more than one academic home in my graduate career, I must also thank everyone at MIT who made my first two years of graduate school full of growth. I am grateful for the support of Ron Prinn, my advisor at MIT, and the atmospheric chemistry community there. Eri Saikawa taught me how to run global models with a reserve of patience that I never reached the bottom of, no matter how hard I tried. Ho-Jeong Shin was the best officemate I have ever had; her

encouraging words left for me on our chalk board kept me afloat in turbulent times. A complete list of my peers would be longer than the dissertation itself, so I hope that Emily Zakem, Ben Mandler, Isabela Le Bras, Ruel Jerry, Sarvesh Garimella, Yodit Tewelde, Christopher Kinsley, Helen Feng, Mike Sori, Stephen Messenger, and the countless others know how much the shared joys and tears mean to me. I appreciate the friendship of Robens Joseph and Sparsha Saha while in Cambridge, and I thank Dr. Xiaolu Hsi for her empathy, insight, and compassion.

I have been blessed with an amazing and supportive extended family, who I hope will forgive me for not listing them all by name. I do have to specifically acknowledge my uncle, Youssef Badir, who has treated me like a scholar since my early childhood, for never wavering in his faith in my abilities or this calling. Among my cousins, I am especially grateful to Marian Beshara, for her near-daily texts that always seem to tell me what I need to hear in each moment, for her support in all realms of my life, and for hardly asking for anything from me during a time when I owed her so much. I also need to call out Helena Botros Youssef, for decades of encouragement and unconditional acceptance, as well as her willingness to drop everything and leave the country when I needed a post-qualifying exam break; I am humbled that I remain important to her no matter how full her life becomes. I cannot begin to articulate how indebted I am to Abouna James Solimon, without whose guidance these past four plus years I would have been lost.

ABSTRACT

Methane is a major driver of atmospheric chemistry and a powerful radiative forcing agent. Thus, explaining tropospheric methane trends over the last two decades is critical for the scientific understanding of the global carbon cycle as well as the ability to predict future consequences on the climate and biosphere. Tropospheric concentrations of methane have been increasing, but the growth rate in the last two decades has been extremely variable. Long-term trends in atmospheric methane concentrations and short-term fluctuations in its growth rate are not well understood because its surface emissions and chemical loss are poorly constrained. The ranges of uncertainties for estimates of methane sources and sinks are considerably broad due to the complexity of both natural and anthropogenic fluxes and the heterogeneity of their timescales. This research takes a multifaceted approach to constraining methane fluxes and determining the causes of interannual and long-term variability by developing and synthesizing measurements, integrating methane observations with tracers of tropospheric advection, and assessing systematic biases in chemical transport models.

This work synthesizes satellite, aircraft, and surface measurements, including a newly developed dataset of tropospheric column-averaged dry-air mole fractions from Fourier Transform Spectrometer (FTS) instruments within the Total Carbon Column Observing Network (TCCON), a global ground-based network of Fourier transform spectrometers that produce precise measurements of column-averaged dry-air mole fractions of atmospheric methane. Temporal variability in the total column of methane due to stratospheric dynamics obscures fluctuations and trends driven by tropospheric transport and local surface fluxes that are critical for understanding methane sources and sinks. We reduce the contribution of stratospheric variability from the total column average by subtracting an estimate of the stratospheric methane derived from simultaneous measurements of hydrogen fluoride (HF). HF provides a proxy for stratospheric methane because it is strongly anti-correlated to methane in the stratosphere, has an accurately known tropospheric abundance (of zero), and is measured at most TCCON stations. The stratospheric partial column of methane is calculated as a function of the zonal and annual trends in the relationship between methane and HF in the stratosphere, which we determine from ACE-FTS satellite data. We also explicitly take into account the methane column averaging kernel to estimate the contribution of stratospheric methane to the

total column. The resulting tropospheric methane columns are consistent with in situ aircraft measurements and augment existing observations in the troposphere.

Assimilating measurements into the GEOS-Chem chemical transport model, the sensitivities of the temporal and spatial distributions of methane to changes in the distributions of sources and sinks are evaluated. Conventionally, estimates of methane sources are derived by bridging emissions inventories with atmospheric observations employing chemical transport models. The accuracy of this approach requires correctly simulating advection and chemical loss such that modeled methane concentrations scale with surface fluxes. When total column measurements are assimilated into this framework, modeled stratospheric methane introduces additional potential for error. To evaluate the impact of such errors, we compare TCCON and GEOS-Chem total and tropospheric column-averaged dry-air mole fractions of methane. We find that the model's stratospheric contribution to the total column is insensitive to perturbations to the seasonality or distribution of tropospheric emissions or loss. In the Northern Hemisphere, we identify disagreement between the measured and modeled stratospheric contribution, which increases as the tropopause altitude decreases, and a temporal phase lag in the model's tropospheric seasonality driven by transport errors. Within the context of GEOS-Chem, we find that the errors in tropospheric advection partially compensate for the stratospheric methane errors, masking inconsistencies between the modeled and measured tropospheric methane. These seasonally varying errors alias into source attributions resulting from model inversions. In particular, we suggest that the tropospheric phase lag error leads to large misdiagnoses of wetland emissions in the high latitudes of the Northern Hemisphere.

This work also investigates the influence of large-scale transport to the spatial distribution, and in particular the meridional gradients, of methane. The surface origins of air parcels and the long-lived trace gases they transport are difficult to discern solely from the meridional gradient defined using latitude. Instead, we evaluate the meridional gradients of tropospheric methane using potential temperature at 700 hPa (θ_{700}) as a dynamical tracer of synoptic-scale transport. We demonstrate that tropospheric methane variability in θ_{700} tracer space captures part of the influence of advection on horizontal methane gradients and, thus, better represents the geospatial distribution of fluxes than geographical location. We find that the summertime meridional gradient of tropospheric methane is relatively constant in the Southern Hemisphere, and the Northern Hemisphere gradient has become weaker in

the past decade, reducing the divide between the mid-latitudes and subtropics. This shift in the gradient indicates that either methane emissions have been increasing or the hydroxyl radical has been decreasing in the Northern extratropics. The signal of the shifting meridional gradients tracking the increased global growth rate requires that any proposed solution to this problem must explain both trends. Unfortunately, model dynamics are currently insufficient to evaluate various explanations with adequate confidence. This dynamical tracer approach would be substantially improved with denser spatial coverage of column measurements. Additional remote sensing measurements that can resolve zonal gradients and disentangle the problems of model covariance will be critical to conclusively determining drivers of tropospheric methane distributions, and thus trends.

PUBLISHED CONTENT AND CONTRIBUTIONS

Saad, K. M., et al. 2016. "Seasonal variability of stratospheric methane: implications for constraining tropospheric methane budgets using total column observations." *Atmospheric Chemistry and Physics* 16 (21): 14003–14024.

Chapter 2 includes Appendix A of and Chapter 3 is adapted from this journal article. K.M.S. participated in the conception of the project, prepared the data, ran the model simulations, derived or participated in the derivation of several of the analytical equations, and wrote the manuscript with input from co-authors. doi:10.5194/acp-16-14003-2016. http://www.atmos-chem-phys.net/16/14003/2016/.

Saad, K. M., et al. 2014. "Derivation of tropospheric methane from TCCON CH_4 and HF total column observations." *Atmospheric Measurement Techniques* 7 (9): 2907–2918.

Chapter 2 is adapted from this journal article. K.M.S. participated in the development of the methodology, derived or participated in the derivation of several of the analytical equations, implemented the methodology, prepared the data, and wrote the manuscript with input from co-authors. doi:10.5194/amt-7-2907-2014. http://www.atmos-meas-tech.net/7/2907/2014/.

CONTENTS

LIST OF FIGURES

LIST OF TABLES

Chapter 1

INTRODUCTION

The history of the scholarship of atmospheric methane (CH_4) is inextricably linked to ground-based remotely-sensed spectroscopic measurements. CH_4's existence in Earth's atmosphere was first detected in the $3.3\mu m$ infrared region of the solar spectra (Migeotte 1948b). Within a few months, comparisons with column retrievals at other observation sites around the United States confirmed that "there are reasons to believe that the detected methane is not due to a local impurity of the atmosphere" (Migeotte 1948a). Shortly thereafter, McMath et al. (1949) calculated the first CH_4 slant column, 1.83×10^{20} molec cm^{-2}, and estimated an atmospheric abundance by mass of 1.2 parts per million (equal to a mole fraction of 2.1 ppm, assuming a dry air mass). Less than a year after Migeotte's unexpected discovery, several other scientists published their CH_4 measurements from ground-based spectrometers across the United States and Europe (Goldberg 1951), confirming that CH_4 was well-mixed enough that its abundance was equivalent globally—at least in the 10° zonal band encompassing the instruments. Further analysis led to the determination that a nearly uniform vertical distribution with higher concentrations near the surface best explained the spectral fits (Goldberg and Müller 1953).

While the accuracy of column measurements have improved—the initial estimates are nearly double the 1.1 ppm_v (hereafter ppm), determined from ice core samples by MacFarling Meure et al. (2006) for that time period—the characterization of CH_4 using remote sensing established a legacy that continues until now. While column measurements of CH_4 are certainly not only the oldest means of understanding its atmospheric abundance, the scientific knowledge of the spatial gradients of CH_4 established by this patchwork of ground-based measurements has fundamentally shaped our understanding of the behavior of CH_4 in the atmosphere. In this tradition, this dissertation presents a dataset of tropospheric CH_4 columns retrieved from Fourier Transform Spectrometer (FTS) instruments to strengthen observational constraints of CH_4, demonstrates the ways in which model biases can alter our understanding of CH_4 trends, and investigates the influence of large-scale advection to the spatial distribution of CH_4.

1.1 Temporal Variability in Atmospheric Methane

CH_4 has surprised the scientific community since the first time it was measured in the atmosphere. Until the early 1980s, CH_4 was thought to be in steady state in the atmosphere (c.f., Ehhalt 1974; Wofsy 1976). The consensus around CH_4 concentrations was such that when the graduate students of future Nobel laureate F. Sherwood Rowland told him that their measurements indicated a steady increase in August of 1980, his response was a firm, "Everyone knows the concentration of methane is stable in the atmosphere" (D.R. Blake, personal communication). However, a cascade of publications arguing just that soon entered the scientific literature. The scientific activity around the determination that atmospheric CH_4 concentrations have been increasing was analogous to that of its discovery: the earliest publication reporting the increase used equally cautious language around whether the signal represented a local anomaly or a global trend (Graedel and McRae 1980); several independent measurements using the same instrumentational approach (in this case, flame ionization gas chromatography) quickly confirmed the original discovery (Rasmussen and Khalil 1981b; Rasmussen and Khalil 1981a; Blake et al. 1982); and it accompanied a focus within the scientific community on constraining the spatial gradients of CH_4 in the atmosphere (Fraser et al. 1981; Mayer et al. 1982) and characterizing its sources and sinks (e.g., Cicerone et al. 1983; Keller et al. 1983; Khalil and Rasmussen 1983; Rasmussen and Khalil 1983; Khalil and Rasmussen 1985). In the intermediate 30 years, however, the precision and accuracy of the measurements had improved greatly, which, coupled with greater temporal frequency, allowed both the long-term trend and the seasonal cycle of tropospheric CH_4 to be characterized (Rasmussen and Khalil 1981a; Khalil and Rasmussen 1983). Moreover, the sources and sinks of CH_4 had been identified as primarily terrestrial emissions at the surface and chemical reaction by the hydroxyl radical (OH) in the troposphere, respectively (Bates and Witherspoon 1952; Ehhalt 1974; Ehhalt and Schmidt 1978; Khalil and Rasmussen 1985).

Within the last three centuries, tropospheric concentrations have more than doubled (Rasmussen and Khalil 1984), from about 700 ppb in 1750 (MacFarling Meure et al. 2006) to the current level of 1850 ppb (Figure 1.1, top). The growth rate had been slowing (Figure 1.1, bottom), from an annual increase of 52 ppb (3.3%) in the late 1970s (Blake et al. 1982) to an average increase of 16 ppb (1.1%) through the late 1980s (Blake and Rowland 1988), reaching the first reported negative growth rate in 2000 (Simpson et al. 2002). After becoming negative at several points since (Rigby et al. 2008; Dlugokencky et al. 2009), the growth rate began to increase

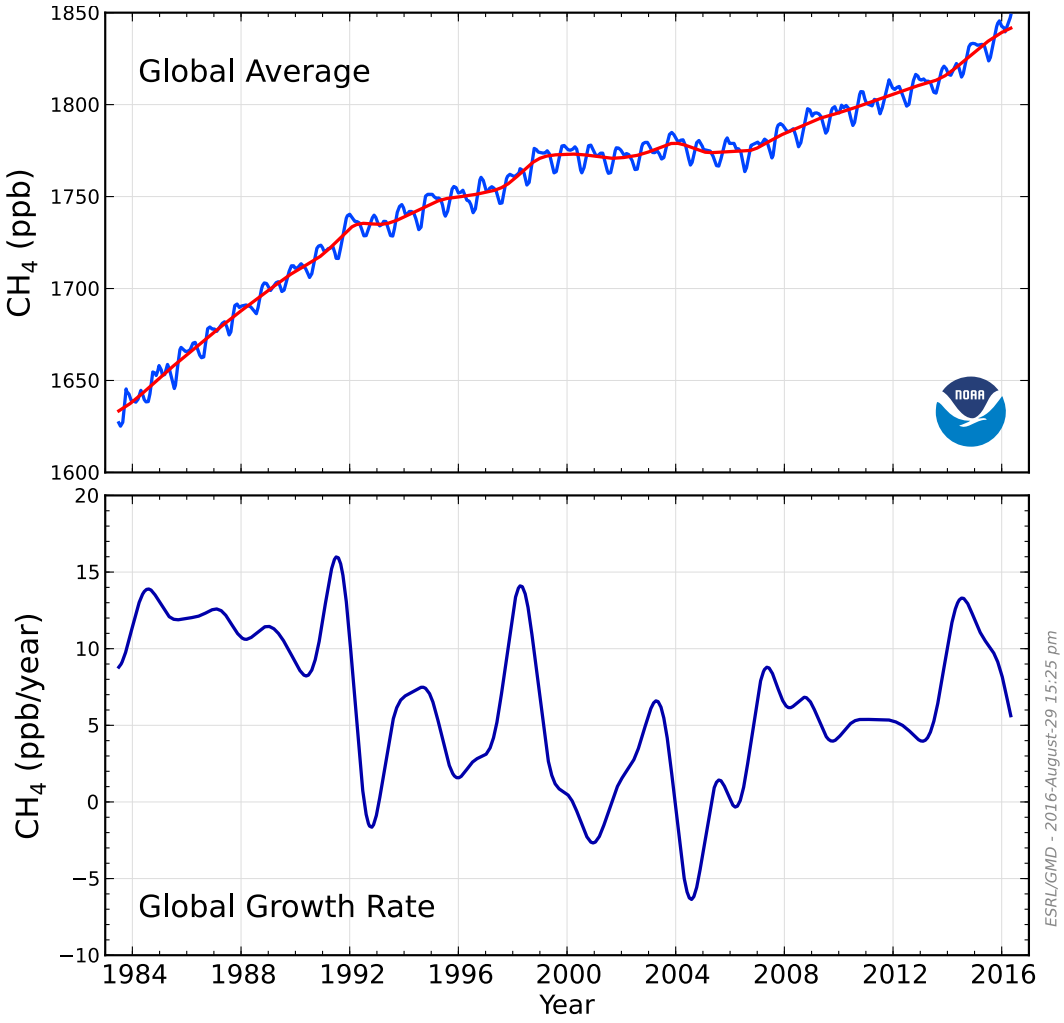

Figure 1.1: Globally averaged CH_4 mole fractions (top, blue line) and their long-term trend (top, red line), and the associated globally averaged growth rate (bottom), from monthly mean National Oceanic and Atmospheric Administration (NOAA) Earth System Research Laboratory (ESRL) Global Monitoring Division in situ surface measurements. (Image courtesy of NOAA ESRL Carbon Cycle/E. Dlugokencky, https://www.esrl.noaa.gov/gmd/ccgg/.)

again (Sussmann et al. 2012), peaking at almost 13 ppb per year in 2014, the highest level in nearly two decades (Figure 1.1, bottom). The global growth rate is notably variable on interannual time scales, a signal of the sensitivity of CH_4 to rapid, short-lived fluctuations in sources and sinks.

The scientific community is divided on which CH_4 fluxes have been driving these annual and decadal trends, partly due to the large number of both natural and anthropogenic biogenic and thermogenic processes that emit CH_4 (c.f., Ciais et al. 2013). Natural sources include wetlands (Tyler et al. 1987; Crozier et al. 1995; Wang et

al. 1996), oceans (Lamontagne et al. 1973), hydrates and termites (Rasmussen and Khalil 1983). Anthropogenic sources are comprised of fossil fuel extraction and processing (Bates and Witherspoon 1952), landfills and waste treatment, ruminants (Crutzen et al. 1986), rice agriculture (Cicerone et al. 1983) and biomass burning (Crutzen et al. 1979). CH_4 oxidation in the troposphere by OH accounts for around 85% of the global CH_4 sink, with soil uptake (Keller et al. 1983) and stratospheric oxidation making up the remaining 15% (Hartmann et al. 2013). As Table 1.1 illustrates, the estimates of both emissions and sinks are quite uncertain. Natural sources such as wetlands and hydrates can vary greatly in their CH_4 production geographically and from year to year. Fossil emissions also can exhibit large spatial variance over the fuel trajectory of extraction, production, processing, and distribution. Other major anthropogenic emitters, such as landfills and waste treatment, ruminants, rice agriculture, and biomass burning, are biogenic and can thus be difficult to distinguish from natural sources. Due to the disperse distribution of tropospheric sources of comparable magnitude, as well as the complicated temporal characteristics of the CH_4 cycle, the scientific understanding of the relative strengths of the processes that govern CH_4 fluxes is unconstrained, particularly at the regional level (Hartmann et al. 2013).

Much of the focus has been on attempting to explain recent fluctuations in CH_4 concentrations, especially the "renewed growth" in the last decade. The primary approach in the scientific literature combines bottom-up estimates, such as those based on surface flux measurements at specific sites and national economic data, with top-down estimates based on background CH_4 concentrations measured by global measurement networks. Studies that aim to establish which emission sources have produced observed variability in the CH_4 growth rate disagree due to the large number of both natural and anthropogenic biogenic and energy-related processes, which vary on different temporal and spatial scales. As a result, estimates of how natural and anthropogenic activities contribute to CH_4 concentrations remain uncertain.

1.2 Motivation for Constraining Methane Emissions

Explaining tropospheric CH_4 trends over the last two decades is critical for the scientific understanding of the global carbon cycle as well as the ability to predict future consequences on the climate and biosphere. The most abundant hydrocarbon in the atmosphere, CH_4 is a significant radiatively absorptive gas, with a greenhouse warming potential more than 20 times that of carbon dioxide (CO_2). The doubling

Table 1.1: Estimated global emissions of CH_4 and 68% confidence intervals ($TgCH_4\ yr^{-1}$), adapted from Ciais et al. (2013).

	1980-1989		1990-1999		2000-2009	
	Top-Down	Bottom-Up	Top-Down	Bottom-Up	Top-Down	Bottom-Up
Natural Sources	193 [150-267]	355 [244-466]	182 [167-197]	336 [230-465]	218 [179-273]	347 [238-484]
Natural wetlands	157 [115-231][1,2,3]	225 [183-266][4,5]	150 [144-160][1,28,29]	206 [169-265][4,5,27]	175 [142-208][1,29,33-36]	217 [177-284][4,5,27]
Other sources	36 [35-36][1,2]	130 [61-200]	32 [23-37][1,28,29]	130 [61-200]	43 [37-65][1,29,33-36]	130 [61-200]
Freshwater lakes & rivers		40 [8-73][6-8]		40 [8-73][6-8]		40 [8-73][6-8]
Wild animals		15 [15-15][9]		15 [15-15][9]		15 [15-15][9]
Wildfires		3 [1-5][9-13]		3 [1-5][9-13]		3 [1-5][9-13]
Termites		11 [2-22][9,10,14,15]		11 [2-22][9,10,14,15]		11 [2-22][9,10,14,15]
Geological & Oceans		54 [33-75][10,16,17]		54 [33-75][10,16,17]		54 [33-75][10,16,17]
Hydrates		6 [2-9][9,18,19]		6 [2-9][9,18,19]		6 [2-9][9,18,19]
Permafrost[a]		1 [0-1][10]		1 [0-1][10]		1 [0-1][10]
Anthropogenic Sources	348 [305-383]	308 [292-323]	372 [290-453]	313 [281-347]	335 [273-409]	331 [304-368]
Biogenic	208 [187-220][1,2,3]	185 [172-197][20]	239 [180-301][1,28,29]	187 [177-196][20,30,31]	209 [180-241][1,29,33-36]	200 [187-224][20,30,31]
Rice		45 [41-47][20]		35 [32-37][20,27,30,31]		36 [33-40][20,27,30,31]
Ruminants		85 [81-90][20]		87 [82-91][20,30,31]		89 [87-94][20,30,31]
Landfills & waste		55 [50-60][20]		65 [63-68][20,30,31]		75 [67-90][20,30,31]
Fossil fuels	94 [75-108][1,2,3]	89 [89-89][20]	95 [84-107][1,28,29]	84 [66-96][20,30,31]	96 [77-123][1,29,33-36]	96 [85-105][20,30,31]
Biomass burning & Biofuels	46 [43-55][1-3]	34 [31-37][20-22,38]	38 [26-45][1,28,29]	42 [38-45][13,20-22,32,38]	30 [24-45][1,29,33-36]	35 [32-39][13,20,21,32,37,38]
Sources	541 [500-592]	663 [536-789]	554 [529-596]	649 [511-812]	553 [526-569]	678 [542-852]
Sinks	511 [460-559]	567 [420-718]	542 [518-579]	599 [530-668]	550 [514-560]	632 [592-785]
Total chemical loss	490 [450-533][1,2,3]	539 [411-671][23-26]	515 [491-554][1,28,29]	571 [521-621][23-26]	518 [510-538][1,29,33,34,36]	604 [483-738][23-26]
Tropospheric OH		468 [382-567][26]		479 [457-501][26]		528 [454-617][25,26]
Stratospheric OH		46 [16-67][23,25,26]		67 [51-83][23,25,26]		51 [16-84][23,25,26]
Tropospheric Cl		25 [13-37][24]		25 [13-37][24]		25 [13-37][24]
Soils	21 [10-27][1,2,3]	28 [9-47][27,34,36]	27 [27-27][1]	28 [9-47][27,34,36]	32 [26-42][1,33-36]	28 [9-47][27,34,36]

[a] excluding lakes and wetlands [1] Bousquet et al. (2011) [2] Fung et al. (1991a) [3] Hein et al. (1997) [4] Hodson et al. (2011) [5] Ringeval et al. (2011) [6] Bastviken et al. (2004) [7] Bastviken et al. (2011) [8] Walter et al. (2007) [9] Denman et al. (2007) [10] EPA (2010) [11] Hoelzemann et al. (2004) [12] Ito and Penner (2004) [13] van der Werf et al. (2010) [14] Sanderson (1996) [15] Sugimoto et al. (1998) [16] Etiope et al. (2008) [17] Rhee et al. (2009) [18] Dickens (2003) [19] Shakhova et al. (2010) [20] EDGAR4-database (2009) [21] Mieville et al. (2010) [22] Schultz et al. (2007) (excluding biofuels) [23] Neef et al. (2010) [24] Allan et al. (2007) [25] Williams et al. (2012b) [26] Voulgarakis et al. (2013) [27] Spahni et al. (2011) [28] Chen and Prinn (2006) [29] Pison et al. (2009) [30] Dentener et al. (2005) [31] EPA (2011a) [32] van der Werf (2004) [33] Bergamaschi et al. (2009) [34] Curry (2007) [35] Spahni et al. (2011) [36] Ito and Inatomi (2012) [37] Wiedinmyer et al. (2011) [38] Andreae and Merlet (2001) [39] Prather et al. (2012), updated to 2011

of CH_4 from pre-industrial concentrations has contributed an estimated 17% of the radiative forcing from well-mixed greenhouse gases (Myhre et al. 2013). In fact, CH_4 could have an even larger radiative forcing impact than previously thought due to the indirect effect of CH_4-aerosol chemistry (Shindell et al. 2009). Thus, further understanding of the dynamics of CH_4 fluxes would have significant implications for climate change and atmospheric warming.

In addition to its warming potential, atmospheric CH_4 has a significant effect on background tropospheric chemistry, in part due to its relatively large abundance. In high NOx conditions, such as in most urban areas, CH_4 oxidation by the OH radical leads to the formation of the methyl peroxy radical, which then reacts with NO to create NO_2, thereby indirectly producing ozone (O_3). Studies have found that increased anthropogenic CH_4 emissions co-varies linearly with higher O_3 concentrations, especially in the boundary layer, where most of the public health concerns are and where most of the measurements in this research are taken (Fiore et al. 2008). Thus, even if emission growth rates decrease, CH_4 will continue to play an important role in atmospheric chemistry and radiative forcing.

Quantifying CH_4 fluxes also has policy implications. CH_4 emissions are strongly intertwined to human quality of life through food production, fuel processing, waste treatment, and land use, and more robust constraints on CH_4 emissions will not only advance scientific understanding of the global carbon cycle but can also inform decision-making processes for the development of more efficient strategies of meeting the challenges of environmental change. CH_4 is one of the trace gases most likely to be regulated in climate change legislation or international agreements, and currently those regulations are based on an incomplete understanding of the relative contributions of emissions from anthropogenic sources. Globally, energy demand is on the rise, with projections of coal, liquid fuel, and natural gas use to increase by 19, 36, and 74%, respectively, by 2040 (EIA 2016). In addition, ruminant farms and landfills will become more numerous as a result of population growth and the economic expansion of developing countries. Future climate and air quality regulations may set caps and credits based on imprecise determinations of the amount of CH_4 produced by each sector.

1.3 Drivers of Methane Fluxes

The continuity equation describes the rate of change of a given trace gas, *i*, in the atmosphere based on its chemical sources and sinks and advection. For a given

chemical species,

$$\frac{\partial \rho_i}{\partial t} = P_i - L_i - \vec{\nabla} \cdot (\rho_i \vec{v}) \tag{1.1}$$

where ρ_i is the mass concentration of that species, P_i and L_i represent production (in the case of CH_4, emissions) and loss (chemical sinks) respectively, and $\vec{\nabla} \cdot (\rho_i \vec{v})$ is the flux of the trace gas in the zonal, meridional, and vertical directions. If we consider the mass fraction, μ_i as the ratio of ρ_i to the density of the air parcel, we can re-write the continuity equation as

$$\frac{\partial (\mu_i \rho)}{\partial t} + \vec{\nabla} \cdot (\mu_i \rho \vec{v}) = P_i - L_i \tag{1.2}$$

where ρ is the density of air. By neglecting molecular diffusivity and applying conservation of mass, this expression simplifies to

$$\frac{\partial \mu_i}{\partial t} + \vec{v} \cdot \vec{\nabla} \mu_i = \frac{P_i - L_i}{\rho} \tag{1.3}$$

Similarly, the evolution of the mole fraction of CH_4, x_{CH_4}, along a trajectory is proportional to the sources and sinks:

$$\frac{\partial x_{CH_4}}{\partial t} + \vec{v} \cdot \vec{\nabla} x_{CH_4} = \frac{P_{CH_4} - L_{CH_4}}{n \cdot M} \tag{1.4}$$

where n and M are the number density and molar mass of air, respectively. The continuity equation thus relates the growth rate and advection of CH_4 to its chemical loss in and emissions to the atmosphere.

Comparing the timescales of distinct processes that govern the distribution of tracer mole fractions allows for the isolation of the relative contribution of emissions, chemical loss, isentropic mixing, and diabatic advection to the observed spatial distribution of CH_4 in the atmosphere. For CH_4, these scalings vary spatially and seasonally in response to the temporal and spatial variability of the various processes underlying each of these terms.

1.3.1 Chemical Loss

Although emissions has captured most of the focus in the CH_4 literature, the sink term has a longer history of deepening our knowledge of the global CH_4 budget.

Soon after its discovery, Bates and Witherspoon (1952) could deduce that CH_4 is not produced in the atmosphere by comparing the activation energies of potential chemical loss pathways. They determined that the spatial distribution is a function of atmospheric mixing, which must occur rapidly relative to the reaction rate of its sinks. As the first indicators that the concentration was increasing, analysis of CH_4 loss lifetimes prompted the hypothesis that emissions are predominantly located in the Northern Hemisphere (Mayer et al. 1982). Accordingly, efforts to quantify changing CH_4 must consider the role of sinks in determining the global CH_4 budget.

CH_4 has a budget lifetime of about 9 years (Ciais et al. 2013), perturbation lifetime of 12 years (Prather 2007), and a stratospheric lifetime of 120 ± 24 years (Prather et al. 2012). The primary loss mechanism of CH_4 is reaction with OH in the troposphere, with minor isotopic differentiation in the sink:

$$CH_4 + OH \xrightarrow{k_{OH}} CH_3 + H_2O \tag{1.5}$$

$$^{13}CH_4 + OH \xrightarrow{k_{13}} {}^{13}CH_3 + H_2O \tag{1.6}$$

$$CH_3D + OH \xrightarrow{k_D} \text{products} \tag{1.7}$$

(Levy 1971; Burkholder et al. 2015) where $k_{OH} = 2.45 \times 10^{-12} \exp(\frac{-1775}{T})$ $cm^3\ molec^{-1}\ s^{-1}$ (Burkholder et al. 2015; Vaghjiani and Ravishankara 1991), $k_{12}/k_{13} = 1.005 \pm 0.002$, and $k_D = 3.5 \times 10^{-12} \exp(\frac{-1950}{T})$ $cm^3\ molec^{-1}\ s^{-1}$ (Burkholder et al. 2015).

Tropospheric OH is extremely reactive, with a lifetime on the order of 1 s, and therefore acts as the primary oxidizing agent in the troposphere (Levy 1971; Kley 1997). OH is not thought to vary significantly from year to year (Montzka et al. 2011) or between the Northern and Southern Hemispheres (Patra et al. 2014). However, the seasonal variability of OH concentrations is a primary driver of the seasonal cycle of CH_4 (Khalil and Rasmussen 1983).

OH concentrations are generally derived using its reaction rate with methyl chloroform (CH_3CCl_3). CH_3CCl_3 is a manufactured compound used in industrial processes whose emissions are fairly certain due to its international regulation (Lovelock 1977). This advantage has presented a challenge recently, however, as atmospheric concentrations are decreasing exponentially to levels approaching measurement error (Montzka et al. 2011; Prather et al. 2012). Houweling et al. (1999) argue that OH concentrations, and thus the estimated CH_4 sink, are generally overestimated

in models, and recent work by Prather et al. (2012) indicate that this bias may still persist.

In the stratosphere, CH_4 reacts with $O(^1D)$ and chlorine (Cl):

$$^{13}CH_4 + O(^1D) \xrightarrow{k_{O(^1D)}} CH_3 + OH \tag{1.8}$$

$$CH_3O \; or \; CH_2OH + H \tag{1.9}$$

$$CH_2O + H_2 \tag{1.10}$$

$$O(^3P) + CH_4 \tag{1.11}$$

$$CH_4 + Cl \xrightarrow{k_{Cl}} CH_3 + HCl \tag{1.12}$$

where $k_{O(^1D)} = 1.75 \times 10^{-10}$ cm^3 molec^{-1} s^{-1} and $k_{Cl} = 7.1 \times 10^{-12} \exp(\frac{-1270}{T})$ cm^3 molec^{-1} s^{-1} (Burkholder et al. 2015). Although these stratospheric reactions only comprise a small proportion of the atmospheric sink of CH_4, they are responsible for a steep decline in CH_4 concentrations above the tropopause. The resulting heterogeneity of the vertical profiles in the troposphere and stratosphere has important consequences for isolating tropospheric variability in total column measurements.

1.3.2 Wetland Emissions

Terrestrial wetlands contribute a significant fraction of global CH_4 emissions, and are the largest natural source. The mechanism associated with CH_4 emissions from wetlands derives from the saturated, and thus anoxic, properties of wetland soils, which creates conditions that promote methanogenesis (Singh et al. 2000; Chang and Yang 2003). Wetland vegetation can increase CH_4 emissions not only by providing substrates for methanogenesis, but also by promoting CH_4 transport from soils to the atmosphere (Singh et al. 2000).

Reports of wetlands' contribution to atmospheric CH_4 vary from twenty to over forty percent of emissions (Fung et al. 1991a; Singh et al. 2000; Chang and Yang 2003; Takeuchi et al. 2003), depending on the region studied and the assumptions associated with up-scaling findings. For example, Takeuchi et al. (2003) find that anaerobic decomposition in the water-logged peat lands of northern high-latitude wetland ecosystems could produce significant CH_4 emissions. As with CH_4 concentrations themselves, temporal and zonal variability of CH_4 production in wetlands depends on a number of environmental parameters whose relative importance is poorly constrained (Whiting and Chanton 1993; Pison et al. 2013). Takeuchi et

al. (2003) find that although CH_4 estimates are strongly influenced by pH, temperature, and the depth of water table, the correlation between CH_4 emissions and these environmental factors is low. Thus, they argue, vegetation cover is the only soil-ecological indicator that can be used to predict emissions. By contrast, Chang and Yang (2003) determined that CH_4 fluxes are primarily influenced by soil properties. While total organic carbon and total nitrogen show high correlation with CH_4 emissions, soil redox potential, light intensity, soil temperature, air temperature and soil pH correlate very weakly with CH_4 emissions in their study. Crozier et al. (1995) and Chang and Yang (2003) both conclude that as long as pH remains within a range of 6 to 8 (with 7.7 as the optimal range in coastal wetlands), methanogenic archaea should prosper.

Other studies examine the relationship between productivity and CO_2 fluxes as an intermediate step to understanding CH_4 fluxes. By simultaneously measuring CO_2 and CH_4 exchange in wetlands, Whiting and Chanton (1993) found a positive correlation between net ecosystem production and CH_4 emissions and posit that the former is the main independent variable in explaining the latter. They argue that primary productivity and microbial activity in wetlands associated with higher CO_2 concentrations in the atmosphere will increase CH_4 emissions, thereby increasing the greenhouse effect.

Although many studies on seasonal trends in CH_4 emissions from wetlands have been conducted (e.g., Aselmann and Crutzen 1989; Wilson et al. 1989; Smith and Lewis 1992; Singh et al. 2000; Ringeval et al. 2010), the mechanisms associated with seasonal variations are not completely understood. Complicating matters further, the link between wetland emissions and atmospheric CH_4 does not seem to be linear. For example, Chang and Yang (2003) found that although atmospheric concentrations of CH_4 did not vary seasonally in their test sites, CH_4 flux rates fluctuated significantly by season. Thus, the contribution of wetlands to local CH_4 concentrations at any given time, not to mention regional and global distributions on seasonal to decadal time scales, presents one of the most significant uncertainties in the CH_4 budget.

1.4 Conflicting Narratives Explaining Recent Methane Trends

While knowledge about the land-atmosphere exchanges in the CH_4 cycle have increased, little has been achieved in the past few decades to significantly reduce the uncertainties associated with their magnitudes at regional or global scales. Numer-

ous studies have attempted to explain the most recent trends in CH_4 by attribution to several of these emission sectors; however no arguments have been conclusive enough to generate broad acceptance.

The body of literature quantifying the contribution of CH_4 fluxes to global and regional trends in the atmospheric burden is extensive (Dlugokencky et al. 2011; Kirschke et al. 2013; Nisbet et al. 2014; Saunois et al. 2016; Hartmann et al. 2013). We thus focus on a subset of those papers that analyze tropospheric CH_4 in the past decade. Approaches that assimilate observations into simple box or chemical transport models generally follow a pattern of specifying three elements in their explanations of the changing CH_4 growth rate: what emissions sector or sink is responsible for observed distribution, where these fluxes are located geographically, and by how much they must have changed to account for the stagnant or increased atmospheric burden.

The sudden reversal of the growth rate trend in 2006 and 2007 has inspired contrasting perspectives. Rigby et al. (2008) postulate that higher temperatures may have made wetlands in both hemispheres more productive, or a decrease in OH may have been coupled with an escalation of Northern Hemisphere CH_4 emissions. However, Dlugokencky et al. (2009) and Bousquet et al. (2011) both find little evidence that recent upward trends in CH_4 are due to declining OH concentrations or a higher incidence of biomass burning and instead argue that wetland emissions are the primary culprit. Bergamaschi et al. (2013) attribute between 50-75% and 30-50% of the rising CH_4 through 2010 to increased tropical and northern mid-latitude anthropogenic emissions, respectively.

This tradition of simultaneous opposing conclusions is not unique to the literature explaining the most recent CH_4 trends (c.f., Kai et al. 2011; Aydin et al. 2011); however, a greater number of observational capabilities since 2004 have widened the span of conclusions, with various combinations of emission type, amount and region of origin. Turner et al. (2015) assimilate Greenhouse gases Observing SATellite (GOSAT) satellite measurements into an adjoint-model inversion to optimize North American emissions and conclude that in 2009-2011 about 80% of CH_4 emissions in the United States were anthropogenic, one-third to almost one-half of which they attribute to livestock. Based on changes in isotopic composition in the atmosphere, Nisbet et al. (2016) suggest that the increase since 2007 was tropical and microbial, though they do not differentiate between wetlands and agriculture. Schaefer et al. (2016) also analyze CH_4 isotopes and arrive at the same conclusion

that biogenic emissions have been increasing, but speculate that the signal more likely corresponds to agriculture. In their evaluation of atmospheric C_2H_6 trends, Franco et al. (2016) use tracer-tracer analysis to calculate that oil and gas development in North America account for a 15 Tg yr^{-1} increase in CH_4 emissions in 2014 compared to 2008. Schwietzke et al. (2016), by contrast, argue that fossil-related CH_4 emissions have not been changing since 2000 but rather have been underestimated, and anthropogenic fuel emissions are in fact 20-60% greater than bottom-up estimates.

Synthesizing the literature, Kirschke et al. (2013) compare scenarios of various combinations of emissions estimates to observed trends. Their calculations indicate a discrepancy of more than 800% between the observed change in the atmospheric burden and the balance between sources and sinks from bottom-up inventories and process-based models (6 versus 50 Tg annually), and they ascribe the overestimation to natural sources, which drive the largest disagreement between bottom-up and top-down studies. The spectrum of results, which depends on underlying measurements, models, and assumptions, highlights the difficulty in synthesizing observations that provide information of disparate spatial and temporal scales. Measurements that traverse these scales will be critical in interpreting the connection between observed atmospheric trends and fluxes of CH_4.

1.5 Bridging Scales with the Total Carbon Column Observing Network

Meaningful evaluation of CH_4 trends requires precise and accurate measurements of atmospheric CH_4 that can bridge spatial and temporal scales of variability. Since 1948, both the precision and accuracy of trace gas column measurements have improved markedly, and the current generation of FTS instruments provide an invaluable complement to in situ observations. Total Carbon Column Observing Network (TCCON), a ground-based network of FTS instruments, has measured pressure-weighted total column-averaged dry-air mole fractions (DMFs) of CH_4, among other trace gases, since 2004. In the subsequent decade, the number of sites that have become operational has expanded (Table 1.2), with the aim of increasing the geographical coverage of the network (Figure 1.2). This dissertation describes the ways in which TCCON CH_4 can address the observational gaps that obstruct constraints on global CH_4 fluxes.

Figure 1.2: Map of TCCON sites.

Table 1.2: TCCON sites, coordinates, altitudes, start date of measurements, and locations for which tropospheric columns have been derived.

Site	Latitude (°)	Longitude (°)	Altitude (km)	Start date	Location	Data reference
Eureka	85.0	−86.4	0.61	Jul 2010	Eureka, Canada	Strong et al. (2014)
Sodankylä	67.4	26.6	0.18	May 2009	Sodankylä, Finland	Kivi et al. (2014)
Bialystok	53.2	23.0	0.18	Mar 2009	Bialystok, Poland	Deutscher et al. (2014)
Bremen	53.1	8.9	0.03	Jan 2007	Bremen, Germany	Notholt et al. (2014)
Karlsruhe	49.1	8.4	0.11	Apr 2010	Karlsruhe, Germany	Hase et al. (2014)
Orleans	48.0	2.1	0.13	Aug 2009	Orleans, France	Warneke et al. (2014)
Garmisch	47.5	11.1	0.75	Jul 2007	Garmisch, Germany	Sussmann and Rettinger (2014)
Park Falls	45.9	−90.3	0.47	Jun 2004	Park Falls, WI, USA	Wennberg et al. (2014d)
Rikubetsu	43.5	143.8	0.36	Nov 2013	Rikubetsu, Japan	Morino et al. (2014b)
Lamont	36.6	−97.5	0.32	Jul 2008	Lamont, OK, USA	Wennberg et al. (2014c)
Tsukuba	36.0	140.1	0.03	Aug 2011	Tsukuba, Japan	Morino et al. (2014a)
Dryden	35.0	−117.9	0.70	Jul 2013	Dryden, CA, USA	Iraci et al. (2014)
JPL	34.2	−118.2	0.39	Jul 2007	Pasadena, CA, USA	Wennberg et al. (2014a) and Wennberg et al. (2014b)
Caltech	34.1	−118.1	0.23	Sep 2012	Pasadena, CA, USA	Wennberg et al. (2014e)
Saga	33.2	130.3	0.01	Jul 2011	Saga, Japan	Kawakami et al. (2014)
Izaña	28.3	−16.5	2.37	May 2007	Tenerife, Canary Islands	Blumenstock et al. (2014)
Darwin	−12.4	130.9	0.03	Aug 2005	Darwin, Australia	Griffith et al. (2014a)
Réunion Island	−20.9	55.5	0.09	Sep 2011	Saint-Denis, Réunion	De Maziere et al. (2014)
Wollongong	−34.4	150.9	0.03	Jun 2008	Wollongong, Australia	Griffith et al. (2014b)
Lauder	−45.0	169.7	0.37	Jun 2004	Lauder, New Zealand	Sherlock et al. (2014a, 2014b)

1.6 Dissertation Organization

This research presents additional observational constraints on CH_4 distributions to isolate the drivers of seasonal, interannual, and long-term variability by developing and synthesizing measurements, integrating observations into data analysis, and assessing models to further the goals of quantifying CH_4 fluxes. The first chapter describes advancements in remote sensing observations of tropospheric CH_4 for the analysis of spatial and temporal trends. The second chapter addresses how artifacts in models and CH_4 measurements impact the current scientific understanding of distributions of CH_4 and its sources. The third chapter evaluates the component of CH_4 variability that can be attributed to transport and identify dynamical processes that co-vary and possibly determine zonal patterns of CH_4. The concluding chapter presents an outlook for the application of tropospheric CH_4 columns in conjunction with those of other trace gases to characterize how CH_4 emissions from fossil sources are changing, especially in urban environments.

Table 1.3: Tropospheric CH_4 versions used in this dissertation.

Version	Chapter	Reference
xch4tr.tccon.ggg2012.R0	2	Saad et al. (2014)
xch4tr.tccon.ggg2014.R0	3	Saad et al. (2016)
xch4tr.tccon.ggg2014.R1	4	

Chapter 2

DEVELOPMENT OF TROPOSPHERIC METHANE PARTIAL COLUMN OBSERVATIONS FROM CH_4 AND HF TOTAL COLUMN MEASUREMENTS

2.1 Motivation for Tropospheric Methane Column Measurements

Analyses of temporal and geospatial trends of CH_4 require precise, continuous measurements with adequate spatial coverage. Several such monitoring networks, such as World Meteorological Organization (WMO) Global Atmospheric Watch and National Oceanic and Atmospheric Administration (NOAA) Global Monitoring Division, have measured methane (CH_4) for decades. These sites are often in locations primarily intended for background observations, and measurements are confined to the surface, primarily within the boundary layer. The Total Carbon Column Observing Network (TCCON), a ground-based network of near-infrared (NIR) Fourier transform spectrometers (FTSs), measures dry-air mole fractions (DMFs) of several atmospheric trace gases, including CH_4, integrated over the entire atmospheric column. The column measurements are sensitive to the free troposphere in addition to the surface, which can allow for better separation of transport from local emissions. Additionally, total column measurements are less sensitive to vertical transport and mixing, and thus meridional or zonal gradients in column measurements can be used to characterize regional-scale fluxes (Yang et al. 2007; Wunch et al. 2011a; Keppel-Aleks et al. 2011). Several TCCON stations are near in situ sites that provide surface, tall tower, and aircraft measurements, which we use to compare the final tropospheric column-averaged CH_4 DMFs.

Tropospheric trends of CH_4 are obscured in total column measurements by variability originating in the stratosphere, especially by vertical shifts of the tropopause. Several methods for accounting for stratospheric variability have been proposed, including incorporating the compact relationship between CH_4 and another chemical tracer in the stratosphere (e.g., Washenfelder et al. 2003; Payne et al. 2009; Angelbratt et al. 2011; Sepúlveda et al. 2012; Sepúlveda et al. 2014; Wang et al. 2014). Washenfelder et al. (2003) estimate the contribution of variations in stratospheric CH_4 as the product of the hydrogen fluoride (HF) column-averaged DMF and the CH_4–HF relationship, calculated from the Halogen Occultation Exper-

iment (HALOE) satellite and the JPL MkIV Interferometer data. Wang et al. (2014) similarly use the relationship between stratospheric nitrous oxide (N_2O) and CH_4 and the fact that tropospheric N_2O is well known to infer stratospheric variations in N_2O, and hence CH_4. Angelbratt et al. (2011) remove the Network for the Detection of Atmospheric Composition Change (NDACC) CH_4 total column variability with a multiple regression model that parameterizes anomalies of several measurements, including HF, carbon monoxide, ethane, and tropopause height. Sepúlveda et al. (2012) use the retrieval algorithm PROFFIT to infer vertical CH_4 profiles directly from the absorption line shapes of the mid-infrared (MIR) FTS spectra measured within NDACC, comparing the resulting tropospheric columns with those calculated with a HF proxy method. Extending this study to additional sites, Sepúlveda et al. (2014) estimate a precision of 0.5% and a systematic error of 2.5% for daily mean values of tropospheric CH_4 derived from profile retrievals on the MIR NDACC measurements.

Vertical profile retrievals using the TCCON spectra are more difficult than those using NDACC MIR spectra because the NDACC measurements apply spectral filters to narrow the spectral coverage, yielding higher signal-to-noise ratios at higher spectral resolution, at the expense of making simultaneous measurements of some other gases. In addition, the line strengths in the MIR are generally higher and doppler widths are smaller, allowing more degrees of freedom in the vertical retrieval. Nevertheless, profile retrievals are more sensitive to error in the instrument and assumed spectroscopic line shapes than profile-scaling retrievals. Quantifying the variability of stratospheric CH_4 via a chemical tracer is, however, not without challenge, as this method is sensitive to errors in the representation of the relationship between that tracer and CH_4 in the stratosphere and knowledge of their respective averaging kernels. In addition, this method provides no information about vertical structure within the troposphere.

To determine the stratospheric CH_4 component of the FTS-retrieved total column, we propose to use its relationship with HF, which is measured at almost all TCCON sites. Stratospheric CH_4 has a nearly linear inverse relationship with HF, which exists almost exclusively in the stratosphere (Luo et al. 1995; Washenfelder et al. 2003). The photodissociation of chlorofluorocarbons (CFCs) and the resulting carbonyl products produce free fluorine, which can then in turn react with CH_4 and water vapor (H_2O) to produce HF, the most stable reservoir species of fluorine in the stratosphere (Luo et al. 1994). The reactions producing HF occur in the middle-

high stratosphere, leading to a uniformly increasing vertical profile (Luo et al. 1995). CH_4, by contrast, is transported from the troposphere and is destroyed by O(1D), hydroxyl, and chlorine free radical-initiated oxidation. The resulting nearly linear relationship between HF and stratospheric CH_4, which is seasonally and zonally consistent, makes HF a useful proxy for the contribution of stratospheric variability to the CH_4 total column.

2.2 Derivation of Tropospheric Methane Columns

TCCON FTS retrievals are conducted with the GFIT nonlinear least-squares fitting algorithm, which determines a scale factor (γ) of an a priori vertical profile ($\vec{x}^{\,a}$) based on the best spectral fit of the solar absorption signal. The scaled profile is then vertically integrated, and the resulting column abundance is divided by the vertical column of dry air, calculated using the retrieved column of oxygen (O_2) (Wunch et al. 2010; Wunch et al. 2011a). The retrieved integrated column of CH_4 can be expressed as a first order Taylor expansion about the solution $\gamma_{CH_4} c^a_{CH_4}$ (Rodgers and Connor 2003) such that,

$$\hat{c}_{CH_4} = \gamma_{CH_4} \cdot c^a_{CH_4} + \vec{a}^{\,\S}_{CH_4}(\vec{x}_{CH_4} - \gamma_{CH_4}\vec{x}^{\,a}_{CH_4}) \tag{2.1}$$

where $\hat{c}$ is the retrieved column, γ_{CH_4} is the retrieved profile scale factor of CH_4, $\vec{x}$ is the true profile, and $\vec{x}^{\,a}_{CH_4}$ and $c^a_{CH_4}$ are the a priori vertical profile and column-integrated CH_4, respectively. We define § as an operator that represents the pressure-weighted integration of the profile:

$$\vec{a}^{\,\S}\vec{x} = \sum_{i=1}^{N} a_i \cdot h_i \cdot x_i \tag{2.2}$$

where $\vec{a}$ is the FTS column averaging kernel, dependent on solar zenith angle and pressure, $\vec{h}$ is the pressure-weighting function, such that $\hat{c} = \vec{h}^T\vec{\hat{x}}$ (Connor et al. 2008; Wunch et al. 2011b), and i is the index of pressure levels from the surface to the highest level, N. When the vertical column includes water vapor, such as in the case of the priors, the pressure-weighting function incorporates the H_2O profile to convert $\vec{x}$ to dry-air mole fractions.

To isolate the tropospheric column of CH_4, we assume a linear relationship between

CH_4 and HF in the stratosphere such that

$$\vec{x}_{CH_4} = c^{trop}_{CH_4}\vec{u} + \beta\vec{x}_{HF} \tag{2.3}$$

where $c^{trop}_{CH_4}$ represents the pressure-weighted DMF averaged over the tropospheric column, $\vec{u}$ is a unity vector the length of the number of vertical levels in the total column retrieval integration, and β is the time-dependent CH_4–HF slope in the stratosphere. Integrating the vertical profiles, the column-averaged form of this relationship becomes

$$c_{CH_4} = c^{trop}_{CH_4} + \beta c_{HF} \tag{2.4}$$

where c is the total column DMF of the respective trace gases. The βc_{HF} term is negative and represents the amount of CH_4 that has been destroyed in the stratosphere, rather than the stratospheric partial column of CH_4. We also assume that the a priori CH_4 profiles can be approximated using the linear relationship between CH_4 and HF.

By combining Equations (2.3) and (2.4), as well as their analogs for the a priori profiles, into Equation (2.1), we derive a tropospheric column-average DMF:

$$c^{trop}_{CH_4} = \hat{c}_{CH_4} - \beta\left(\gamma_{CH_4}\cdot c^{a}_{HF} + \vec{a}^{\S}_{CH_4}(\vec{x}_{HF} - \gamma_{CH_4}\vec{x}^{a}_{HF})\right). \tag{2.5}$$

Ideally, $\vec{x_{HF}}$ would be derived from the equivalent of Equation (2.1) for HF, but doing so would require inverting the pressure-weighted averaging kernel, which does not have a unique solution. Thus, in order to solve Equation (2.5), we must assume that $\vec{x}_{HF} = \vec{\hat{x}}_{HF} = \gamma_{HF}\vec{x}^{a}_{HF}$ and, accordingly, that the shape of the HF profile is known. In general, this is a reasonable assumption because the vertical profile is governed mainly by well-characterized chemical production, and, as previously stated, increases uniformly. However, this solution has limitations when the scaled profile deviates from the true profile, such as in the polar vortex.

Substituting $\gamma_{HF}\vec{x}^{a}_{HF}$ for $\vec{x}_{HF}$, the tropospheric column of CH_4 is derived as follows:

$$c^{trop}_{CH_4} = \hat{c}_{CH_4} - \beta\left(\gamma_{CH_4}\cdot c^{a}_{HF} + \vec{a}^{\S}_{CH_4}\vec{x}^{a}_{HF}(\gamma_{HF} - \gamma_{CH_4})\right). \tag{2.6}$$

All of the terms on the right hand of the equation can be generated from the TCCON data set except for β, which we derive from satellite data. Equation (2.6) can be

applied to determine tropospheric DMFs of trace gases other than CH_4 that are correlated with HF in the stratosphere because it does not require assumptions about the relationship between the averaging kernels of the respective gases and is thus a more general approach than that of Washenfelder et al. (2003).

2.2.1 Measurement uncertainties

The $c^{\text{trop}}_{CH_4}$ error is calculated by propagating the uncertainties of the retrievals, which in Equation (2.6) are associated with the scale factors, and β, which is described in Sect. 2.2.2. These errors are propagated as the sum of the squares of the standard errors for each term. Because the scale factor errors are derived assuming that the residuals from the spectral fits have a Gaussian distribution, systematic artifacts that are stable from spectrum to spectrum inflate the errors calculated from the spectral fit. To derive the measurement precision, the uncertainties are scaled to account for the variations in DMFs calculated from successive spectra within 5 min. The mean and median tropospheric CH_4 precisions vary from 0.04–1 and 0.01–0.03%, respectively, at individual sites and are 0.1 and 0.004% across all sites and years. By comparison, the precision in Washenfelder et al. (2003) is 0.5%, although this improvement is partially attributable to advancements in the retrieval methodology and instrumentation. The data have been corrected for laser sampling errors (Dohe et al. 2013; Messerschmidt et al. 2010), and the associated uncertainties of those corrections are summed in quadrature with the measurement precision.

2.2.2 Determination of CH_4–HF slope

Vertical profiles of CH_4 and HF mole fractions were developed from level 2, version 3.0 and 3.5 retrievals from the Atmospheric Chemistry Experiment Fourier Transform Spectrometer (ACE-FTS) instrument on the Canadian SCISAT-1 satellite. SCISAT-1 orbits in low Earth orbit with an inclination of 74°, offering coverage of tropical, mid-latitude and polar regions from 85°N to 85°S (Bernath 2005; De Mazière et al. 2008; Mahieu et al. 2008; Waymark et al. 2014). Data were taken from February 2004 through September 2010 for version 3.0 and October 2010 through December 2012 for version 3.5. These data sets differ only in that the a priori pressure and temperature profiles in the latter are taken from the global Canadian Meteorological Center model rather than the regional one, which began to provide unphysical profiles starting October 2010 (Waymark et al. 2014). The ACE-FTS profiles are additionally filtered to exclude occultations with physically unlikely profiles and all individual CH_4 and HF retrievals with statistical fitting

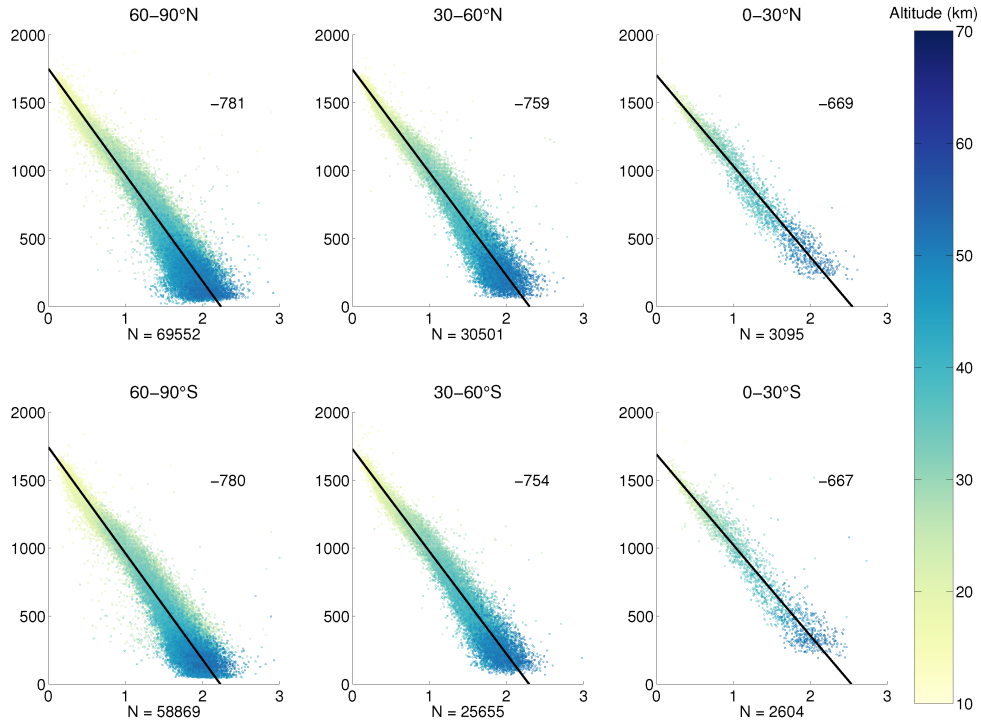

Figure 2.1: CH_4 (ppb, y axis) vs. HF (ppb, x axis) from ACE-FTS measurements taken between 2004–2012, binned by zonal bands. The slopes of the linear regression are in the upper right-hand corner, and number of data points (N) are listed below each plot.

errors above 5%. Because the HF abundance in the troposphere is essentially zero, any coincident retrievals of CH_4 and HF were assumed to reside in the stratosphere; therefore we did not designate a pressure level threshold to isolate the stratosphere. Data above 70 km were excluded for consistency with TCCON retrievals, although CH_4 concentrations are generally depleted at that altitude. The CH_4–HF relationship exhibits a strong altitude dependence, with steeper CH_4–HF slopes in the upper stratosphere (Figure 2.1). Annual slopes follow the long-term trend from Washenfelder et al. (2003), given the expected trajectory of HF concentrations in the stratosphere (Figure 2.2).

Tracer–tracer relationships in the stratosphere tend to be dependent on latitude, with the tropics exhibiting different slopes than the mid-latitude "surf zone" and the polar regions (Luo et al. 1995). While ACE-FTS coverage at high latitudes is extensive, tropical coverage is sparse; thus, to ensure a large enough number of data points in the tropics for robust statistical analysis, we binned CH_4 and HF mole fractions in 30° zonal bands. The tracer relationship demonstrates a clear zonal trend: the slopes are less steep in lower latitudes, and the Northern Hemisphere slopes are

more steep than their zonal counterparts in the Southern Hemisphere (Figures 2.1 and 2.2). To determine statistically robust values for β, the CH_4–HF slope was computed for bootstrap subsamples of 1000 individual retrievals from each year and zonal band. In order to minimize the effect of outliers in the determination of the slope, we applied an iteratively re-weighted least squares regression with a Tukey's bi-weight function, weighting data points by pressure (Hoaglin et al. 1983). The means and 2σ standard deviations of the resulting probability distributions were taken respectively as the values and errors of β (Table 2.1). For 2013, we calculated the annual growth rate of the CH_4–HF ratio in the northern mid-latitude region (30–60°N), chosen because the surf zone is well-mixed and thus has the most robust tracer relationships, and added it to the respective zonal values for 2012. The error for β in 2013 was computed as the sum in quadrature of the error for β in 2012, the standard error of the annual growth rate, and the 2σ standard deviations of the interannual variability of each zonal band. While temporal trends in β do indicate seasonal variability, the impact on the slopes is not sufficiently statistically robust from year to year to incorporate a seasonally varying β. The sensitivity of the tropospheric CH_4 calculation to β differs by site, but generally varies by 0.1–1 ppb for $\Delta\beta$ of 10.

2.2.3 Validation of methodology

Equation (2.6) incorporates two major assumptions: that the CH_4–HF relationship is linear, and that the retrieved HF column is a close approximation to the true HF column. To test these assumptions, we compared tropospheric CH_4 DMFs

Table 2.1: Annual zonal values (2σ uncertainties) of β. Values after 2012 are extrapolated from the long-term trend.

	60–90°S	30–60°S	0–30°S	0–30°N	30–60°N	60–90°N
2004	-719 (7)	-706 (10)	-674 (28)	-714 (17)	-739 (7)	-756 (5)
2005	-739 (5)	-729 (7)	-701 (18)	-633 (22)	-740 (6)	-748 (4)
2006	-742 (6)	-725 (9)	-648 (25)	-690 (18)	-752 (7)	-758 (5)
2007	-738 (6)	-730 (9)	-684 (31)	-620 (50)	-742 (8)	-754 (5)
2008	-743 (6)	-732 (8)	-665 (25)	-705 (23)	-734 (6)	-749 (4)
2009	-727 (6)	-721 (10)	-635 (36)	-661 (28)	-743 (9)	-755 (6)
2010	-706 (5)	-709 (7)	-658 (22)	-656 (27)	-716 (7)	-737 (4)
2011	-746 (5)	-735 (9)	-596 (61)	-607 (25)	-704 (6)	-731 (4)
2012	-714 (7)	-705 (8)	-624 (51)	-641 (24)	-722 (7)	-724 (5)
2013	-712 (23)	-703 (20)	-622 (63)	-639 (63)	-720 (16)	-722 (11)

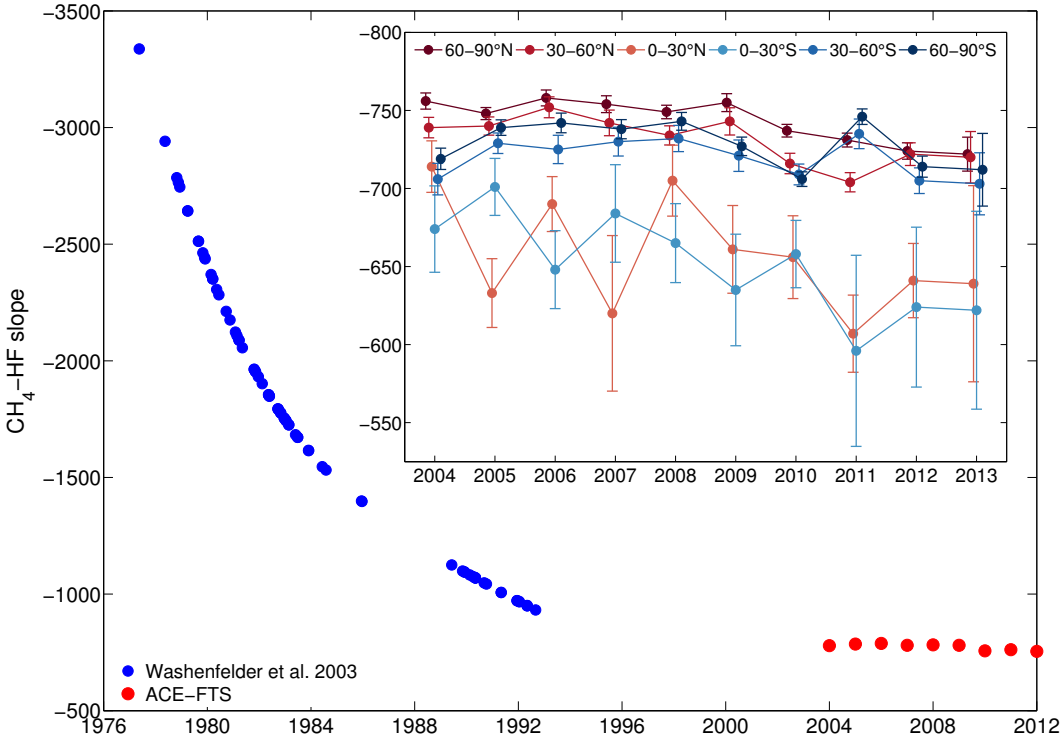

Figure 2.2: Long-term CH_4–HF slopes derived by Washenfelder et al. (2003) and annual-mean slopes from ACE-FTS measurements. The inset shows the time series of zonal pressure-weighted ACE-FTS slopes (β), with error bars denoting the 2σ standard error. For each year, zonal slopes are offset from each other for clarity.

derived directly from ACE-FTS CH_4 profiles to those calculated by substituting the most recent TCCON priors (GGG 2014) and ACE-FTS CH_4 and HF profiles into Equation (2.5). For this analysis, the ACE-FTS trace gas profiles up to 70 km interpolated onto a 1 km vertical grid were considered the true profiles $\vec{x}_{HF}$ and $\vec{x}_{CH_4}$, and assuming $\gamma_{CH_4} \approx 1$, we solved Equations (2.1) and (2.5) for $c^{trop}_{CH_4}$. Because the minimum retrieval altitudes were at least 5.5 km and on average 9.5 km, mole fractions of CH_4 and H_2O near the surface were extrapolated using TCCON priors. Occultations with individual CH_4, HF and H_2O errors greater than 10% were excluded for latitudes poleward of ±30°. In the tropics, the error threshold was relaxed to 40% in order to ensure a large enough data set for results to be meaningful. We then compared the calculated tropospheric CH_4 column-averaged DMF to the ACE-FTS CH_4 profiles integrated to the tropopause. For the intercomparison, the integrated ACE-FTS profiles were smoothed with the TCCON CH_4 averaging kernel and priors (Connor et al. 2008; Wunch et al. 2011b). The tropopause altitude was calculated using National Centers for Environmental Prediction/National Center for

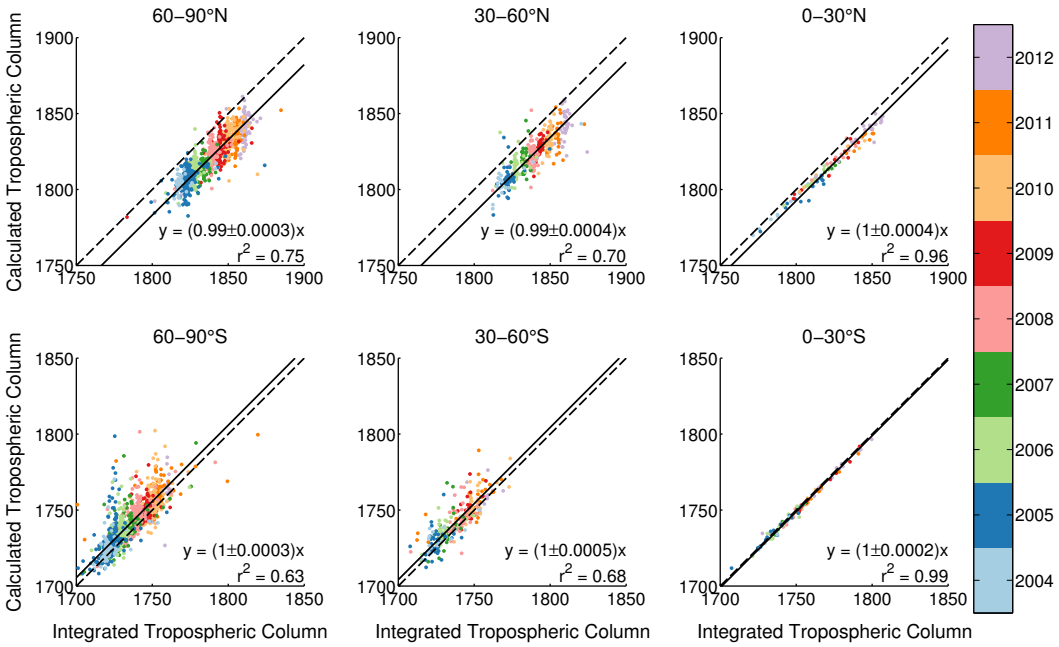

Figure 2.3: Validation of the tropospheric column-averaged CH_4 derivation using HF as a proxy. The calculated tropospheric CH_4 (y axis) uses the TCCON priors, CH_4 averaging kernel, and ACE-FTS vertical profiles to determine the value that the ground-based FTS would retrieve. The integrated tropospheric CH_4 (x axis) applies the pressure-weighting function and TCCON CH_4 averaging kernel and priors to the extrapolated tropospheric ACE-FTS profile of CH_4. The black lines depict the one-to-one line (solid) and the linear regression of the calculated versus integrated tropospheric CH_4 with a zeroed y intercept (dashed). The r^2 values correspond to the linear regression. Note the different DMF ranges in the Northern versus Southern Hemispheres.

Atmospheric Research (NCEP/NCAR) Reanalysis local noon temperature profiles (Kalnay et al. 1996), from which the TCCON priors are generated, for consistency.

As Figure 2.3 illustrates, the temporal and zonal dependencies of the tropospheric CH_4 calculation are well characterized, with a few notable exceptions. The consistency of the bias across years (slope = 0.99–1) indicates that the annual variability of β is accurate, although the asymmetric scatter of the residuals in the northern tropics could be a result of the smaller number of data points included in the determination of β. Additionally, the seasonal variability associated with descent within the polar vortices, not currently captured by the HF priors, accounts for the outliers apparent in higher latitudes. Because the southern polar vortex is stronger and more persistent than in the north, the calculated tropospheric column exhibits a much larger spread in the southern polar zonal band.

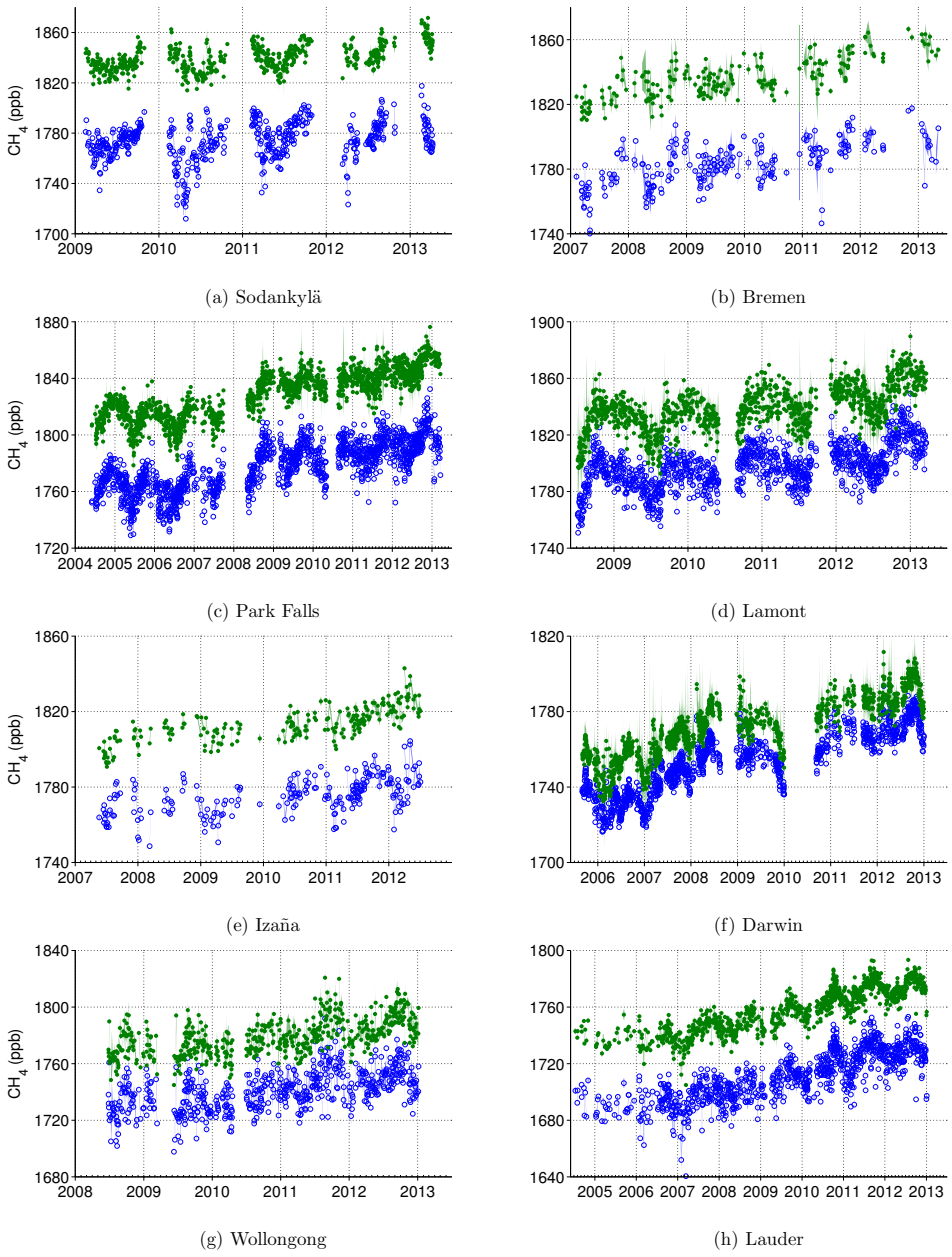

Figure 2.4: Daily median and standard deviation (shading) $X_{\mathrm{CH_4}}$ (blue, open circles) and $X^t_{\mathrm{CH_4}}$ (green, closed circles) at **(a)** Sodankylä, Finland, **(b)** Bremen, Germany, **(c)** Park Falls, Wisconsin, USA, **(d)** Lamont, Oklahoma, USA, **(e)** Izaña, Tenerife, Canary Islands, **(f)** Darwin, Australia, **(g)** Wollongong, Australia, and **(h)** Lauder, New Zealand. Only days with more than 10 $X^t_{\mathrm{CH_4}}$ measurements with errors of $< 1\%$ are shown. Both the 120 HR (June 2004–December 2010) and 125 HR (February 2010–December 2012) instruments are plotted for Lauder.

The underestimation of tropospheric CH_4 in the Northern Hemisphere and slight overestimation in the Southern Hemisphere is partially a result of several assumptions that are necessary because coincident TCCON measurements do not exist for all zonal regions over the time series. TCCON averaging kernels are highly dependent on the solar zenith angle at the time of measurement; however, the solar zenith angles at the surface during ACE-FTS occultations are close to 90°. We use the solar zenith angle calculated at the latitude, longitude and time of the occultation, which, while accurate, does not test one of the main advantages of this methodology, which is to adjust the tropospheric CH_4 calculation for seasonality and latitude, which impacts each zonal band differently and thus creates an offset. The averaging kernels also depend on surface pressure, which for the ACE-FTS occultation is unknown. To address this, we assume that the pressure at the lowest point in the ACE-FTS pressure/temperature profile is the surface pressure. Because these values are not retrieved, but rather a priori, any spatial biases in these values can impact the zonal or interhemispheric differences in this comparison.

The method validation also requires the assumption that $\gamma_{CH_4} = 1$ in Equations (2.1) and (2.5). A bias in the a priori profiles between the Northern and Southern Hemispheres would lead to differences in the retrieved values of γ_{CH_4}, indicating that the TCCON a priori profiles are slightly too low in the Southern Hemisphere relative to the Northern Hemisphere. While γ_{CH_4} is generally within 1% of 1, TCCON measurements tend to have larger values for γ_{CH_4} in the Southern Hemisphere compared to the Northern Hemisphere, and a difference of 0.01 between hemispheres can shift the residuals from the one-to-one line by up to 4 ppb, or about one quarter of the offset in the mid-latitudes. Because of the low sensitivity of the tropospheric CH_4 calculation to changes in β, inter-hemispheric biases in β determined from ACE-FTS would have to be considerable to explain the offset.

2.3 Results for GGG2012 $X^t_{CH_4}$

Tropospheric column-averaged DMFs ($X^t_{CH_4}$) were calculated for TCCON sites in Sodankylä (Figure 2.4a), Bremen (Figure 2.4b), Park Falls (Figure 2.4c), Lamont (Figure 2.4d), Izaña (Figure 2.4e), Darwin (Figure 2.4f), Wollongong (Figure 2.4g), and Lauder (Figure 2.4h) using the 2012 version of the GGG software. Location information for each of these TCCON sites can be found in Table 2.2. As we would expect, the values for $X^t_{CH_4}$ are higher than those of X_{CH_4}. Many of the low outliers in the total column that are a result of the stratospheric variability no longer appear in $X^t_{CH_4}$. The intraday variability of $X^t_{CH_4}$ are generally equivalent to those of the

corresponding X_{CH_4} values, although the tropospheric standard deviations are, in some cases, significantly larger than those of the total column. Sites in the tropics are especially susceptible to both larger errors for a single measurement and larger daily variances due to the higher HF errors caused by H_2O interference (for example, Darwin, Figure 2.4f). Additionally, the tropospheric calculation removes most of the effects of the seasonal cycle of stratospheric variability. While the magnitude of the impact on the seasonal cycle of CH_4 varies from site to site, the tropospheric column calculation generally shifts the peak of CH_4 from late fall to winter and the minimum from spring to late summer (Figure 2.5). At Lamont and Park Falls, this impact is especially apparent, with 2-month lags in the maxima and minima in the tropospheric versus total columns. The de-trended seasonal cycles of $X^t_{CH_4}$ also exhibit fewer short-term fluctuations, except in the case of Izaña, which is located on a mountain at about 2.4 km and thus is more sensitive to variability in the free troposphere.

2.3.1 Comparison to the Washenfelder et al. (2003) method

The derivation introduced here improves on the previous calculation of Washenfelder et al. (2003) by explicitly including the CH_4 averaging kernels in the estimate of stratospheric loss and including the recent ACE-FTS satellite data set, which allows for the analysis of temporal and zonal dependencies. To assess the impacts of these additions to the tropospheric CH_4 column, we calculated $X^t_{CH_4}$ using the Washenfelder et al. (2003) derivation (Equation 2.4) and the annual northern mid-latitude values of β (Table 2.1, column 6) for all sites. The daily standard deviations tend to decrease modestly with the updated methodology (Figure 2.6), although intraday variability is reduced by up to 40 ppb. The inclusion of the CH_4 averaging

Table 2.2: TCCON sites, coordinates, altitudes, and locations used in this analysis.

Site	Latitude	Longitude	Altitude (km)	Location
Sodankylä	67.4	26.6	0.18	Sodankylä, Finland
Bremen	53.1	8.85	0.03	Bremen, Germany
Park Falls	45.9	−90.3	0.44	Park Falls, WI, USA
Lamont	36.6	−97.5	0.32	Lamont, OK, USA
Izaña	28.3	−16.5	2.37	Tenerife, Canary Islands
Darwin	−12.4	130.9	0.03	Darwin, Australia
Wollongong	−34.4	150.9	0.03	Wollongong, Australia
Lauder	−45.0	169.7	0.37	Lauder, New Zealand

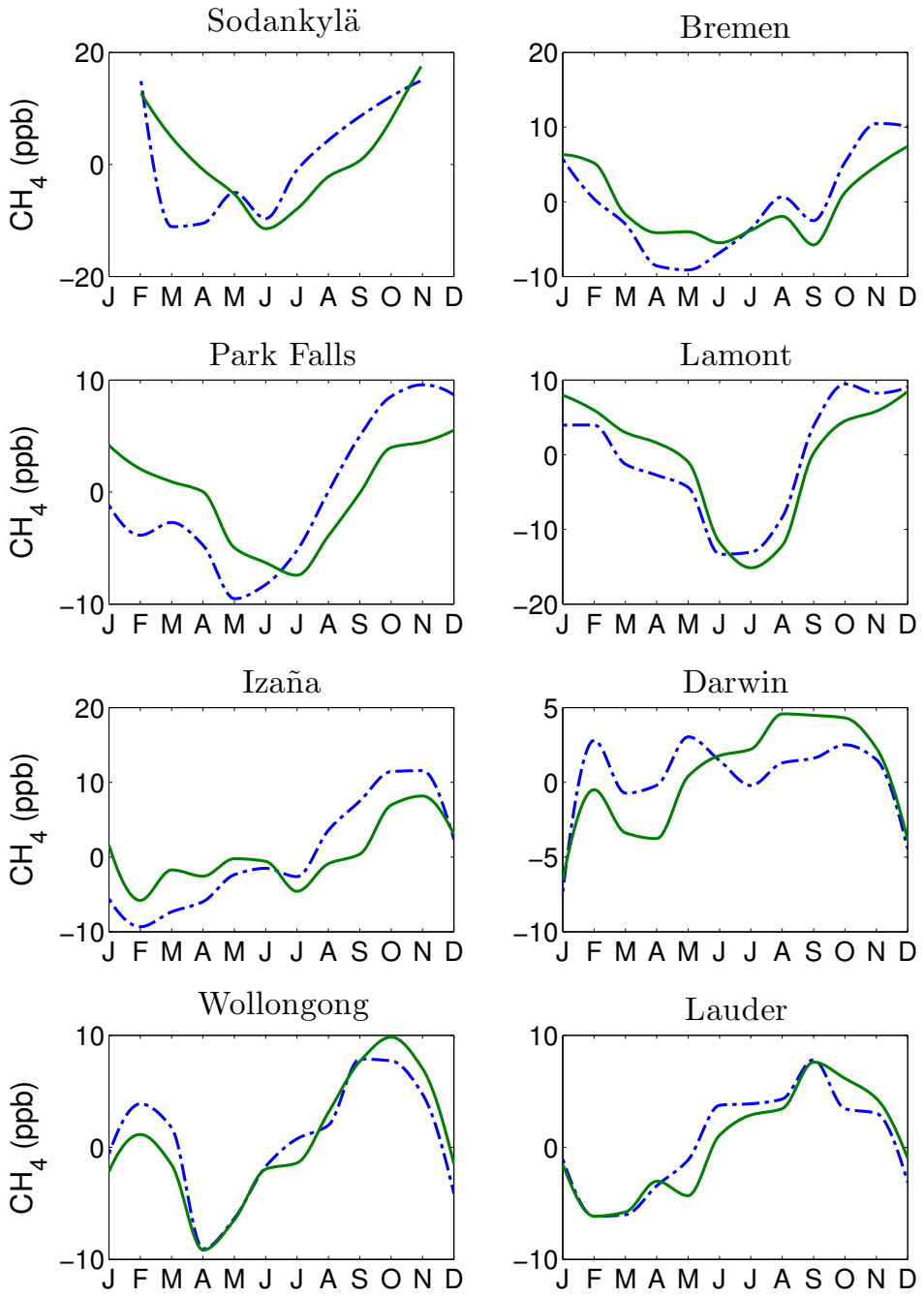

Figure 2.5: De-trended seasonal cycles of CH_4 for X_{CH_4} (blue, dashed) and $X^t_{CH_4}$ (green, solid), averaged over all years.

kernel adjusts the air-mass dependence of the tropospheric CH_4 calculation, thereby reducing the amplitude of the CH_4 seasonal cycle. This improvement is especially apparent during winter at the high-latitude sites (Figure 2.7), because the solar zenith angles are large and, therefore, the CH_4 averaging kernels have a strong dependence on altitude. Additionally, calculating the CH_4–HF relationship as a function of

latitude allows for more meaningful geospatial comparisons.

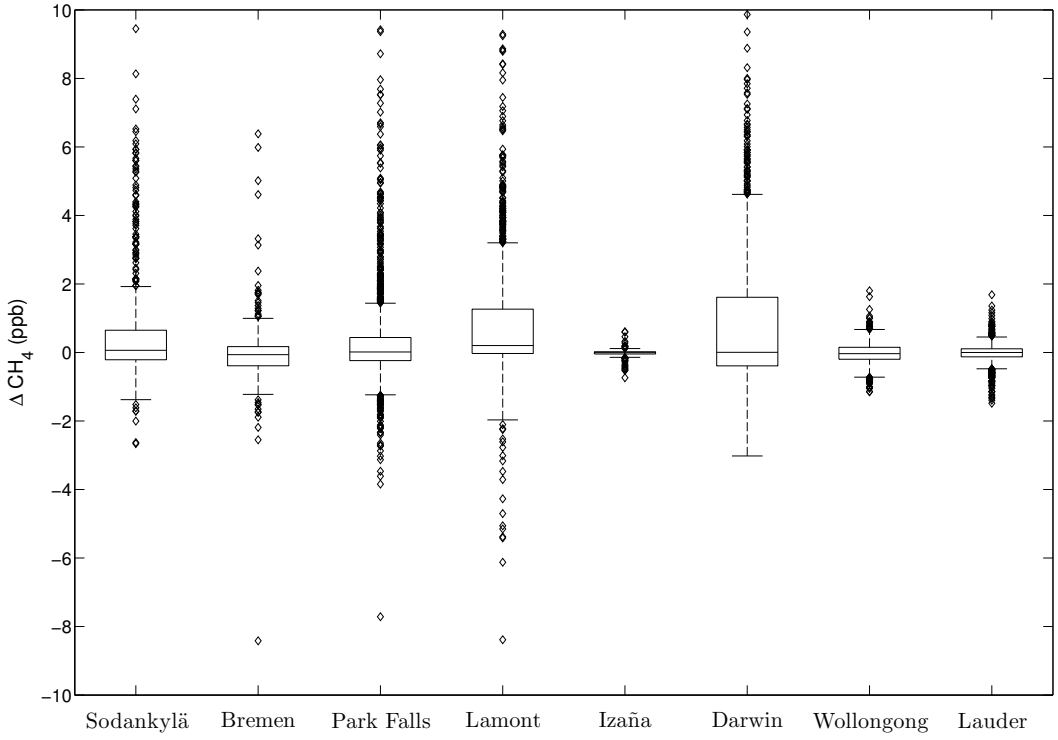

Figure 2.6: The differences between daily tropospheric CH_4 standard deviations using the Washenfelder et al. (2003) and updated methods. (Positive values correspond to larger Washenfelder et al. (2003) standard deviations.) Box ends, midline and whiskers illustrate the quartiles, medians and twice the interquartile ranges, respectively. Outliers beyond the the range are denoted by diamonds.

2.3.2 Comparison to in situ measurements

Following the method for numerical integration of in situ profiles derived in Wunch et al. (2010), smoothed column-averaged DMFs were determined for several air-

Table 2.3: Aircraft Overflights. TCCON site locations, aircraft campaign dates, and altitude ranges are listed.

Site	Location	Campaign	Date	Altitude (km)
Bremen	53°N, 9°E	IMECC	9 Oct 2009	0.5 – 13.2
Park Falls	46°N, 90°W	INTEX	12 Jul 2004	0.7 – 10.1
		START08	12 May 2008	1.2 – 9.4
Lamont	37°N, 98°W	HIPPO	30 Jan 2009	0.4 – 13.0
		Learjet	31 Jul; 2, 3 Aug 2009	0.5 – 12.9
Wollongong	34°S, 151°E	HIPPO	15 Nov 2009	0.1 – 12.6
Lauder	45°S, 170°E	HIPPO	20 Jan 2009	0.7 – 14.6

Figure 2.7: Daily median $X^t_{CH_4}$ at Sodankylä using the Washenfelder et al. (2003) method (black) versus the updated method (green). Shading is as in Figure 2.4.

craft campaigns (Table 2.3). Additional information on the TCCON calibration, including instruments, can be found in Wunch et al. (2010), and the WMO calibration scales used for the instruments can be found in Dlugokencky (2005). Aircraft profiles were integrated to the tropopause, determined using the flight temperature profiles. Aircraft errors are calculated as the sum in quadrature of the respective 2σ instrument errors and the estimated uncertainties associated with the profile not reaching the tropopause and the surface. FTS columns were calculated with the aircraft calibration factors for CH_4 determined in Wunch et al. (2010) applied to the tropospheric column and thus do not include the spectroscopy bias that exists in the total column. FTS errors are calculated as the standard deviation of tropospheric DMFs with individual errors of less than 1% measured within 1 hour of each flight. Both the slope and associated error are calculated considering both the aircraft and FTS errors, assuming those errors are independent of each other, following the method outlined in York et al. (2004). Additionally, because the derivation method is predicted to vary linearly, we calculate the slope assuming a y intercept of zero.

The FTS tropospheric columns show general agreement to each other (Figure 2.8), with a slope close to within error of the one-to-one line and a slope and error similar to that of total column CH_4 (Wunch et al. 2010). The tropospheric column calibration curve has a slight hemispheric bias, with Southern Hemisphere sites above the fit line and Northern Hemisphere sites below, with the INTEX-NA campaign, over Park Falls, WI, as the only exception.

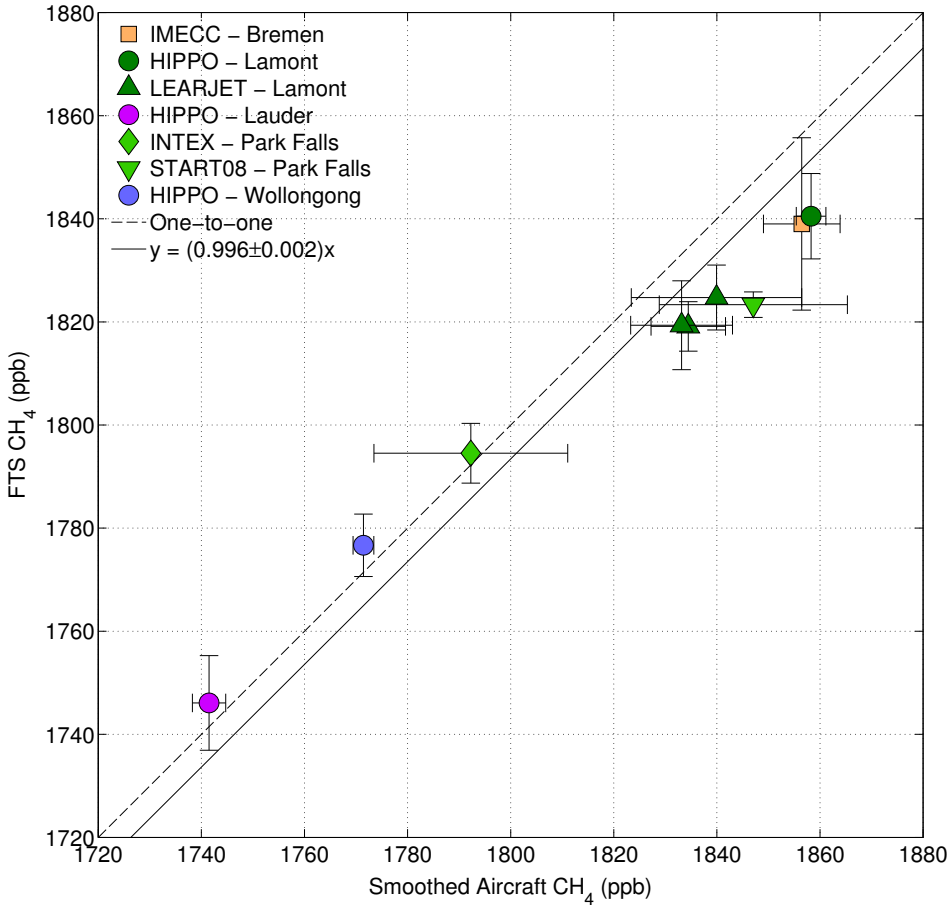

Figure 2.8: Tropospheric CH_4 column comparison for TCCON versus aircraft profiles. Error bars denote the 2σ standard deviation from the daily median (FTS) and the estimated instrument errors and tropospheric uncertainty of the measurements (aircraft).

Additionally, we compared $X^t_{CH_4}$ to long-term in situ flask measurements collected at the Atmospheric Radiation Measurement Program (ARM), Southern Great Plains (SGP) site, near the Lamont TCCON station, and analyzed by the NOAA Earth System Research Laboratory (ESRL). Surface measurements are collected from a 60 m tower, typically once per week on one afternoon, and aircraft samples are collected approximately biweekly with a flight path centered over the tower. The integrated aircraft DMFs are generally higher than the TCCON tropospheric columns, which provide a lower bound to the flask measurements (Figure 2.9a). The partial aircraft columns, restricted to the free troposphere (approximately 3–7 km), are more consistent with the TCCON tropospheric columns. The calibration curve reinforces the distinction between the aircraft tropospheric and partial tropospheric columns when compared to the FTS DMFs at Lamont (Figure 2.9b); while the best

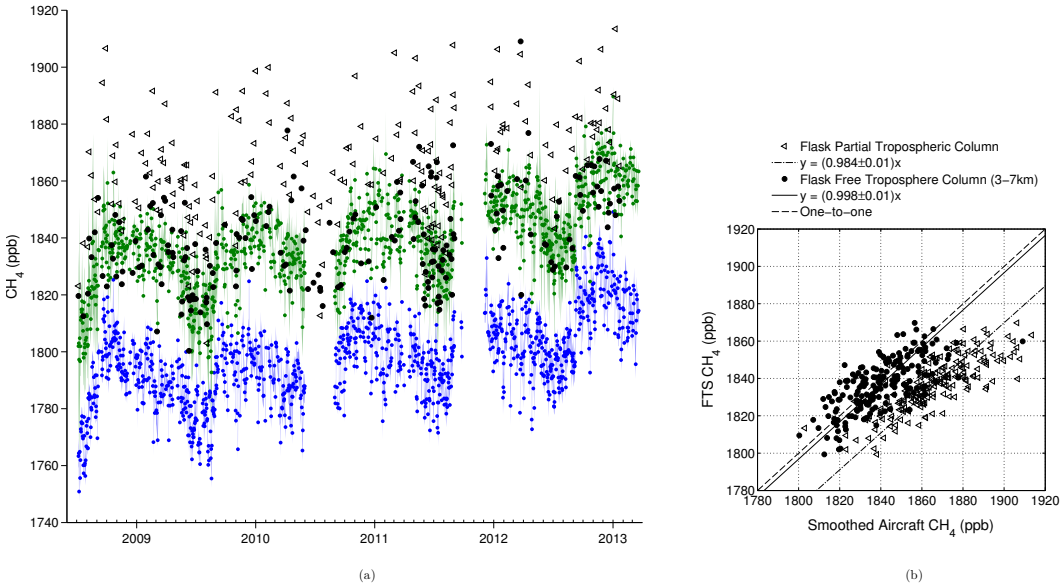

Figure 2.9: **(a)** Daily median column and aircraft CH_4 DMFs at Lamont. Flask partial tropospheric columns integrate CH_4 from the minimum to the maximum altitudes of the aircraft measurement. Flask free troposphere columns integrate CH_4 from the minimum to the maximum altitudes of the aircraft within 3–7 km. Total and tropospheric column DMFs are the same as in Figure 2.4. **(b)** Tropospheric CH_4 column comparison for TCCON versus in situ profiles.

fit slopes, calculated as in (Figure 2.8), are equal within measurement error, the slope of the free troposphere partial column has a smaller offset from the FTS-aircraft one-to-one line.

In situ measurements at the surface are also useful for regions without large local surface sources and if the troposphere is well-mixed, as in New Zealand. We compared Lauder FTS measurements to in situ data at the Baring Head National Institute of Water and Atmospheric Research of New Zealand (NIWA) facility, about 600 km northeast of the TCCON site (41.4°S, 174.9°E, 85 m a.s.l.). The Baring Head flask measurements are collected on a stationary platform at a sampling height of 10 m, analyzed with a flame ionizing detector, and calibrated with the NOAA04 scale (Lowe et al. 1991). The surface measurements are similar to the tropospheric columns, both in terms of the DMF values and the timing of the seasonal cycle (Figure 2.10). The Lauder tropospheric columns are somewhat higher in the late summer and early fall, which could be a function of local CH_4 sources near Lauder, changing wind directions impacting the covariance between the two sites, or seasonal HF variability not captured in the tropospheric column derivation. Given

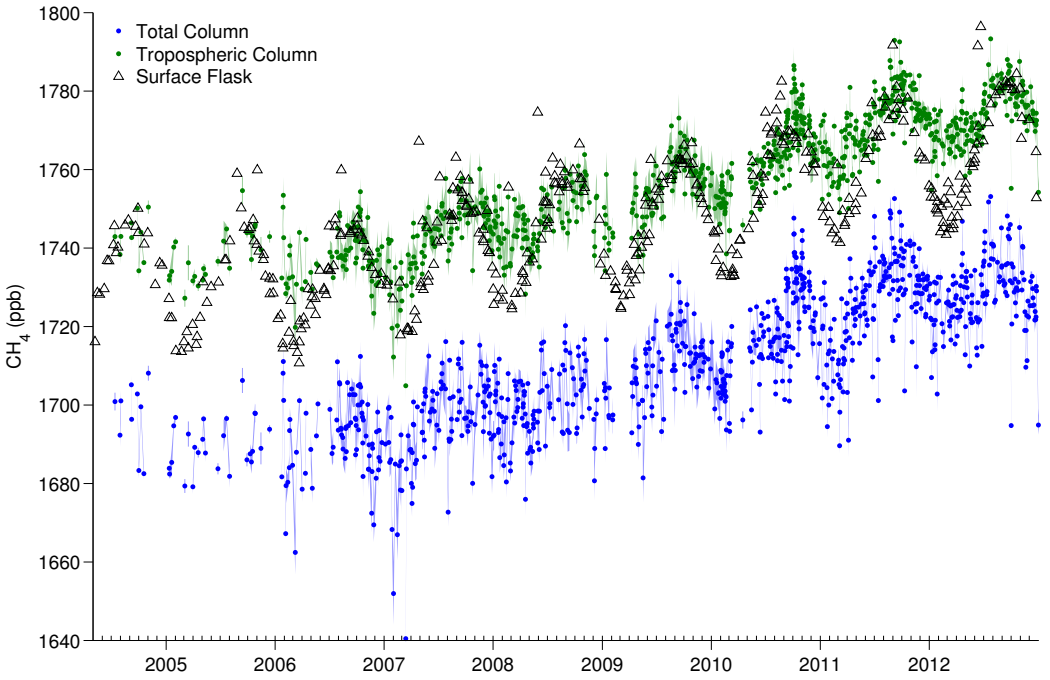

Figure 2.10: Daily median CH_4 DMFs at Lauder (FTS) and Baring Head (flask). Both the 120 HR (June 2004–December 2010) and 125 HR (February 2010–December 2012) instruments are plotted for Lauder. X_{CH_4} and $X^t_{CH_4}$ are as in Figure 2.4.

the relatively large discrepancy of about 10 ppb between the two data sets during those months and the low sensitivity of the tropospheric column to small changes in β, the last of these explanations is the least likely.

2.3.3 Discussion

Inadequate constraints on the global CH_4 budget have been a long-standing problem, and understanding recent trends depends on reliable and frequent observations of tropospheric CH_4 concentrations. By explicitly taking into account the averaging kernels of CH_4 and incorporating temporally and spatially varying estimates of the CH_4–HF relationship, the methodology described here refines earlier tracer proxy methods for estimating stratospheric CH_4. The tropospheric column measurements of CH_4 derived from TCCON X_{CH_4} provide a useful addition to existing data sets used to analyze the global CH_4 cycle and verify chemical transport models.

While the CH_4–HF relationship is robust, the calculation of β still has limitations. The slight non-linearity and seasonal variability of the CH_4–HF relationship could impact the estimation of stratospheric CH_4 loss. Further analysis of ACE-FTS

and other high-frequency stratospheric measurements could produce a statistically significant seasonal cycle to apply to β.

2.4 Consideration of the Boundary Condition for Stratospheric Loss

The TCCON $X^t_{CH_4}$ were updated from Saad et al. (2014) to incorporate the most recent version of the a priori vertical profiles (Toon and Wunch 2014) and retrieval software (GGG2014, Wunch et al. 2015), with several adjustments to both the parameters used and methodology. GGG2014 made several revisions to column retrievals that are relevant to the $X^t_{CH_4}$ calculation, including adding $^{13}CH_4$ linelists, improving estimates of measurement precision, and introducing a secular decrease of 1% annually to the HF priors.

The HF-proxy method for determining $X^t_{CH_4}$ incorporates the relationship between CH_4 and HF in the stratosphere, which is calculated using ACE-FTS data. These CH_4–HF slopes now use updated ACE-FTS version 3.5 measurements with v.1.1 flags (Boone et al. 2013; Sheese et al. 2015). The data quality flags are provided for profile data on a 1 km vertical grid, which uses a piecewise quadratic method to interpolate from the retrievals (Boone et al. 2013). Additionally, the CH_4 and HF measurement errors are now considered in the pressure-weighted linear regression that determines the slopes. All other data processing to produce the CH_4–HF slopes followed methods described in Saad et al. (2014). Figure 2.11 shows the updated annual zonal values used to calculate $\hat{X}^t_{CH_4}$ with Washenfelder et al. (2003) and MkIV (retrieved from `http://mark4sun.jpl.nasa.gov/m4data.html`) values included for reference (c.f. Saad et al. 2014, Figure 2 therein). These updates altered $\hat{X}^t_{CH_4}$ for the sites and time period covered in this paper by less than 2 ppb but reduced the uncertainties of the β values, and thus $\hat{X}^t_{CH_4}$, considerably.

The derivation of the tropospheric column in Washenfelder et al. (2003), Saad et al. (2014), and Wang et al. (2014) implicitly assumed that the CH_4 profile is continuous across the tropopause; however, the boundary condition for stratospheric CH_4 is rather set by tropospheric air transported through the tropical tropopause (Brewer 1949; Dobson 1956). Boering et al. (1996) showed that the concentration of CO_2 directly above the tropopause can be approximated by introducing a two-month phase lag to the average concentration at northern and southern tropical surface sites: Mauna Loa, Hawaii (MLO) and Tutuila, American Samoa (SMO), respectively. As the CH_4 entering the stratosphere originates in both hemispheres and mixes (Boering et al. 1995), stratospheric CH_4 exhibits a smaller interhemispheric gradient than in

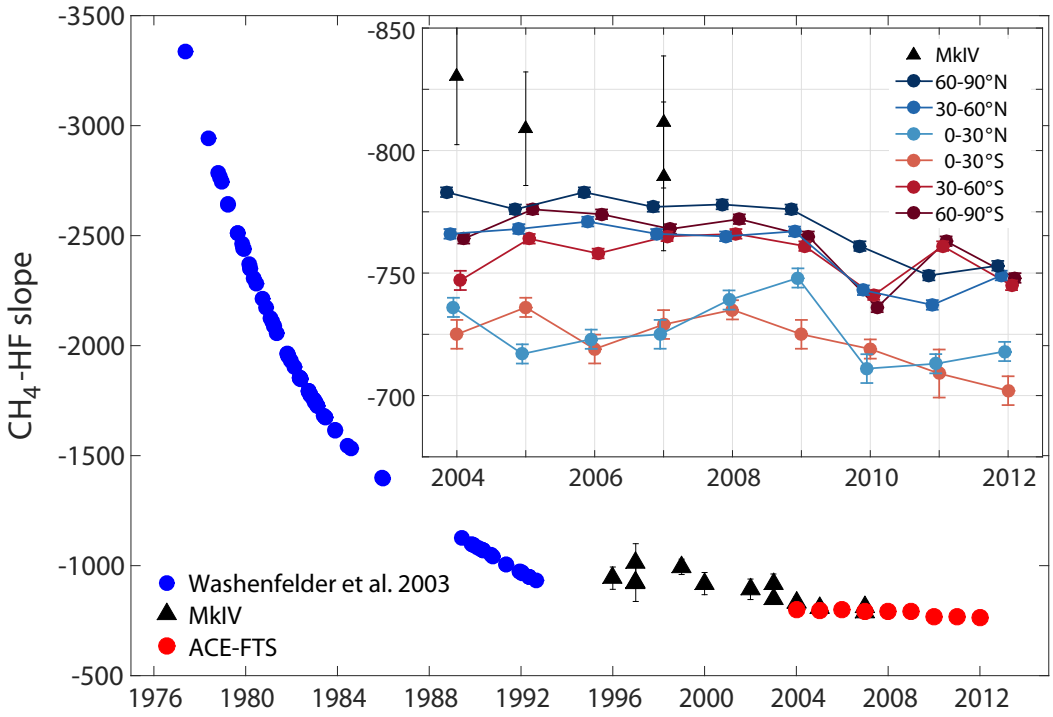

Figure 2.11: Long-term CH_4–HF slopes from Washenfelder et al. (2003), MkIV, and ACE-FTS v. 3.5 measurements. Inset: Time series of zonal pressure-weighted ACE-FTS slopes (β) used to calculate $\hat{X}^t_{CH_4}$ (version xch4tr.tccon.ggg2014.R0), with error bars denoting the 2σ standard error. Zonal slopes are offset each year for visual clarity.

the troposphere: approximately 20 ppb, as calculated from ACE-FTS measurements, versus approximately 50 ppb, taken as the difference at MLO and SMO. To calculate the stratospheric boundary condition for CH_4 we remove the seasonal component of the mean of CH_4 DMFs at MLO and SMO, which are made available through 2014 by the NOAA Earth System Research Laboratory (ESRL) Global Monitoring Division (Dlugokencky et al. 2016). To capture the interhemispheric gradient observed in ACE stratospheric CH_4 measurements, we add and subtract 10 ppb, in the northern and southern extratropics respectively, the limits of which we choose as the Tropic of Cancer (23°N) and the Tropic of Capricorn (23°S). A constant value is chosen in each hemisphere to reflect the rapid mixing time of air from the extra-tropics in the region directly above the tropopause, which Boering et al. (1996) found to be less than one month. Within the tropics, we interpolate the boundary condition as a linear function of altitude such that $x_{CH_4}(P^t) = \bar{x}^s_{CH_4} + \frac{10}{23}\lambda$, where $x_{CH_4}(P^t)$ is the boundary condition at the tropopause, $\bar{x}^s_{CH_4}$ is the mean DMF of CH_4 at the surface, and λ is the latitude of the site.

Assuming hydrostatic equilibrium, the tropospheric column of CH_4, $c^t_{CH_4}$, can be calculated as the integral of the vertical profile, $x_{CH_4} \equiv x_{CH_4}(P)$, from the surface, P^s, to the tropopause, P^t:

$$c^t_{CH_4} = \int_{P^t}^{P^s} x_{CH_4} \frac{dP}{gm} = X^t_{CH_4} \frac{P^s - P^t}{g^t_* m} \tag{2.7}$$

where P is the pressure, g is the gravitational acceleration, g^t_* is the pressure-weighted tropospheric value of g, and m is the mean molecular mass of CH_4 (Washenfelder et al. 2006). The profile of CH_4 in the stratosphere can be expressed as a linear function of pressure altitude, $x_{CH_4}(P) = x_{CH_4}(P^t) + \delta \cdot P$, where $\delta = \frac{dx_{CH_4}}{dP}$ is the stratospheric loss of CH_4. This stratospheric loss term is estimated by the HF-proxy method to produce the retrieved tropospheric column-averaged DMF, $\hat{X}^t_{CH_4}$, such that

$$\hat{X}^t_{CH_4} \frac{P^s}{g_* m} = \hat{c}^t_{CH_4} = \int_0^{P^s} x_{CH_4} \frac{dP}{gm} - \int_0^{P^t} \delta \cdot P \frac{dP}{gm} \tag{2.8}$$

where g_* is the pressure-weighted column average of g. The stratospheric boundary condition can thus be related to the retrieved tropospheric column as

$$\int_0^{P^t} x_{CH_4} \frac{dP}{gm} = \int_0^{P^t} x_{CH_4}(P^t) \frac{dP}{gm} - \hat{c}^t_{CH_4} + \int_0^{P^s} x_{CH_4} \frac{dP}{gm}. \tag{2.9}$$

Given that the total column integration is the sum of the tropospheric and stratospheric partial columns, and substituting Equation 2.9:

$$\int_{P^t}^{P^s} x_{CH_4} \frac{dP}{gm} = \int_0^{P^s} x_{CH_4} \frac{dP}{gm} - \int_0^{P^t} x_{CH_4} \frac{dP}{gm} \tag{2.10}$$

$$= \int_0^{P^s} x_{CH_4} \frac{dP}{gm} - \int_0^{P^t} x_{CH_4}(P^t) \frac{dP}{gm} + \hat{c}^t_{CH_4} - \int_0^{P^s} x_{CH_4} \frac{dP}{gm} \tag{2.11}$$

$$= \hat{c}^t_{CH_4} - \int_0^{P^t} x_{CH_4}(P^t) \frac{dP}{gm} \tag{2.12}$$

$$X^t_{CH_4} \frac{P^s - P^t}{g^t_* m} = \hat{X}^t_{CH_4} \frac{P^s}{g_* m} - x_{CH_4}(P^t) \frac{P^t}{g^0_* m} \tag{2.13}$$

where g^0_* is the pressure-weighted average of g from the tropopause to the top of the atmosphere. While the molecular mass of air changes as a function of water vapor and thus altitude and gravity changes as a function of both altitude and latitude,

assuming constant values of g and m changes $X^t_{\mathrm{CH_4}}$ by less than 2 ppb. Thus, to good approximation these variables can be canceled out:

$$X^t_{\mathrm{CH_4}}[P^s - P^t] = \hat{X}^t_{\mathrm{CH_4}} \cdot P^s - x_{\mathrm{CH_4}}(P^t) \cdot P^t \tag{2.14}$$

$$X^t_{\mathrm{CH_4}} = \frac{\hat{X}^t_{\mathrm{CH_4}} \cdot P^s - x_{\mathrm{CH_4}}(P^t) \cdot P^t}{P^s - P^t}. \tag{2.15}$$

The surface pressure is measured at each site, and the tropopause pressure is calculated from the TCCON prior temperature profiles. The uncertainties associated with the interpolated value of the tropopause height are determined by calculating $X^t_{\mathrm{CH_4}}$ for ±30% of P^t and adding these confidence intervals in quadrature to the precision error of $\hat{X}^t_{\mathrm{CH_4}}$. The aforementioned deseasonalization of $x_{\mathrm{CH_4}}(P^t)$ is an approximation that adds another uncertainty. The signal of the tropospheric seasonal cycle of a trace gas entering the stratosphere is apparent directly above the tropopause and both dampens in amplitude and shifts in time with increasing altitude (Mote et al. 1996). Thus, the stratospheric boundary condition is not truly constant throughout the column, but rather the pressure-weighted sum of these attenuated signals. Calculating $x_{\mathrm{CH_4}}(P^t)$ without removing the seasonality, which provides the maximum impact of this uncertainty, decreases $X^t_{\mathrm{CH_4}}$ by an average of 1 ppb and 4 ppb in the Northern and Southern Hemispheres, respectively, and does not alter the seasonal cycle of $X^t_{\mathrm{CH_4}}$. Moreover, as described below, the mismatch between the calibrated TCCON $X^t_{\mathrm{CH_4}}$ and the in situ aircraft $X^t_{\mathrm{CH_4}}$ does not correlate with season ($R^2 = 0.017$). Thus, we retain the simpler computation of deseasonalized $x_{\mathrm{CH_4}}(P^t)$ in Equation 2.15.

Airmass-dependent artifacts were derived for updated values consistently with the total column CH_4 (Wunch et al. 2015). Removing these artifacts, the $X^t_{\mathrm{CH_4}}$ was then calibrated with in situ aircraft profiles using the same methodology described in Wunch et al. (2010) and including the updates delineated in Wunch et al. (2015) to produce a calibration correction factor of 0.9700 (Figure 2.12). The covariance between the difference between the calibrated TCCON and aircraft $X^t_{\mathrm{CH_4}}$ and several parameters were assessed to ensure biases were not introduced into the measurements. These differences had an uncertainty-weighted correlation coefficient of 0.1 for solar zenith angle and uncertainty-weighted correlation coefficients of less that 0.02 for tropopause and surface pressures, year, and season. Measurement precisions and errors were determined as in Saad et al. (2014), with the additional

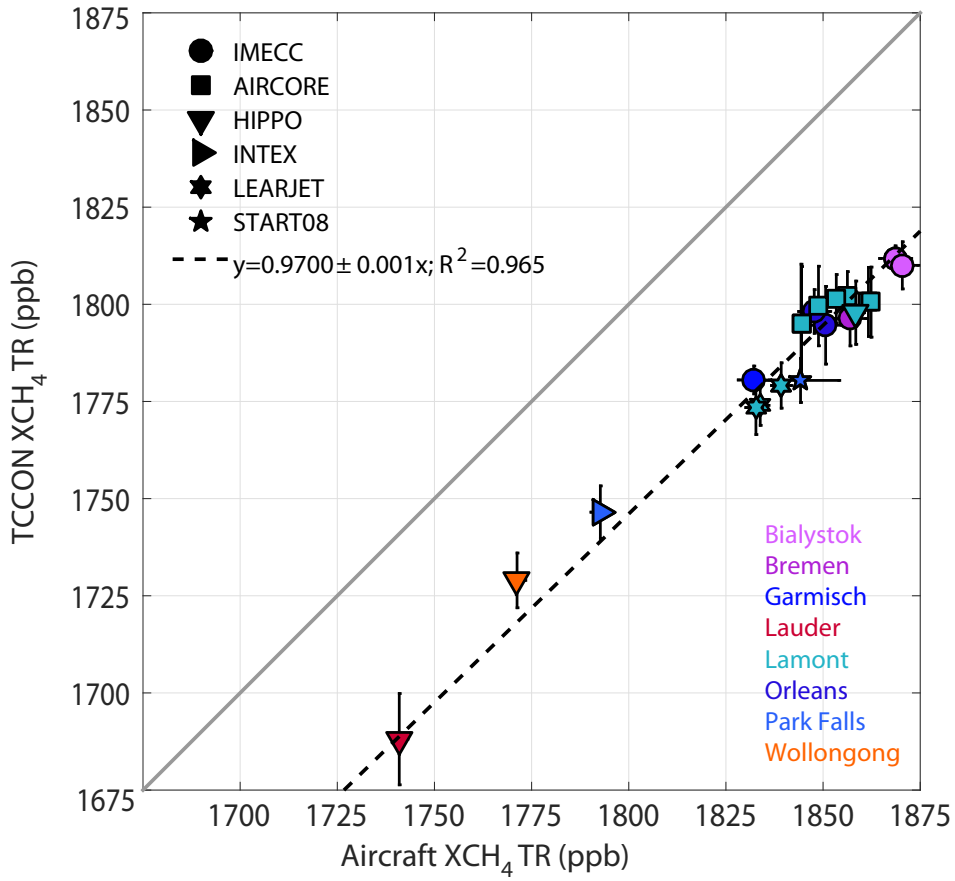

Figure 2.12: Calibration curve of TCCON $X^t_{CH_4}$ (version xch4tr.tccon.ggg2014.R0, c.f. Wunch et al. 2015, Figure 8 therein). Site colors are as in Figure 3.1. Aircraft campaigns are described in Table 6 of Wunch et al. (2015).

uncertainties mentioned in this section included. Individual TCCON sites have median $X^t_{CH_4}$ precisions in the range of 0.1–0.8%, and mean and median precisions are 0.3 and 0.2%, respectively, for all sites through May 2016.

2.5 Further Improvements to Tropospheric Columns

Efforts to improve the precision and accuracy of the TCCON $X^t_{CH_4}$ measurements have led to additional updates to the dataset (version xch4tr.tccon.ggg2014.R1).

Stratospheric CH_4–HF ratios calculated from ACE-FTS measurements have been revised to incorporate the version 3.6 (Bernath 2017) dataset, which extends the available data through 2016 (Table 2.4). The zonal dependence and decadal trend in β is similar to version xch4tr.tccon.ggg2014.R0 values through 2012 (Figure 2.13); however, a convergence in values between the tropics and higher latitudes is apparent from 2013 onward. This feature was not captured in the previously extrapolated β

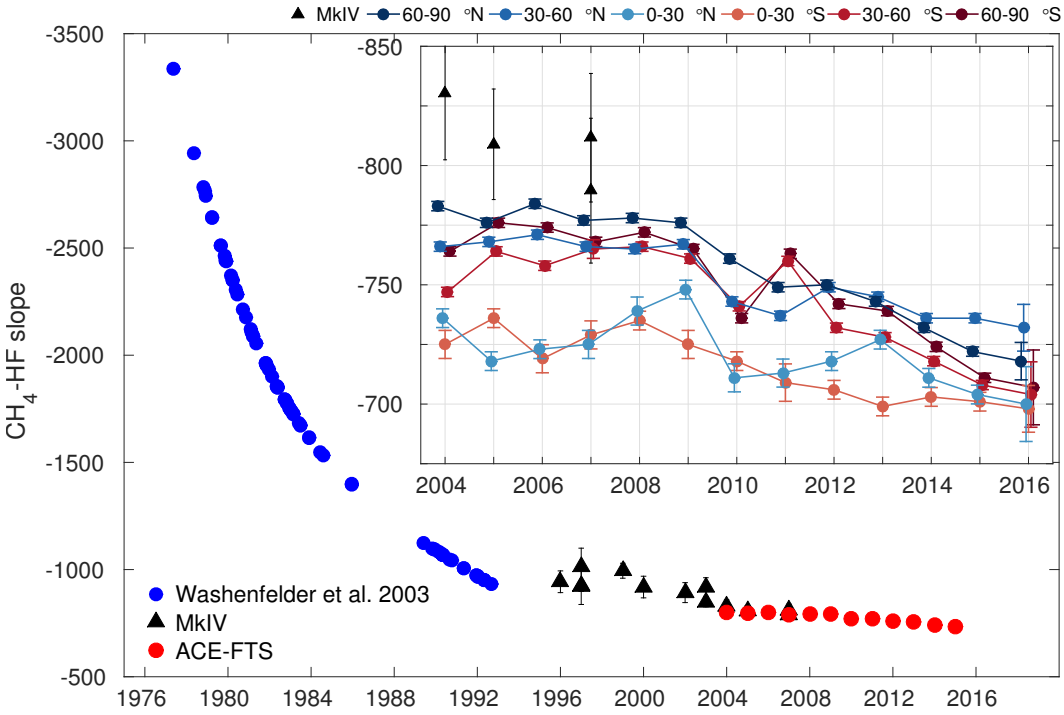

Figure 2.13: Long-term CH_4–HF slopes from Washenfelder et al. (2003), MkIV, and ACE-FTS v. 3.6 measurements. Inset: Time series of zonal pressure-weighted ACE-FTS slopes (β) used to calculate $\hat{X}^t_{CH_4}$ (version xch4tr.tccon.ggg2014.R1), with error bars denoting the 2σ standard error. Zonal slopes are offset each year for visual clarity.

Table 2.4: Annual zonal values (2σ uncertainties) of β from ACE-FTS data. Values after 2015 are extrapolated from the long-term trend.

	60–90°S	30–60°S	0–30°S	0–30°N	30–60°N	60–90°N
2004	-764 (2)	-747 (2)	-725 (6)	-736 (4)	-766 (2)	-783 (2)
2005	-776 (2)	-764 (2)	-736 (4)	-718 (4)	-768 (2)	-776 (2)
2006	-774 (2)	-758 (2)	-719 (6)	-723 (4)	-771 (2)	-784 (2)
2007	-768 (2)	-765 (4)	-729 (6)	-725 (6)	-766 (2)	-777 (2)
2008	-772 (2)	-766 (2)	-735 (4)	-739 (6)	-765 (2)	-778 (2)
2009	-765 (2)	-761 (2)	-725 (6)	-748 (4)	-767 (2)	-776 (2)
2010	-736 (2)	-741 (2)	-718 (4)	-711 (6)	-743 (2)	-761 (2)
2011	-763 (2)	-760 (2)	-709 (8)	-713 (6)	-737 (2)	-749 (2)
2012	-742 (2)	-732 (2)	-706 (4)	-718 (4)	-749 (2)	-750 (2)
2013	-739 (2)	-728 (2)	-699 (4)	-727 (4)	-745 (2)	-743 (2)
2014	-724 (2)	-718 (2)	-703 (4)	-711 (4)	-736 (2)	-732 (2)
2015	-711 (2)	-708 (2)	-701 (4)	-704 (4)	-736 (2)	-722 (2)
2016	-707 (16)	-704 (14)	-698 (10)	-700 (16)	-732 (10)	-718 (8)

values, demonstrating the benefit of incorporating updates to the ACE-FTS dataset. As of February 2017, new occultations are processed with a two-day latency period and integrated into the main datasets within one month, thereby removing the uncertainty associated with the extrapolation in future calculations of $\hat{X}^t_{CH_4}$.

Airmass dependence factors were re-calculated for the updated tropospheric CH_4 columns. These $X^t_{CH_4}$ have also been calibrated using in situ aircraft profiles in accordance with WMO standards (Figure 2.14a), consistently with (Wunch et al. 2015). Although HF is not calibrated, as no WMO-standard profiles of HF exist over the TCCON sites, by calibrating the partial column we can address some of the spectroscopy errors of HF. Calibration curves for X_{CH_4} using the same overpass profiles are also shown for comparison (Figure 2.14b).

The calibrated TCCON $X^t_{CH_4}$ have slightly high values compared to the aircraft $X^t_{CH_4}$, in the range of 6–11 ppb, for solar zenith angles less than 30°̃(Figure 2.15), producing the strongest parameter dependence of $X^t_{CH_4}$ (R^2=0.1). This dependence is less apparent for X_{CH_4} (R^2=0). The difference between calibrated and aircraft $X^t_{CH_4}$ and X_{CH_4} do not exhibit temporal dependence (Figures 2.16a and 2.16b). Additionally, the calibration is not sensitive to the tropopause heights derived from the aircraft temperature and pressure profiles (Figure 2.17b) or those used in the TCCON $X^t_{CH_4}$ boundary condition adjustment (Figure 2.17a).

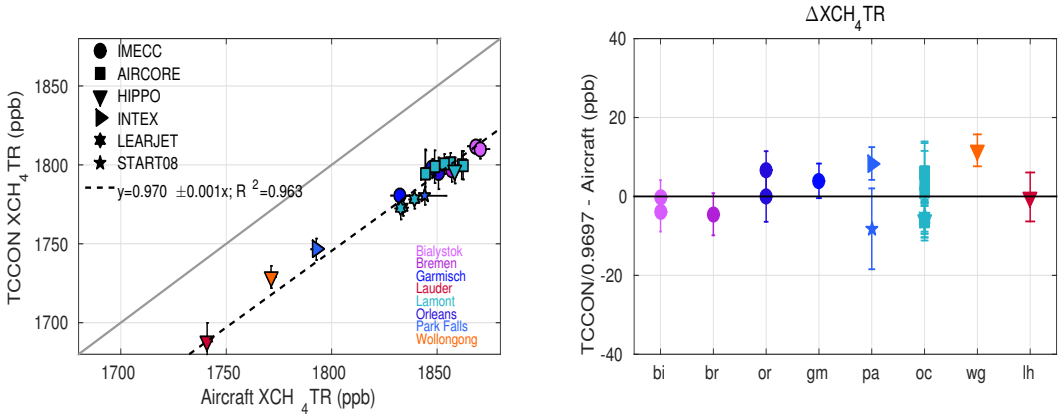

(a) Calibration curves for $X^t_{CH_4}$

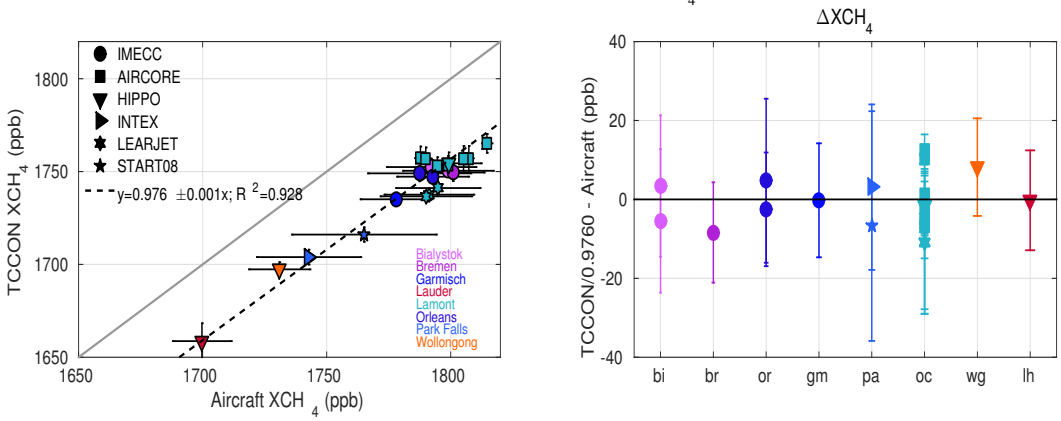

(b) Calibration curves for X_{CH_4}

Figure 2.14: Left: Calibration curves of (a) TCCON $X^t_{CH_4}$ (version xch4tr.tccon.ggg2014.R1) and (b) X_{CH_4} using the same overpass profiles (c.f. Wunch et al. 2015, Figure 8). Right: Difference between calibrated TCCON and aircraft column-averaged DMFs for individual sites, sorted by latitude. Site colors are as in Figure 3.1. Aircraft campaigns are described in Table 6 of Wunch et al. (2015).

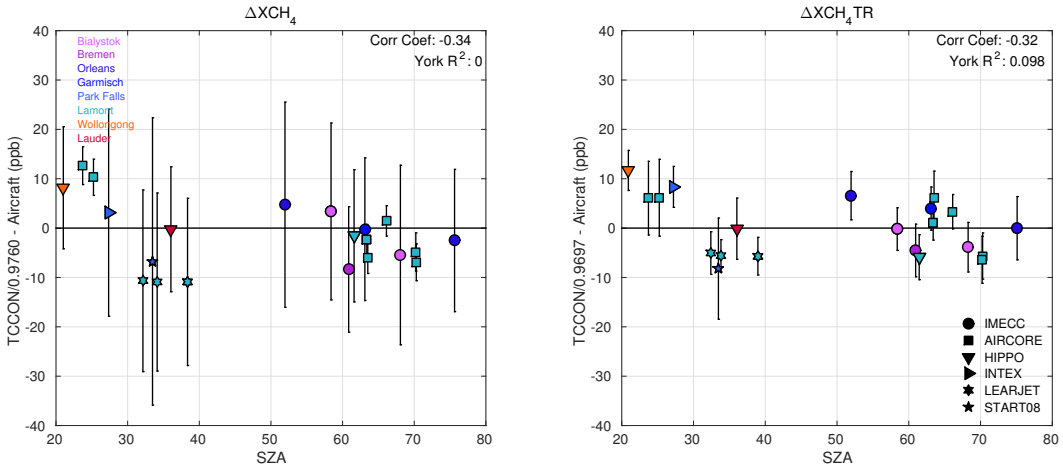

Figure 2.15: Difference between calibrated TCCON and aircraft X_{CH_4} (left) and $X^t_{\mathrm{CH}_4}$ (right) as a function of solar zenith angle. Site colors and aircraft campaign markers are as in Figure 2.14.

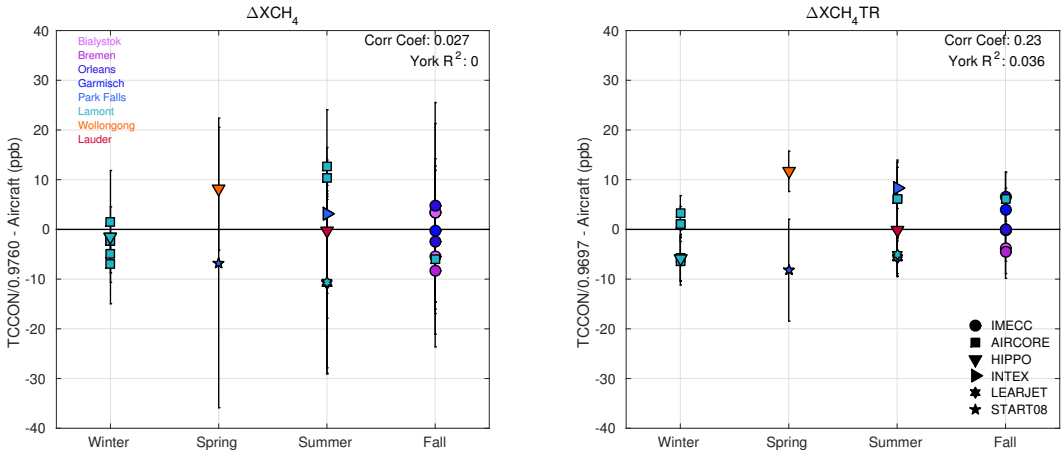

(a) Season

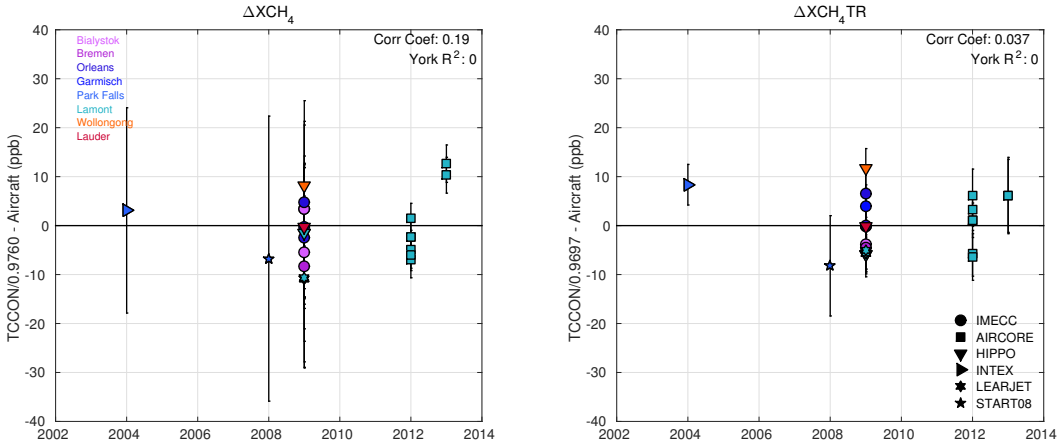

(b) Year

Figure 2.16: Difference between calibrated TCCON and aircraft X_{CH_4} (left) and $X^t_{CH_4}$ (right) as a function of (a) season and (b) year. Site colors and aircraft campaign markers are as in Figure 2.14.

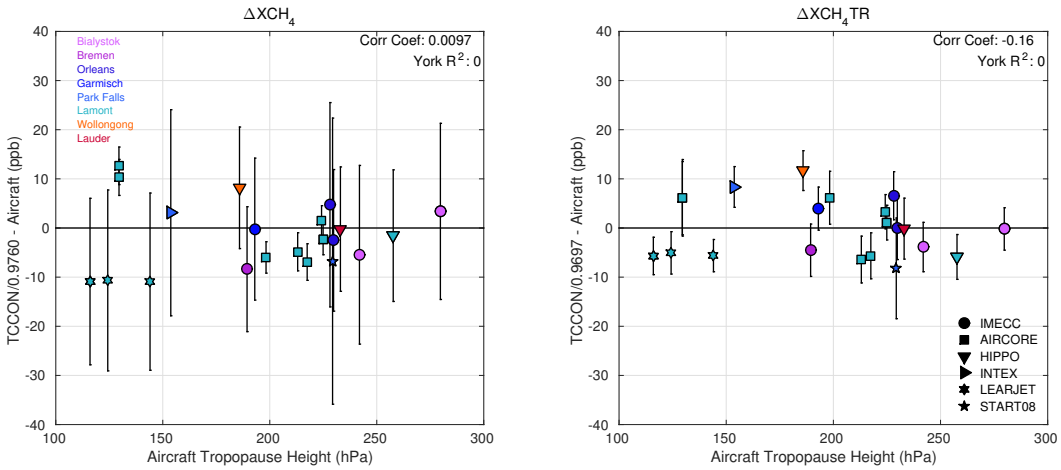

(a) Aircraft Tropopause Height

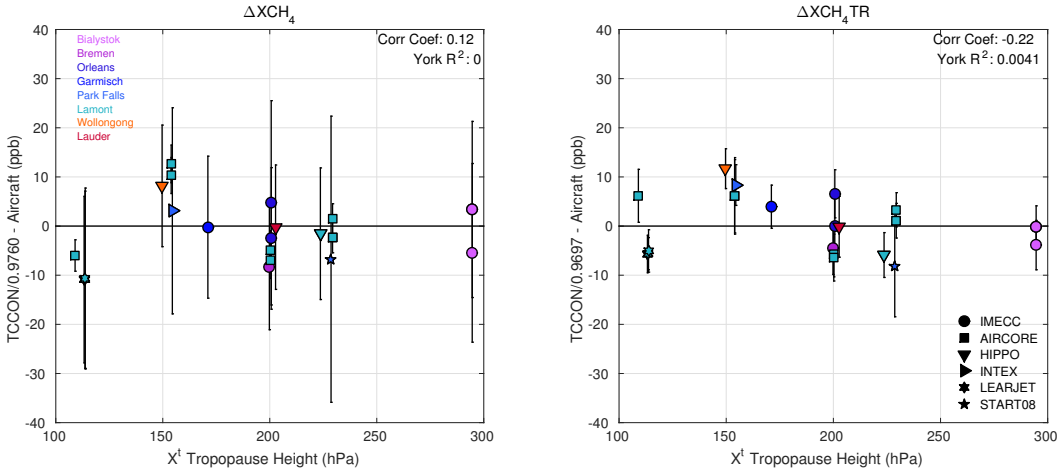

(b) TCCON Tropopause Height

Figure 2.17: Difference between calibrated TCCON and aircraft X_{CH_4} (left) and $X^t_{CH_4}$ (right) as a function of (a) aircraft and (b) TCCON tropopause heights (hPa). Site colors and aircraft campaign markers are as in Figure 2.14.

acknowledgments Support for this research was received from NASA's Carbon Cycle Science program (NNX10AT83G, James Randerson, PI). Part of this work was performed at the Jet Propulsion Laboratory, California Institute of Technology, under contract with NASA. US funding for TCCON comes from NASA grants NNX11AG01G, NAG5-12247, NNG05-GD07G, and NASA Orbiting Carbon Observatory Program. We are grateful to the DOE ARM program for technical support in Lamont and Darwin and Jeff Ayers for technical support in Park Falls. European funding is from GEOMON, InGOS, and IMECC. From 2004 to 2011 the Lauder TCCON program was funded by the New Zealand Foundation of Research Science and Technology contracts CO1X0204, CO1X0703, and CO1X0406. Since 2011 the program has been funded by NIWA's Atmosphere Research Programme 3 (2011/13 Statement of Corporate Intent). Australian funding is from the Australian Research Council, DP0879468 and LP0562346. Funding for the ACE-FTS mission is primarily provided by the Canadian Space Agency. NCEP Reanalysis data are provided by NOAA/OAR/ESRL PSD. SGP aircraft flask data were obtained through the ARM Program sponsored by the US Department of Energy, Office of Science, Office of Biological and Environmental Research and were generated by NOAA-ESRL, Carbon Cycle Greenhouse Gases Group. Baring Head NIWA surface data were provided courtesy of Gordon Brailsford, Dave Lowe, and Ross Martin. We would also acknowledge the contributions of in situ vertical profiles from the HIPPO, IMECC, INTEX, Learjet, and START08 campaigns. Color schemes for Figures 2.1 and 2.3 are from Brewer, Cynthia A., 200x.`http://www.ColorBrewer.org`. K. M. Saad is indebted to Debra Wunch for the numerous codes that served as templates from which the airmass correction and aircraft calibration factors were derived.

Chapter 3

SEASONAL VARIABILITY OF STRATOSPHERIC METHANE: IMPLICATIONS FOR CONSTRAINING TROPOSPHERIC METHANE BUDGETS USING TOTAL COLUMN OBSERVATIONS

3.1 Introduction

Identifying the processes that have driven changes in atmospheric methane (CH_4), a potent radiative forcing agent and major driver of tropospheric oxidant budgets, is critical for understanding future impacts on the climate system. Methane's growth rate, which had been decreasing through the 1990s from about 10 to 0 ppb per year, began to increase again in 2006 and over the past decade has averaged 5 ppb per year (Dlugokencky et al. 2011). Developing robust constraints on the global CH_4 budget is integral to understanding which processes produced these decadal trends (e.g., Bergamaschi et al. 2013; Wecht et al. 2014b; Wecht et al. 2014a; Turner et al. 2015).

One common approach to quantifying changes in the spatial distribution of sources are atmospheric inversions, which incorporate surface fluxes estimated by bottom-up inventories as boundary conditions for a chemical transport model (CTM). The modeled CH_4 concentrations are compared to observations within associated grid boxes, and prior emissions are scaled to minimize differences with measured dry-air mole fractions (DMFs), producing posterior estimates. The accuracy of these optimized emissions depends on how well the CTM simulates atmospheric transport and CH_4 sinks, which are generally prescribed.

Pressure-weighted total column-averaged DMFs (X_{gas}) provide a relatively new constraint and have previously been shown to improve estimates of regional and interhemispheric gradients in trace gases (Yang et al. 2007). Infrared spectrometers can measure CH_4 DMFs ($X_{\mathrm{CH_4}}$) from ground-based sites, such as those in the Total Carbon Column Observing Network (TCCON) and Network for the Detection of Atmospheric Composition Change (NDACC), and satellites, including SCanning Imaging Absorption spectroMeter for Atmospheric CartograpHY (SCIAMACHY) (Bergamaschi et al. 2007), Greenhouse gases Observing SATellite (GOSAT) (Parker et al. 2011), and the upcoming TROPOspheric Monitoring Instrument (TROPOMI) (Butz et al. 2012). These observations complement surface in situ measurements

because they add information about the vertically averaged profile and are sensitive in the free troposphere (Yang et al. 2007). Additionally, they complement aircraft observations by measuring trace gases at higher temporal frequency, although they share the limitation of not measuring in inclement weather. Satellite measurements add global coverage that can fill in gaps where in situ observations are sparse. Fraser et al. (2013) found that assimilating GOSAT CH_4 columns into the GEOS-Chem CTM with an ensemble Kalman filter reduced posterior emissions uncertainties by 9–48% for individual source categories and by more than three times those of inversions that only assimilated surface data for most regions. Wecht et al. (2014a) determined from their analysis of observing system simulation experiments (OSSEs) that TROPOMI's daily frequency and global coverage performs similarly to aircraft campaigns on sub-regional scales, and could provide a constraint on California's CH_4 emissions similar to CalNex aircraft observations (Santoni et al., 2014; Gentner et al., 2014).

Incorporating total columns into modeling assessments can also be used to diagnose systematic issues with model transport. For example, comparing carbon dioxide (CO_2) from TCCON and TransCom (Baker et al. 2006), Yang et al. (2007) found that most models included in the comparison lack sufficiently strong vertical exchange between the planetary boundary layer (PBL) and the free troposphere, thereby dampening the seasonal cycle amplitude of X_{CO_2}. The limitations of models to accurately represent vertical transport can lead to radically different spatial distributions of fluxes; Stephens et al. (2007) found, for example, that the northern terrestrial carbon land sink and tropical emissions were overestimated by 0.9 and 1.7 PgC year^{-1}, respectively, when comparing models to aircraft CO_2 profiles. More recent studies attribute to model transport errors the tendency of simulated CH_4 in the Southern Hemisphere to be higher at the surface than the free troposphere, in contrast with measurements (Fraser et al. 2011; Patra et al. 2011).

Tropospheric CH_4 typically does not vary radically with height above the PBL; above the tropopause, however, the vertical profile of CH_4 exhibits a rapid decline with altitude as a result of its oxidation and the lack of any source beyond advection from the troposphere. Fluctuations in stratospheric dynamics, including the height of the tropopause, change the contribution of the stratosphere to the total column. CH_4 profiles with similar tropospheric values can thus have significant differences in X_{CH_4} (Saad et al. 2014; Washenfelder et al. 2003; Wang et al. 2014).

Provided that simulations replicate seasonal and zonal variability of stratospheric

CH_4 loss, tropopause heights, and vertical exchange across the upper troposphere and lower stratosphere (UTLS), posterior flux estimates from inversions incorporating X_{CH_4} measurements would not be sensitive to stratospheric processes. However, most models do not accurately represent stratospheric transport, producing low age-of-air values and zonal gradients in the subtropical lower stratosphere that are less steep than observations (Waugh and Hall 2002). The TransCom-CH_4 CTM intercomparison assessment of transport using sulfur hexafluoride (SF_6) showed a strong correlation between the stratosphere–troposphere exchange (STE) rate and the model's CH_4 budget, and a weaker correlation between the CH_4 growth rate and vertical gradient in the model's equatorial lower stratosphere (Patra et al. 2011). These forward model dependencies of CH_4 concentrations on vertical transport, both within the troposphere and across the tropopause, have the potential to introduce substantial errors in atmospheric inversions. As temporal and spatial biases in a model's vertical profile will alias into posterior emissions, inversions that incorporate total column measurements must ensure that the stratosphere is sufficiently well described so as to not introduce spurious seasonal, zonal, and interhemispheric trends in CH_4 concentrations and consequently emissions.

In this analysis, we identify systematic model errors in the seasonal cycle and spatial distribution of CH_4 DMFs by comparing TCCON total and tropospheric columns (Saad et al. 2014) to vertically integrated profiles derived from the GEOS-Chem CTM (Bey et al. 2001; Wang et al. 2004; Wecht et al. 2014b). We assess the impact of errors in the characterization of stratospheric processes on the assimilation of X_{CH_4} and resulting posterior emissions estimates. In Section 3.2 we describe the TCCON column measurements, and in Section 3.3 we outline the GEOS-Chem setup and simulation characteristics. In Section 3.4 we present the results of the measurement–model comparison. In Section 3.5 we compare the base case simulation to one in which emissions do not vary within each year and quantify the sensitivity of source attribution of the biggest seasonal emissions sector, wetlands, to the tropospheric seasonal delay.

3.2 Tropospheric Methane Columns

TCCON has provided precise measurements of X_{CH_4} and other atmospheric trace gases for over ten years (Wunch et al. 2011a; Wunch et al. 2015). Developed to address open questions in carbon cycle science, the earliest sites are located in Park Falls, Wisconsin, United States and Lauder, New Zealand at about 45° north and south, respectively. Since 2004, the ground-based network of Fourier transform

Figure 3.1: Map of TCCON sites used in this analysis. Site colors are on a spectral color scale in order of latitude, with Northern Hemisphere sites designated by cool colors and Southern Hemisphere sites designated by warm colors.

spectrometers has expanded greatly.

X_{CH_4} are processed with the current version of the TCCON software, GGG2014, to be consistent, and thereby comparable, across sites. Total column retrievals are generated with the GFIT nonlinear least-squares fitting algorithm, which calculates the best spectral fit of the solar absorption signal to an a priori vertical profile and outputs a scaling factor. The pressure-weighted integration of the scaled a priori profile produces column abundances, which are then divided by the dry air column, calculated using concurrently retrieved oxygen (O_2) columns (Wunch et al. 2010; Wunch et al. 2011a; Wunch et al. 2015). Trace gas a priori profiles are derived with empirical models, which are generated incorporating aircraft and balloon in situ and satellite measurements (see Wunch et al. 2015, for a complete list), and for CH_4 include a secular increase of 0.3% per year and an interhemispheric gradient in the altitude dependence of the vertical profiles (Toon and Wunch 2014). These models are fit to daily noontime National Centers for Environmental Protection and National Center for Atmospheric Research (NCEP/NCAR) reanalysis pressure grids (Kalnay et al. 1996), interpolated to the surface pressure measured real-time on site. Because the profile of CH_4 drops off rapidly in the stratosphere, the accuracy of the a priori shape, and thus the retrieved column, depends on correctly determining the tropopause.

Tropospheric columns have been shown to represent the magnitude and seasonality of in situ measurements (Saad et al. 2014; Washenfelder et al. 2003; Wang et al. 2014). The tropospheric CH_4 column-averaged DMFs ($X^t_{CH_4}$) are derived by the

hydrogen fluoride (HF) proxy method described in Saad et al. (2014), which uses the relationship between CH_4 and HF in the stratosphere, derived from ACE-FTS satellite measurements (Bernath 2005; De Mazière et al. 2008; Mahieu et al. 2008; Waymark et al. 2014), to calculate and remove the stratospheric contribution to X_{CH_4}. The $X^t_{CH_4}$ used in this analysis have been processed consistently with the GGG2014 TCCON products, with air-mass dependence and calibration factors calculated for and applied to $X^t_{CH_4}$ (Wunch et al. 2010; Wunch et al. 2015). Additional details about the tropospheric CH_4 measurements can be found in Section 2.4.

With the exception of Eureka and Sodankylä, which are highly influenced by the stratospheric polar vortex, all TCCON sites that provide measurements before December 2011 are included in this analysis (Figure 3.1). Table 3.1 lists locations and data collection start dates for each of the sites.

Table 3.1: TCCON sites, coordinates, altitudes, measurement start dates, locations, and data used in this analysis.

Site	Latitude (°)	Longitude (°)	Altitude (km)	Start date	Location	Data reference
Bialystok	53.2	23.0	0.18	Mar 2009	Bialystok, Poland	Deutscher et al. (2014)
Bremen	53.1	8.9	0.03	Jan 2007	Bremen, Germany	Notholt et al. (2014)
Karlsruhe	49.1	8.4	0.11	Apr 2010	Karlsruhe, Germany	Hase et al. (2014)
Orleans	48.0	2.1	0.13	Aug 2009	Orleans, France	Warneke et al. (2014)
Garmisch	47.5	11.1	0.75	Jul 2007	Garmisch, Germany	Sussmann and Rettinger (2014)
Park Falls	45.9	-90.3	0.47	Jan 2005	Park Falls, WI, USA	Wennberg et al. (2014d)
Lamont	36.6	-97.5	0.32	Jul 2008	Lamont, OK, USA	Wennberg et al. (2014c)
JPL	34.2	-118.2	0.39	Jul 2007	Pasadena, CA, USA	Wennberg et al. (2014a) and Wennberg et al. (2014b)
Saga	33.2	130.3	0.01	Jul 2011	Saga, Japan	Kawakami et al. (2014)
Izaña	28.3	-16.5	2.37	May 2007	Tenerife, Canary Islands	Blumenstock et al. (2014)
Darwin	-12.4	130.9	0.03	Aug 2005	Darwin, Australia	Griffith et al. (2014a)
Réunion Island	-20.9	55.5	0.09	Sep 2011	Saint-Denis, Réunion	De Maziere et al. (2014)
Wollongong	-34.4	150.9	0.03	Jun 2008	Wollongong, Australia	Griffith et al. (2014b)
Lauder	-45.0	169.7	0.37	Jan 2005	Lauder, New Zealand	Sherlock et al. (2014a, 2014b)

3.3 GEOS-Chem model

Model comparisons use the offline CH_4 GEOS-Chem version 9.02 at $4° \times 5°$ horizontal resolution on a reduced vertical grid (47L). CH_4 loss is calculated on 60 min intervals and is set by annually invariable monthly 3-D fields: hydroxyl radical (OH) concentrations in the troposphere (Park et al. 2004) and parameterized CH_4 loss rates per unit volume in the stratosphere (Considine et al. 2008; Allen et al. 2010; Murray et al. 2012). Emissions are released at 60 min time steps and are provided by the GEOS-Chem development team for 10 sectors: (i) gas and oil, (ii) coal, (iii) livestock, (iv) waste, (v) biofuel and (vi) other anthropogenic annual emissions from EDGAR v4.2 (European Commission Joint Research Centre, Netherlands Environmental Assessment Agency 2011; Wecht et al. 2014b), (vii) other natural annual emissions from Fung et al. (1991b), (viii) rice agriculture (European Commission Joint Research Centre, Netherlands Environmental Assessment Agency 2011) and (ix) wetland (Pickett-Heaps et al. 2011) monthly emissions, which incorporate GEOS5 annual and monthly mean soil moisture values, and (x) biomass burning daily emission from GFED3 estimates (Mu et al. 2011; Werf et al. 2010). Loss via soil absorption (Fung et al. 1991b), set annually, is subtracted from the total emissions at each time step.

3.3.1 Model Setup

We initialized zonal CH_4 distributions with GGG2014 data version a priori profiles (Toon and Wunch 2014) produced at horizontal grid centers, which we adjusted vertically to match the zonally averaged daily mean model's tropopause, derived from the National Aeronautics and Space Administration Global Modeling and Assimilation Office (NASA/GMAO) Goddard Earth Observing System Model, Version 5 (GEOS5). The model was run from December 2003, the first month in which GEOS5 meteorological data were available, to June 2004, the beginning of the TCCON time series; we then ran the model repeatedly over the June 2004–

Table 3.2: Sensitivity experiments

Simulation name	Description	CH_4 lifetime (years)	Final CH_4 burden (Tg)
Base	Default OH and emissions	9.55	4825
Aseasonal	Constant monthly emission rates	9.57	4872
Updated OH	Monthly OH fields from standard chemistry + biogenic VOCs	8.53	4828

May 2005 time frame, which allowed us to make comparisons with the TCCON data at Park Falls and Lauder, until CH_4 concentrations reached equilibrium. A number of perturbation experiments were run in this way to quantify the sensitivity of CH_4 distribution and seasonality to the offline OH fields, prescribed emissions, and tropopause levels (Table 3.2). These model experiments are described in greater detail in Appendix 3A.

Using CH_4 fields for 1 January 2005 from the equilibrium simulation as initial conditions, model daily mean CH_4 mole fractions were computed through 2011. In addition to the default emissions scheme, an aseasonal simulation setup, in which rice, wetland, and biomass burning emissions were disabled and aseasonal emissions scaled up such that total annual zonal fluxes approximate those in the base simulation, was similarly run to equilibrium and used as initial conditions for the 2005–2011 run. The model infrastructure posed difficulties for setting the seasonally varying fluxes constant throughout each year; thus we implement this scaling technique as an alternative to assess first-order impacts of emission seasonality. The resulting changes to the spatial distribution of CH_4 emissions are shown in Figure 3.11.

Versions of GEOS-Chem prior to v.10 have inconsistencies in wet versus dry definitions of pressure, temperature, and air mass, which propagate into model diagnostics and conversions calculated using these terms. As a consequence, CH_4 concentrations are output assuming air masses that include water vapor but calculated with the molar mass of dry air. To correct for this discrepancy, model output was converted to dry mole fractions. For all comparisons in this analysis model CH_4 DMFs are calculated taking into account the GEOS-5 specific humidity, q_s (in units of $g_{H_2O}\,kg_{air}^{-1}$), such that

$$x_{CH_4,dry} = \frac{x_{CH_4}}{1 - q_s \times 10^{-3}} \tag{3.1}$$

where X_{CH_4} is the model profile in mole fractions. Dry air profiles were derived by subtracting the water vapor mole fraction, also calculated from the GEOS-5 specific humidity, from the total air mass at each pressure level, as in Wunch et al. (2010) and Geibel et al. (2012).

For comparisons with column measurements, model vertical profiles were smoothed with corresponding TCCON CH_4 averaging kernels, interpolated for the daily mean solar zenith angles, and prior profiles, scaled with daily median scaling factors, following the methodology in Rodgers and Connor (2003) and Wunch et al. (2010). Averaging kernels and prior profiles were interpolated to the model's pressure grid,

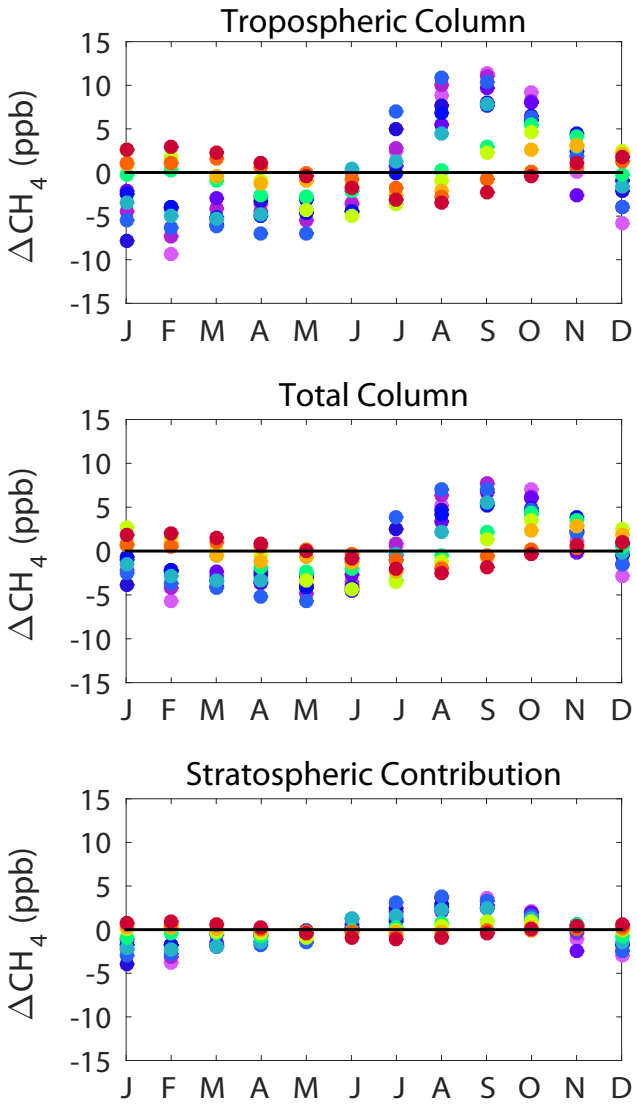

Figure 3.2: Seasonality of the difference between base and aseasonal CH_4 for tropospheric, total and stratospheric contribution to total columns. Site colors are as in Figure 3.1.

and all terms in the smoothing equation were interpolated to daily mean surface pressures measured at each site. Tropospheric columns were integrated in the same manner as the total columns up to the grid level completely below the daily mean tropopause, consistent with how GEOS-Chem partitions the atmosphere in the offline CH_4 simulation. To test the dependence of our results on the chosen vertical integration level, tropospheric columns were also calculated assuming the tropopause was one and two grid cells above this level. While $X^t_{CH_4}$ changed slightly, by a median of about 1 and 5 ppb for a one and two-level increase respectively, shifting the tropopause did not alter the findings discussed in this paper. A description

of the model smoothing methodology and assumptions is provided in Appendix 3B. The stratospheric contribution to the total column, which is calculated as the residual between the $X^t_{CH_4}$ and X_{CH_4}, is the amount by which the stratosphere attenuates X_{CH_4} via stratospheric loss and transport (ref. Appendix 3C for the derivation).

3.3.2 Model Features

The seasonal amplitude of the differences between base and aseasonal simulations are small — within ±4 ppb — for all vertical levels in the Southern Hemisphere (Figure 3.2). In the Northern Hemisphere, however, the difference is much larger and primarily impacts the troposphere, where it varies between −10 and +13 ppb. The insensitivity of the stratosphere to the seasonality of emissions is due to the common source of stratospheric air in the tropics (Boering et al. 1995) and the loss of seasonal information as the age of air increases (Mote et al. 1996).

Due to the relatively short photochemical lifetime of CH_4 in the stratosphere, about 22 months in the base simulation, stratospheric CH_4 concentrations stabilize much more quickly than in the troposphere (Figure 3.3a). This rapid response time of the stratosphere occurs regardless of perturbations to the troposphere, such as the seasonality of emissions (Figure 3.3b) or tropospheric OH fields (Figure 3.3c). In both hemispheres the differences between the base and experimental simulations asymptotically approach steady state with seasonal variability over a decade in the troposphere, but oscillate seasonally around a constant mean in the stratosphere.

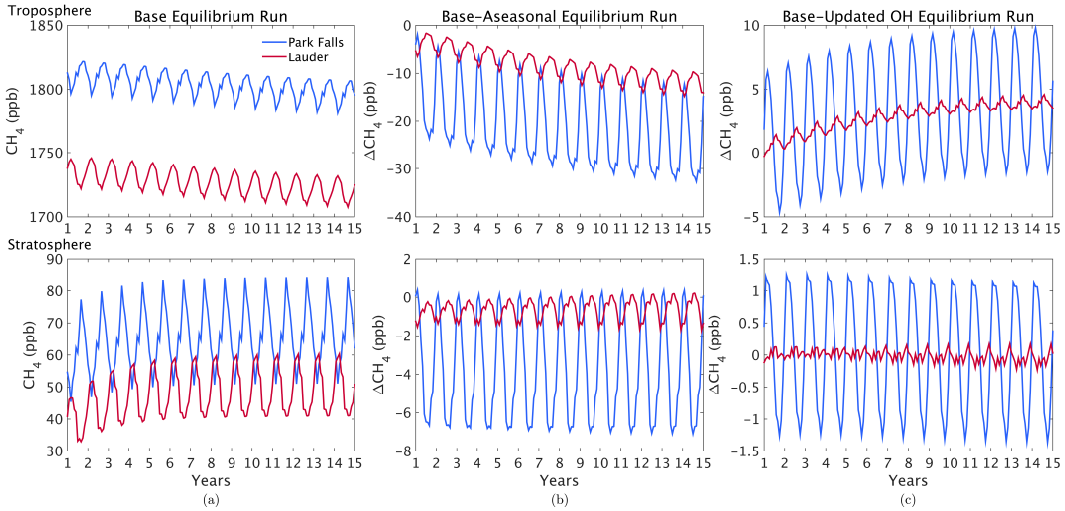

Figure 3.3: Smoothed daily mean $X^t_{CH_4}$ and stratospheric contribution to X_{CH_4} at Park Falls (blue) and Lauder (red) for **(a)** base equilibrium simulation and the difference between the base and **(b)** aseasonal and **(c)** updated OH simulations.

Stratospheric differences between simulations are considerably smaller than the seasonal amplitude of the base run: within 6 and 1 ppb, respectively, versus a seasonal range of 30 ppb at Park Falls. By contrast, $X^t_{CH_4}$ have differences within 30 and 10 ppb, respectively, versus a seasonal range of 20 ppb at Park Falls. The stratosphere at Lauder is even less sensitive to tropospheric perturbations.

3.4 Measurement–Model Comparison

The TCCON daily median and GEOS-Chem daily mean CH_4 column-averaged DMFs demonstrate a strong interhemispheric difference for $X^t_{CH_4}$ and X_{CH_4} in both the base and aseasonal simulations (Figure 3.4). The Northern Hemisphere $X^t_{CH_4}$ slope deviates from the one-to-one line more than the X_{CH_4} slope (0.60 ± 0.02 versus 0.86 ± 0.03), and the correlation coefficients are equivalent ($R^2 = 0.41$), which indicates that the poorer agreement between measurements and models in the troposphere drives the scatter in the total column.

The stratospheric contribution comparison between TCCON and the base simulation for the Northern Hemisphere sites has an equivalent slope (0.60 ± 0.1) and higher correlation coefficient ($R^2 = 0.68$) compared to $X^t_{CH_4}$ (Figure 3.4c). GEOS-Chem's larger stratospheric contribution to the total column, coupled with lower tropospheric values, depresses X_{CH_4}. Because this effect on X_{CH_4} occurs more at higher latitudes, zonal errors in the model's stratosphere balances those in the troposphere. The result is better measurement–model agreement in the total columns.

The aseasonal simulation produces lower slopes and correlation coefficients for, $X^t_{CH_4}$ (slope $= 0.42 \pm 0.02$, $R^2 = 0.32$), X_{CH_4} (slope $=0.60 \pm 0.03$, $R^2 = 0.26$), and the stratospheric contribution (slope $= 0.52 \pm 0.01$, $R^2 = 0.66$) in the Northern Hemisphere. Removing the seasonality of emissions increases both measurement–model differences and scatter, as we would expect given the seasonality of Northern Hemisphere emissions noted in bottom-up studies (Kirschke et al. 2013). The aseasonal simulation also reduces the offset between TCCON and GEOS-Chem, whereby modeled $X^t_{CH_4}$ and X_{CH_4} are systematically low. TransCom-CH_4 showed that GEOS-Chem CH_4 concentrations tend to be lower than the model median, and much lower than the range of other models when using the same OH fields (Patra et al. 2011). The aseasonal emissions used in this analysis likely reduce this documented imbalance with the model's tropospheric OH fields.

The X_{CH_4} and $X^t_{CH_4}$ regression equations across Southern Hemisphere sites are nearly equivalent, which suggests that the Southern Hemisphere is not as impacted

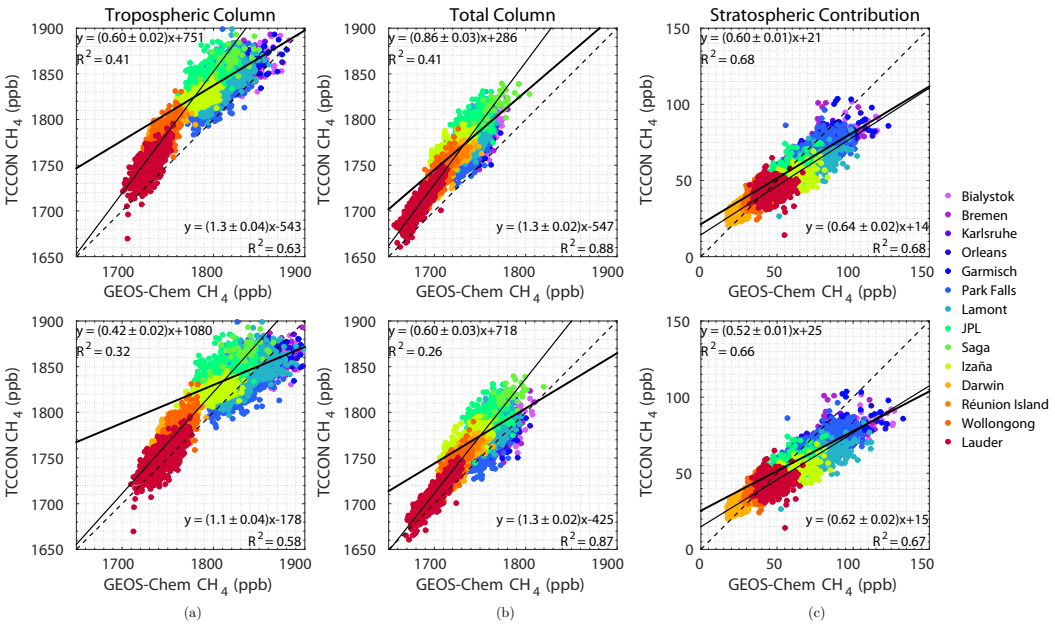

Figure 3.4: Daily median TCCON and smoothed daily mean GEOS-Chem base (top) and aseasonal (bottom) DMFs for **(a)** $X^t_{\mathrm{CH_4}}$, **(b)** $X_{\mathrm{CH_4}}$, and **(c)** stratospheric contribution. Site colors are as in Figure 3.1. Northern Hemisphere least squares regression equations are in the top left, and Southern Hemisphere least squares regression equations are in the bottom right of each plot. Dashed lines mark the one-to-one lines.

by the STE errors as the Northern Hemisphere. This consistency between $X_{\mathrm{CH_4}}$ and $X^t_{\mathrm{CH_4}}$ could also be a function of the zonal dependence of the stratospheric error: whereas more than half of the Northern Hemisphere sites are north of 45°N, the most poleward site in the Southern Hemisphere is located at 45°S. The increased scatter associated with the slightly lower $X^t_{\mathrm{CH_4}}$ R^2 value of 0.63, compared to the $X_{\mathrm{CH_4}}$ R^2 value of 0.88, does indicate that the Southern Hemisphere is not exempt from model errors associated with emissions, the OH distribution, or transport. The lower $X^t_{\mathrm{CH_4}}$ slope of the aseasonal simulation (1.1 versus 1.3) illustrates the influence of emissions: removing their seasonality leads to better measurement–model agreement, evidenced by a slope closer to both the one-to-one line and the zero-intercept. We hypothesize that either the seasonality of Southern Hemispheric emissions is too strong or, more likely, errors in the Northern Hemispheric seasonality of emissions drive measurement–model mismatch in the Southern Hemisphere via interhemispheric transport. If this effect was solely due to a changed emissions distribution, we would expect the $X_{\mathrm{CH_4}}$ slope to also change for the Southern Hemisphere sites, if only slightly; instead the slope is equivalent to the base simulation $X^t_{\mathrm{CH_4}}$ and

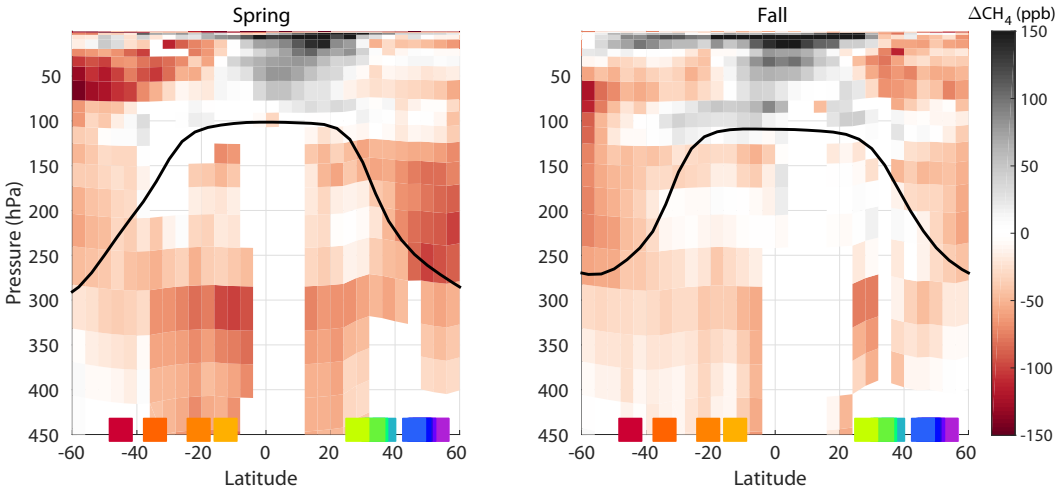

Figure 3.5: Zonally averaged ACE minus GEOS-Chem climatological CH_4 mole fractions for boreal spring and fall. Black line represents the mean zonal tropopause level. Site colors of squares on the x axis are as in Figure 3.1.

X_{CH_4} slopes, and $R^2 = 0.87$, only marginally less than the base simulation X_{CH_4} correlation coefficient.

The stratospheric contribution regression equations differ only slightly between the base and aseasonal simulations: $(0.64 \pm 0.02)\,x + 14$, $R^2 = 0.68$, versus $(0.62 \pm 0.02)\,x + 15$, $R^2 = 0.67$. The insensitivity of both the stratospheric contribution and the total columns in the Southern Hemisphere to perturbations in the seasonality of tropospheric emissions could be driven by the smaller vertical gradient across the UTLS that results from the influence of Northern Hemispheric air both in the free troposphere (Fraser et al. 2011) and the stratosphere (Boering et al. 1995). This effect would also support the interpretation of Northern Hemispheric emission errors driving disagreement between observations and the model in the Southern Hemisphere.

In the troposphere, CH_4 increases from south to north; the stratospheric contribution of CH_4, however, increases from the Equator to the poles due to the zonal gradient in tropopause height. In the Northern Hemisphere total column, the zonal gradient largely disappears: at high latitudes, the larger tropospheric emissions balances the larger stratospheric contribution. By contrast, zonal gradients in the Southern Hemisphere troposphere and stratosphere are additive, and greater south to north differences are apparent in the total column.

Figure 3.5 illustrates how the model differs from ACE-FTS CH_4 measurements in the stratosphere over boreal spring (March–April–May) and fall (September–October–

November). Except above the tropical tropopause, CH_4 is considerably lower in the ACE-FTS climatology (v. 2.2, Jones et al. 2012) compared to GEOS-Chem. The difference varies both with altitude and latitude, especially in the Northern spring poleward of 40°N. The vertical gradient is the least pronounced in Lauder, where the stratospheric contributions of TCCON and GEOS-Chem fall most closely to the one-to-one line (Figure 3.4). The low CH_4 in the tropical mid and upper stratosphere in GEOS-Chem could be a result of too-weak vertical ascent to the stratosphere; however, the ACE-FTS data gaps in the tropical troposphere make this hypothesis difficult to test.

3.4.1 Dependence on Tropopause Height

In the Northern Hemisphere, the measurement–model mismatch of the stratospheric contribution increases as the tropopause altitude shifts downward (Figure 3.6). As the model's stratospheric portion of the pressure-weighted total column increases, the error in stratospheric CH_4 is amplified, causing a larger disagreement with measurements. Because the tropopause height decreases with latitude, and this gradient increases during winter and spring, this introduces both zonal and seasonal biases. The disagreement exhibits a large spread for relatively few tropopause pressure heights because the model's effective tropopause, that is, the pressure level at which the model divides the troposphere from the stratosphere in GEOS-Chem, is defined at discrete grid level pressure boundaries.

The tropospheric mismatch ($\Delta X^t_{CH_4}$), by contrast, decreases with tropopause height for the majority of days and exhibits a much weaker correlation to tropopause height, 0.099 versus 0.22 for the stratospheric contribution. Thus, as expected, the tropopause height explains less of the variance in the measurement–model mismatch in $X^t_{CH_4}$: the upper troposphere is generally well-mixed, and chemical loss does not vary with altitude as much as in the lower stratosphere. This weaker relationship also demonstrates that the choice of tropopause used in the tropospheric profile integration does not strongly impact $\Delta X^t_{CH_4}$.

The relationship between $\Delta X^t_{CH_4}$ and tropopause height has a clear zonal component that indicates that the correlation is instead a result of another parameter that varies with latitude. The tropospheric slope is dominated by high-latitude sites; the sub-tropical sites exhibit a much weaker correlation. At Izaña, which is in the sub-tropics at an altitude of 2.4 km, the correlation between $\Delta X^t_{CH_4}$ and tropopause position is weak: the slope of -0.035 ± 0.03 is nearly flat within error, and R^2 is 0.025. By

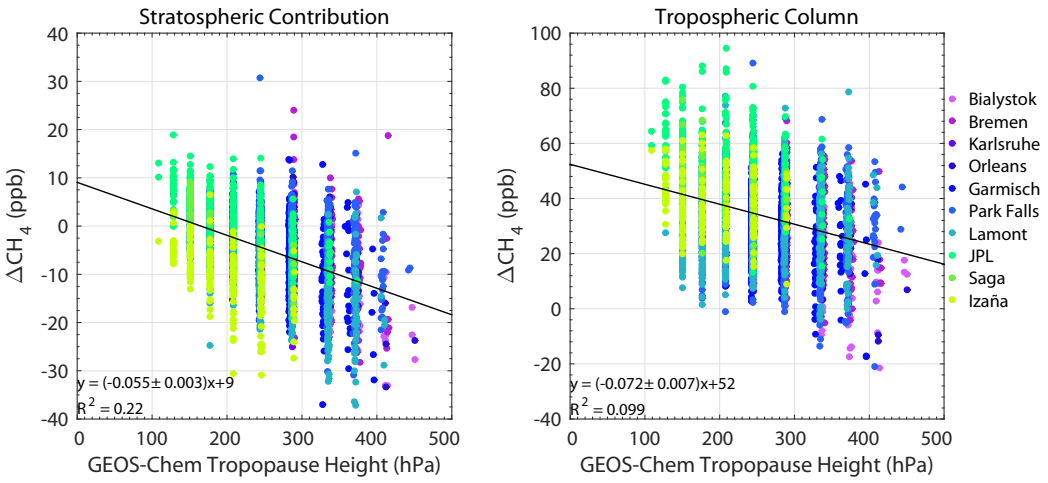

Figure 3.6: TCCON minus GEOS-Chem CH_4 column-averaged DMFs as a function of the effective GEOS-Chem tropopause height, shown for Northern Hemisphere sites. Site colors are as in Figure 3.1.

contrast, the stratospheric relationship at Izaña corresponds more closely with the other Northern Hemisphere sites: the slope is -0.088 ± 0.02, and $R^2 = 0.36$.

3.4.2 Seasonal Agreement

The tropospheric difference between TCCON and GEOS-Chem, $\Delta X^t_{CH_4}$, has a periodic trend indicating that the model error has a strong seasonal component in the troposphere. To isolate stable seasonal patterns from the cumulative influence of emissions, we calculate the detrended seasonal mean column-averaged DMFs for each site. In the Southern Hemisphere, the measurements and model agree well. Across the Northern Hemisphere sites, however, the seasonality differs (Figure 3.7). The seasonal amplitude of GEOS-Chem $X^t_{CH_4}$ is about equal to that of TCCON, but the TCCON $X^t_{CH_4}$ seasonal minimum is in June/July while the GEOS-Chem seasonal minimum is in September/October. Additionally, while TCCON $X^t_{CH_4}$ begins to decrease in January, GEOS-Chem shows some persistence into the spring.

The seasonal delay also appears in comparisons of GEOS-Chem surface CH_4 with National Oceanic and Atmospheric Administration (NOAA) surface flask measurements at the LEF site in Park Falls (Figure 3.8). The seasonality of GEOS-Chem's surface is regulated more by emissions than transport: CH_4 peaks in the summer, when wetland emissions are highest (Figure 3.10). This contrasts with the flask measurements, which reach a minimum in the summer (Figure 3.8). The seasonality covaries remarkably closely with respect to other features: the late winter decrease, spring persistence, and local minimum in October. The spring plateau lasts twice

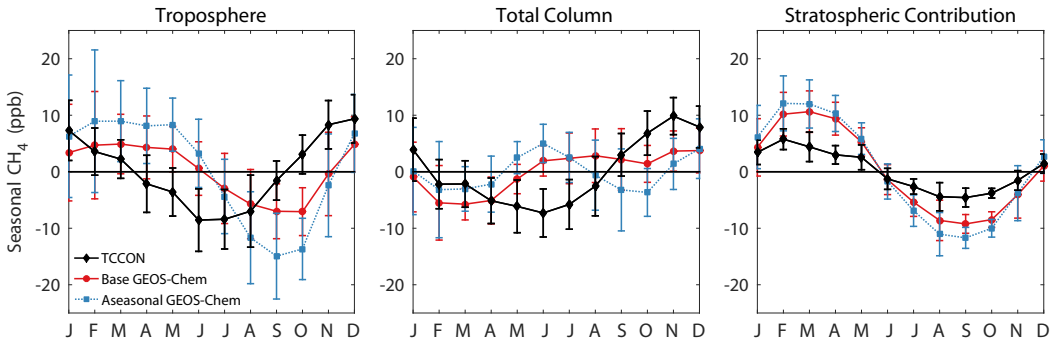

Figure 3.7: Detrended seasonality of TCCON (black diamonds), GEOS-Chem base (red circles), and GEOS-Chem aseasonal (blue squares) CH_4 column-averaged DMFs, averaged across Northern Hemisphere sites, excluding Saga, which has less than one year of measurements prior to 2012. Error bars denote the 1σ standard deviation across sites.

as long as seen in observations, however, and matches $X^t_{CH_4}$, indicating that feature is not the result of vertical transport between the PBL and free troposphere.

Not surprisingly, a time lag does not occur in the stratosphere; the TCCON stratospheric seasonal amplitude is less than half but in phase with that of GEOS-Chem (Figure 3.7). The vertical inconsistency of the seasonality produces unusual features in the model total column. From January through April, the TCCON and GEOS-Chem X_{CH_4} are consistent because the model's bias in the troposphere is balanced by the larger stratospheric contribution. Starting in May, however, the model diverges from the measurements as the higher tropopause limits the stratosphere's influence, and the phase lag in the troposphere dominates. This balancing effect is also demonstrated by the greater variance across sites in the model $X^t_{CH_4}$ and stratospheric contribution compared to measurements, but about the same variance in X_{CH_4}.

For the aseasonal simulation, the tropospheric seasonal cycle amplitude and variance across sites increase (Figure 3.7). The greatest model differences, from August through October, are a result of dampening the large wetland fluxes in the base simulation that balance higher OH concentrations. The seasonal amplitude does not increase as drastically in the sub-tropics, where the total emissions are not as impacted by seasonally varying sources, leading to the greater variance across sites. The second largest difference between simulation amplitudes occurs in the spring, and OH loss could potentially be contributing to the discrepancy in these months also. The aseasonal simulation spreads the wetland fluxes so as to introduce emissions in the winter and spring, when the OH concentrations are lowest. Another

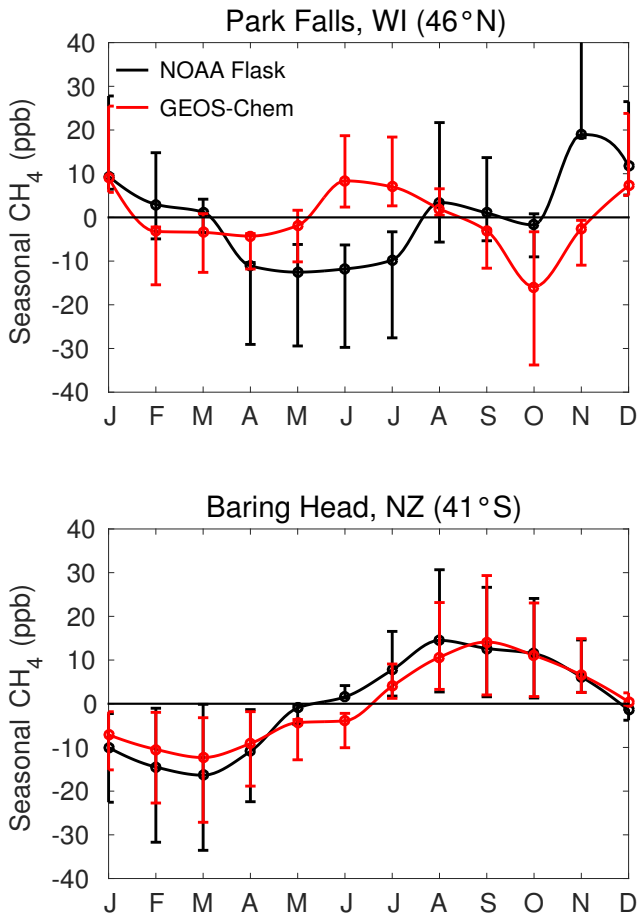

Figure 3.8: NOAA surface flask (black) and GEOS-Chem surface level (red) seasonality of CH_4 DMFs over 2005–2011 at Park Falls, WI, USA and Baring Head, NZ. Lower and upper bounds denote the 25th and 75th percentiles, respectively, of detrended data for each month.

possibility is that the model could be subject to errors that are in phase with the base simulation seasonal emissions, which would then have an ameliorating effect that produces the reasonable seasonal cycle amplitude. The stratospheric contribution does not change, however, further demonstrating that the stratosphere is insensitive to perturbations to Northern Hemisphere emissions.

The impact of a static stratosphere and changing troposphere is to make the seasonality of the aseasonal simulation X_{CH_4} bimodal: the October local minimum in the base simulation becomes a fall absolute minimum. The aseasonal X_{CH_4} agrees with TCCON in late winter, masking the greater disagreement in the troposphere. Notably, the main tropospheric features of the base simulation, the seasonal phase lag and spring persistence, are still apparent. Thus, the seasonality of emissions prescribed in the forward model is not the driver of the discrepancies between mea-

surement and model $X^t_{CH_4}$ seasonalities. OH is not likely the driver of these features, as the Northern Hemisphere phase shift also occurs in simulations performed with large changes in OH (Figure 3.13, in Appendix 3A). Transport is thus the most likely driver of these tropospheric trends in the model.

3.5 Discussion

The stratospheric insensitivity to changes in emissions and tropospheric loss has significant implications for flux inversions. Model inversions use the sensitivity of trace gas concentrations at a given location to perturbations of different emission sources to adjust those emissions so as to match observations at that location. The response of modeled CH_4 DMFs to changing emissions depends on the model's transport and chemical loss, as well as assumptions about the seasonal and spatial distribution of emissions relative to each other. Thus the model sensitivity kernel, the linear operator that maps emissions to CH_4 concentrations, implicitly includes uncertainties in these terms. The model's stratospheric response to emission perturbations differs from that of the troposphere and is subject to different transport and loss errors. Because the tropospheric transport errors covary with emissions, they alias into the resulting source attribution.

Comparing measurement and model stratospheric CH_4 as a fraction of the total column provides a normalized comparison that isolates differences in the vertical structure from those caused by initial conditions and unbalanced sources and sinks. Figure 3.9 illustrates the error associated with the normalized stratospheric column and the associated stratospheric contribution to X_{CH_4} at Park Falls. Although the stratosphere accounts for less than 30% of X_{CH_4}, a relatively small error can produce significant seasonal differences; the springtime error of 4.5×10^{17} molec cm^{-2} (23 ppb) is more than twice the seasonal cycle amplitude. Winter and spring are also when $X^t_{CH_4}$ is least sensitive to seasonal emissions; by contrast, the error is about 15 ppb in the summer, when seasonal emissions have the greatest influence (Figure 3.9, top panel). The seasonality of the stratospheric error will therefore distort the inversion mechanism and thus posterior emissions estimates.

Additional bias is introduced by differences in the seasonal patterns of $\Delta X^t_{CH_4}$ and ΔX_{CH_4}. Wetlands are the largest seasonal source of CH_4 in models and the largest natural source in flux inventories, and their emissions are very uncertain: estimates range between 142 and 284 TgC year^{-1} for the 2000–2009 time period (Kirschke et al. 2013). A priori GEOS-Chem CH_4 emissions from northern high-

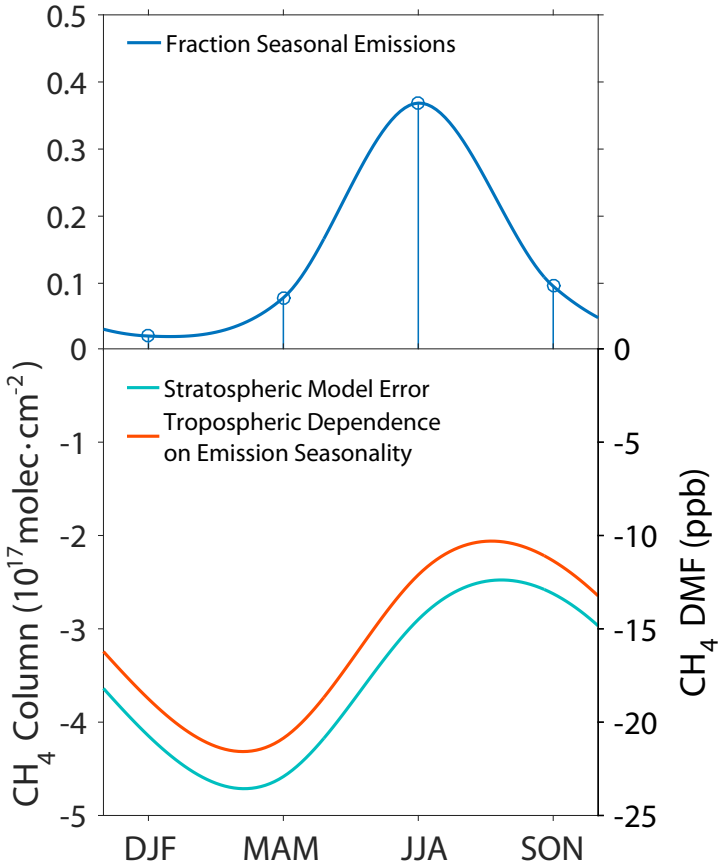

Figure 3.9: Top: Seasonally averaged fraction of model emissions from seasonally varying sources, north of 40°N. Bottom: Seasonally averaged normalized model stratospheric column error (teal) and the difference between base and aseasonal simulation tropospheric columns (orange) at Park Falls.

latitude wetlands are extremely variable, with large fluxes in June, July, and August; moderate fluxes in May and September; and almost no fluxes the remainder of the year (Figure 3.10a). Surface CH_4 concentrations in models depend on the assumed seasonally varying emissions. Patra et al. (2011) found that correlations between the seasonal cycles of the forward model averages and in situ observations of CH_4 DMFs at the surface varied for a given site by up to 0.78 ± 0.4 depending on wetland and biomass burning fields used. Model inversions that scale emissions in a given grid box based on the incorrect seasonality will invariably change the posterior attribution of seasonal emissions. Fraser et al. (2013) found that optimized wetland emissions from inversions that assimilate surface data only are smaller than the priors, while those from inversions that assimilate GOSAT total columns are larger, even if surface measurements are also assimilated. From this we infer that the transport errors in the model's free troposphere lead to an "optimization" of the

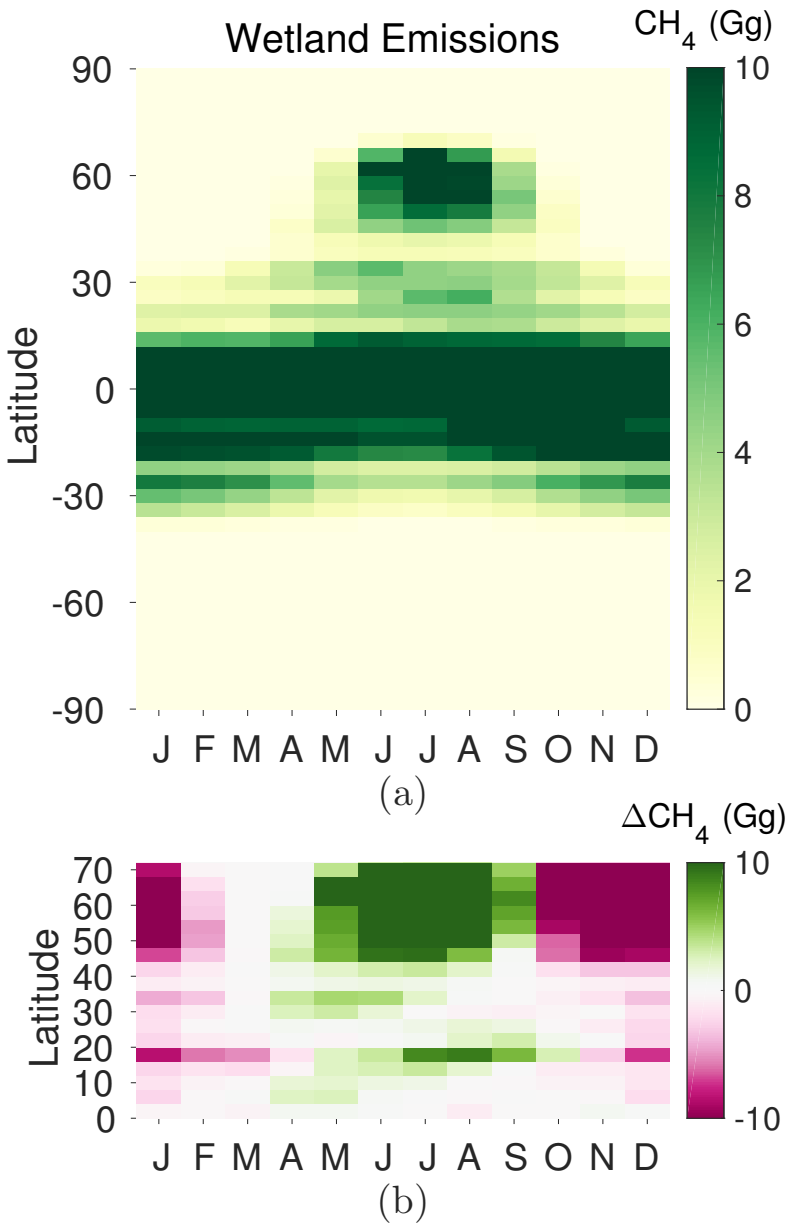

Figure 3.10: **(a)** GEOS-Chem monthly zonal mean wetland emissions, in Gg. **(b)** The Northern Hemisphere sensitivity of GEOS-Chem wetland emission attribution caused by a 3-month lag for each 1 ppb increase of CH_4 in the tropospheric column, in Gg.

prior fluxes of opposite sign to that of the emission errors that the inversion attempts to correct.

A two- to three-month shift in the phase of the $X^t_{CH_4}$ seasonality will produce a strong under- or over-estimation of posterior wetland fluxes in late spring through early fall. In an inversion, prior emissions are adjusted in proportion to the deviation

of the model's CH_4 DMFs from observed values. Attribution of these posterior emissions to different sectors depends on a priori information and assumptions about how they vary in time and location relative to one another. Thus, an increase in posterior emissions relative to the prior in the northern mid- and high latitudes during winter will not change emissions from wetlands. For example, Figure 3.10b illustrates the sensitivity of posterior wetland emissions to a three-month lag in the Northern Hemisphere. The change in posterior emissions is derived by calculating the total emissions required to produce an increase of 1 ppb of CH_4 in each tropospheric column and scaling those emissions according to the a priori contribution of wetlands, estimated as the fractional contribution of wetlands to the total monthly mean emissions. The difference between this change in wetland emissions and the value in the same location three months prior produces the sensitivity of wetland emissions to the tropospheric phase lag. This approach provides an alternative to the computationally expensive calculation of the gain matrix over the entire time series but does not include information about model transport.

The tropics and subtropics are less sensitive to a phase shift, but polewards of 40°N, both the magnitude and seasonality of the difference are significant. Large differences between measured and modeled $X^t_{CH_4}$ are concurrent with low emissions from seasonal sources. The adjustments to prior emissions produced by larger measurement–model disagreement that occur when seasonal sources are a small fraction of total emissions will overestimate posterior emissions from aseasonal sources. Thus these seasonal errors will bias source apportionment toward emissions that do not vary on timescales shorter than annually.

3.6 Conclusions

Assimilation of total column measurements into CTMs can improve constraints on the global CH_4 budget; however, the model's treatment of stratospheric chemistry and dynamics must be carefully considered. This work has compared TCCON and GEOS-Chem pressure-weighted total and tropospheric column-averaged CH_4 DMFs, X_{CH_4}, and $X^t_{CH_4}$ respectively, parsing out the seasonality of the troposphere and stratosphere and the resulting impacts on X_{CH_4} (Figure 3.9a). The Southern Hemisphere measurement–model agreement is robust to changes in emissions or tropospheric OH. In the Northern Hemisphere the model's stratospheric contribution is larger than that of the measurements, and the mismatch increases as the tropopause altitude decreases. The result is greater model error at high-latitude sites, with the magnitude of this error varying seasonally. Moreover, in the Northern Hemisphere

the GEOS-Chem $X^t_{CH_4}$ exhibits a 2–3 month phase lag. The combined tropospheric and stratospheric errors smooth the model X_{CH_4} such that they may agree with total column measurements despite having an incorrect vertical distribution.

Model transport errors coupled with spatial and seasonal measurement sparsity can limit the accuracy of the location and timing of emissions scaling. The differences in the seasonality mismatch across vertical levels amplify the error uncertainty because the timing of optimized fluxes will be especially susceptible to limitations in model transport. The stronger influence of the stratosphere at higher latitudes due to lower tropopause heights, together with the higher temporal variability of the stratospheric fraction of the total column due to the stronger seasonal cycle of the tropopause, also impacts the seasonality of the meridional gradient of X_{CH_4}.

The influence of stratospheric variability on emissions is not unique to the model chosen for this analysis. Bergamaschi et al. (2013) ran TM5-4DVAR inversions using SCIAMACHY column and NOAA surface measurements and found that the mean biases between the optimized CH_4 profiles and aircraft measurements differ between the PBL, free troposphere, and UTLS. Seasonal emissions from wetlands and biomass burning vary by ±10 and ±7 $TgCH_4$, respectively, from year to year, and the zonal partitioning of posterior emissions is sensitive to the wetland priors chosen. Moreover, the larger changes to emissions and sensitivity to assumptions in the Northern Hemisphere indicate that TM5 is also subject to the strong hemispheric differences found in GEOS-Chem. The TransCom-CH_4 model comparison found that the interhemispheric exchange time in GEOS-Chem was near the model median over the 1996–2007 time series (Patra et al. 2011), which suggests that GEOS-Chem's interhemispheric transport, and thus associated errors, is not particularly distinct. Ostler et al. (2016) found that atmospheric CTM (ACTM) and other CTMs used in TransCom-CH_4 are subject to transport errors that impact emissions optimization. Furthermore, ACTM profiles show a similar over-estimation of stratospheric CH_4, zonally varying measurement–model mismatch dependent on tropopause height.

In this analysis we have used TCCON $X^t_{CH_4}$ derived with the HF-proxy method; however, $X^t_{CH_4}$ calculated using other stratospheric tracers such as nitrous oxide (N_2O) (Wang et al. 2014) would provide an additional constraint on models' representations of the stratosphere, as N_2O is not subject to the spectral interference with water vapor that impacts HF. Information about the vertical tropospheric CH_4 profile directly retrieved from NDACC spectra (Sepúlveda et al. 2014) can also be

used to assess whether transport errors differ at different levels of the free troposphere. Ideally, information from these tropospheric products could be integrated to overcome the limitations of each: the sensitivity of $X^t_{CH_4}$ to prior assumptions of STE and the sensitivity of profile retrievals to UTLS variability (Ostler et al. 2014).

A limitation of the aseasonal simulation was that the distribution of emissions was not identical to that of the base simulation due to the scaling approach we employed. Ideally, the aseasonal emissions for each sector would have been fluxes calculated for each grid box from the base simulation annual emissions. The robustness of the model's tropospheric phase shift, which was apparent regardless of the emissions used, demonstrates that this feature is not a product of the chosen emissions fields. However, more nuanced analysis on smaller spatial scales would benefit from simulations that prescribe the annual mean for each of the seasonal sources. The most recent version of GEOS-Chem has a much more flexible emissions scheme (Keller et al. 2014) that allows these more nuanced experiments to be performed and analyzed.

The insensitivity of model stratospheres to tropospheric change allows for a straightforward solution: prescribed stratospheric CH_4 fields based on satellite observations from ACE-FTS, MIPAS (Clarmann et al. 2009), or a compilation of remote sensing instruments (Buchwitz et al. 2015). As the representation of tropical convection and exchange across the UTLS advances in models and reduces stratospheric isolation, chemical loss and transport mechanisms would need to be improved. The output from more accurate stratospheric models over the time period of interest could be used to set the stratospheric component in the offline CH_4 simulation. For instance, the Universal tropospheric–stratospheric Chemistry eXtension (UCX) mechanism, which has been added to more recent versions of GEOS-Chem, updates the stratospheric component of the standard full chemistry simulation such that CH_4 has more sophisticated upwelling, advection, and chemical reaction schemes (Eastham et al. 2014). Models that account for interannual variability in both stratospheric and tropospheric dynamics can then assimilate total column measurements to develop more accurate global CH_4 budgets.

Appendix 3A: Equilibrium sensitivity experiments

All equilibrium runs for a given simulation have identical meteorology, emissions, and OH fields over June 2004–May 2005. Initial conditions for each year are set by the restart files of the previous run. To calculate columns at each site, GEOS-Chem

monthly mean mole fractions are adjusted for the monthly medians of the site's daily mean surface pressures and smoothed with the monthly median scaled prior profiles and averaging kernels, interpolated using the monthly medians of the daily mean solar zenith angles. Because Park Falls and Lauder are the only TCCON sites that had started taking measurements over this time period, they are the only sites used to generate smoothed columns for the comparisons to the experimental simulations.

Emissions in the aseasonal simulation were derived by running a two-dimensional regression on the annual emissions to determine the scale factors that would produce the smallest residual of total emissions and the interhemispheric gradient. Figure 3.11 illustrates the difference in total emissions between the base and aseasonal simulations for each zonal band.

The updated OH simulation used OH output from a 2012 GEOS-Chem standard chemistry simulation with extensive updates to the photochemical oxidation mechanisms of biogenic volatile organic compounds (VOCs), described in Bates et al. (2016) and references therein. These were converted to 3-D monthly mean OH concentrations to conform to the infrastructure of the GEOS-Chem offline CH_4 tropospheric loss mechanism. The OH was then scaled by 90% to keep the lifetime above 8 years, and emissions were scaled by 112% to maintain the same balance between sources and sinks in the base simulation. Figure 3.12 provides zonal averages of the difference between the base and updated OH columns.

The full list of simulations run is provided in Table 3.3, with descriptions and the CH_4 emissions, tropospheric OH, and total chemical loss lifetimes. Figure 3.13 shows each simulation's seasonality of $X^t_{CH_4}$ at Park Falls, with TCCON seasonality plotted for reference, as well as the seasonality of the difference between the base and each simulation.

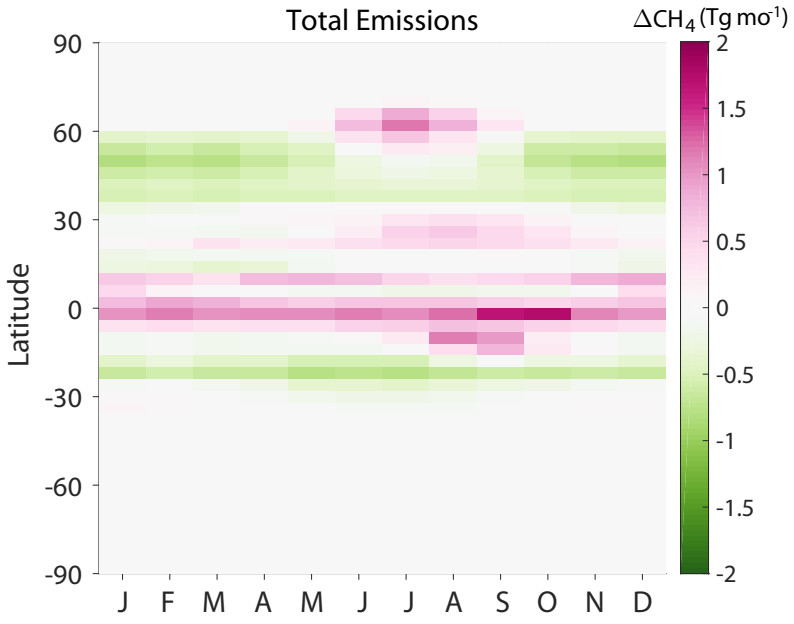

Figure 3.11: Monthly averages of the difference in total CH_4 emissions between the base and aseasonal GEOS-Chem simulations, summed over each zonal band, in Tg mo^{-1}.

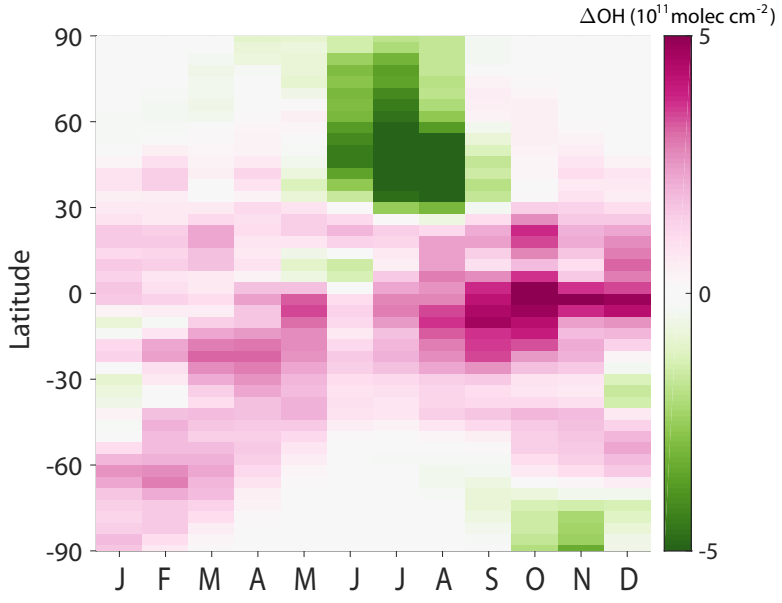

Figure 3.12: Zonal averages of the difference in total column OH (molec cm^{-2}) between the base and updated monthly OH fields.

Table 3.3: List of sensitivity experiments.

Simulation name	Description	CH_4 lifetime (years) with respect to			Final CH_4 burden (Tg)
		Emissions	Tropospheric OH	Total loss	
Base	Default OH and emissions	9.6	10.7	9.7	4825
Aseasonal	Constant monthly emission rates	9.6	10.7	9.7	4872
Updated OH	Monthly OH fields from standard chemistry + biogenic VOCs, scaled down by 10%	8.5	9.4	8.6	4828
Unscaled updated OH	Monthly OH fields from standard chemistry + biogenic VOCs	7.7	8.4	7.8	4917
90% OH	Default OH scaled down by 10%	10.5	11.9	10.7	5296
110% OH	Default OH scaled up by 10%	8.8	9.7	8.8	4425
Scaled rice emissions	Rice emissions increased by 20%	9.6	10.7	9.6	4780
No wetlands	Wetland emissions turned off	10.7	10.6	9.5	3768
Scaled livestock Emissions	Scale livestock emissions by 50%	9.6	10.7	9.6	4359
MERRA	MERRA meteorology fields	9.6	10.7	9.6	4849
Tropopause level	Set top of troposphere 2 vertical levels higher	9.6	10.6	9.6	4855

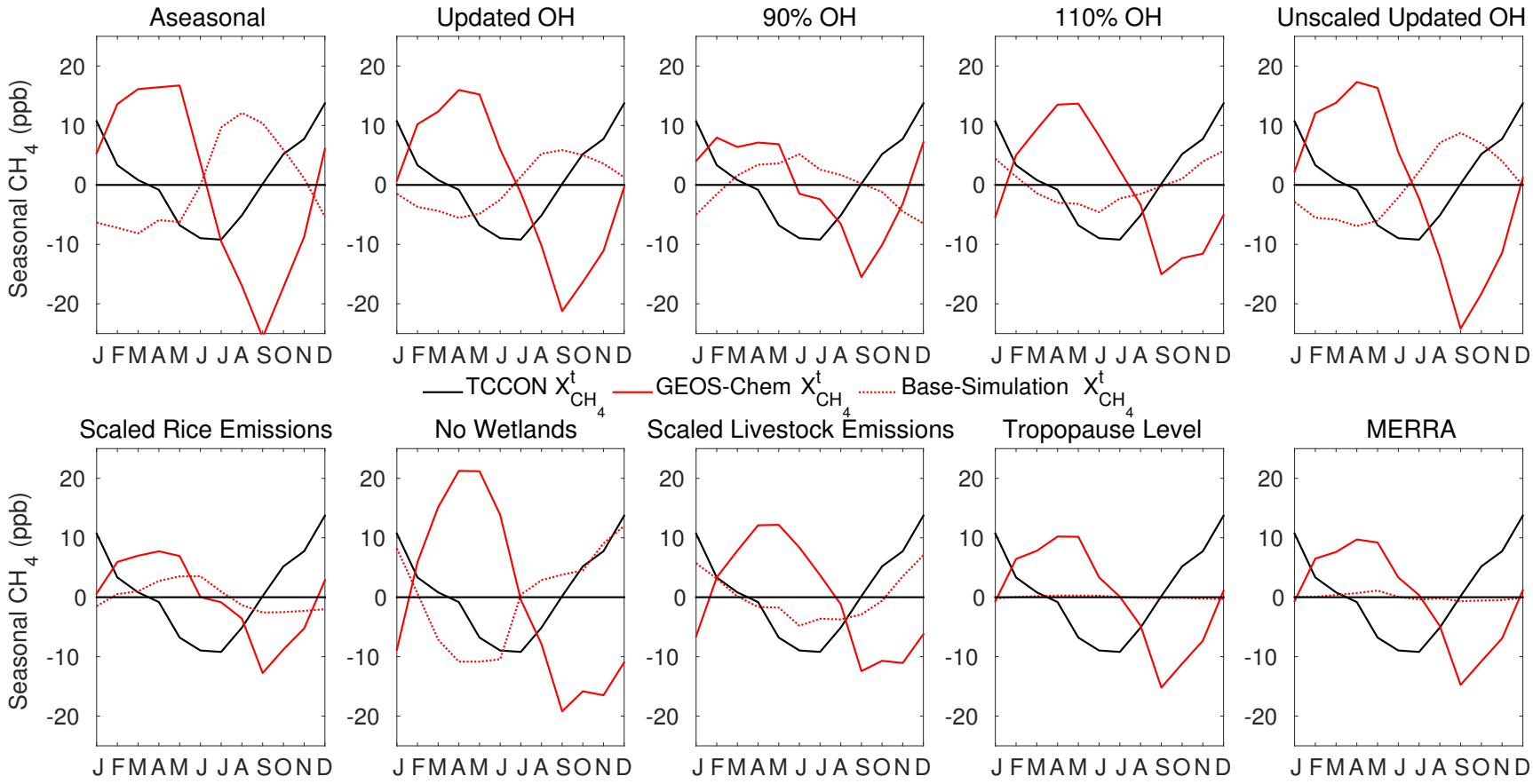

Figure 3.13: Seasonality of tropospheric CH_4 ($X^t_{CH_4}$) at Park Falls for TCCON (black solid line), GEOS-Chem (red solid line), and the difference from the base simulation (dotted red line) for each of the sensitivity experiments, in ppb.

Appendix 3B: Model smoothing for measurement comparisons

Base and aseasonal daily runs were initialized using CH_4 fields from their respective 34th equilibrium cycles. Daily CH_4 mole fractions averaged over both 24 h and 10:00–14:00 local time were output to test whether TCCON's daytime-only observations would introduce a bias in the comparisons. Measurement–model differences were not sensitive to averaging times. Comparison of measurements to model columns produced using the 24 h and 10:00–14:00 LT averages produce equivalent slopes and only slightly different intercepts and correlation coefficients. The seasonality of 10:00–14:00 LT column-averaged DMFs does not differ, except for the fall seasonal maximum of the adjusted troposphere and stratospheric contribution at Park Falls in October, one month later than the 24 h column-averaged DMF seasonality.

CH_4 dry vertical profiles for each grid box associated with a TCCON site, $\vec{x}^{m}_{CH_4}$, were smoothed with corresponding FTS column averaging kernels, $\vec{a}_{CH_4}$, and scaled priors for each day and vertically integrated using pressure-weighted levels:

$$X^{s}_{CH_4} = \gamma_{CH_4} \cdot X^{a}_{CH_4} + \vec{a}^{\S}_{CH_4} \left(\vec{x}^{m}_{CH_4} - \gamma_{CH_4} \vec{x}^{a}_{CH_4} \right) \tag{3.2}$$

where $X^{s}_{CH_4}$ is the smoothed GEOS-Chem column-averaged DMF, γ_{CH_4} is the TCCON daily median retrieved profile scaling factor, and $\vec{x}^{a}_{CH_4}$ and $X^{a}_{CH_4}$ are respectively the a priori profile and column-integrated CH_4 DMFs (Rodgers and Connor 2003).

The pressure weighting function, $\vec{h}$, was applied such that $X = \vec{h}^{T}\vec{x}$. TCCON priors were interpolated to the GEOS-Chem pressure grid, and GEOS-Chem pressure and corresponding gas profiles were adjusted using daily mean surface pressures local to each site (Wunch et al. 2010; Messerschmidt et al. 2011). The averaging kernels were interpolated for the local daily mean solar zenith angle and the GEOS-Chem pressure grid so that it could be applied to the difference between the GEOS-Chem and TCCON profiles as $\vec{a}^{\S}\vec{x} = \sum_{i=1}^{N} a_i h_i x_i$ from the surface to the highest level, N, at i pressure levels (Connor et al. 2008; Wunch et al. 2011b). Figure 3.14 shows how the smoothed column compares to the column that only uses the dry gas correction.

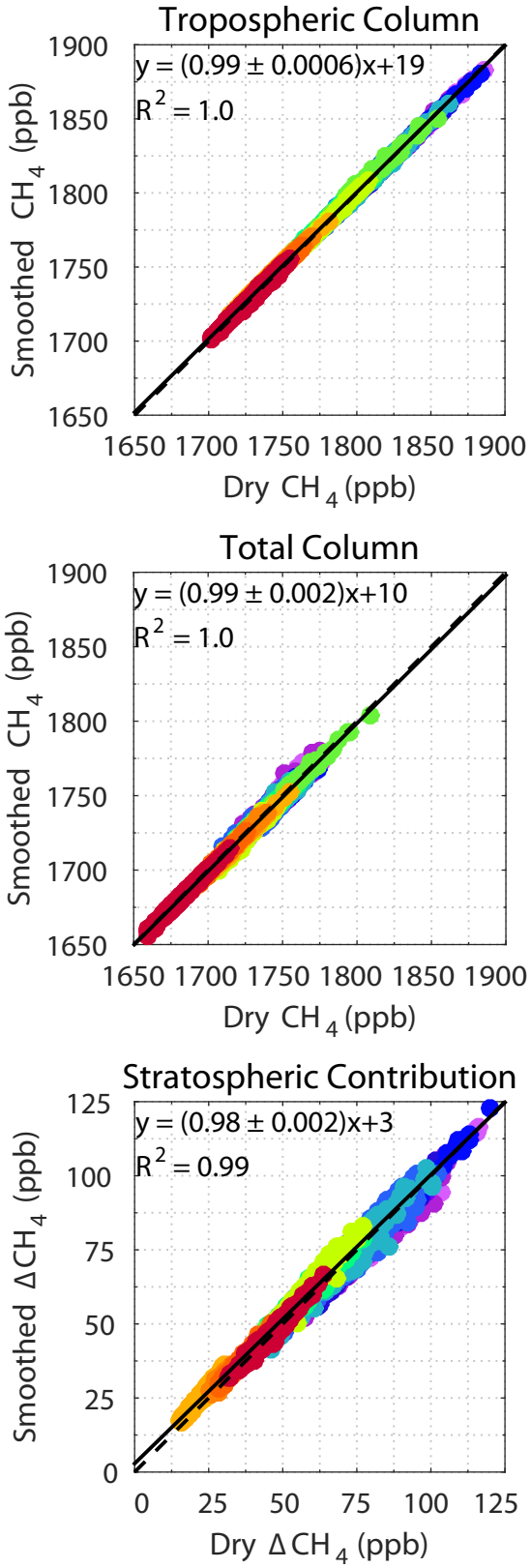

Figure 3.14: GEOS-Chem smoothed vs. dry integrated CH_4 DMFs for base simulation tropospheric columns, total columns, and stratospheric contribution. Site colors are as in Figure 3.1. Dashed lines mark the one-to-one lines.

Appendix 3C: Derivation of Stratospheric Contribution

Considering the CH_4 profile integration as in Equation (2.10), and substituting the profile of CH_4 in the stratosphere, $x_{CH_4}(P) = x_{CH_4}(P^t) + \delta \cdot P$, described in Section 2.4, the total column is calculated as

$$\int_0^{P^s} x_{CH_4} \frac{dP}{gm} = \int_{P^t}^{P^s} x_{CH_4} \frac{dP}{gm} + \int_0^{P^t} \left[x_{CH_4}\left(P^t\right) + \delta \cdot P \right] \frac{dP}{gm} \tag{3.3}$$

$$X_{CH_4} \cdot P^s = X^t_{CH_4} \left[P^s - P^t \right] + x_{CH_4}\left(P^t\right) \cdot P^t + c^{\delta}_{CH_4} \tag{3.4}$$

where $c^{\delta}_{CH_4}$ is the pressure-weighted column average of CH_4 loss in the stratosphere. Rearranging terms, Equation (3.4) becomes:

$$\left[X_{CH_4} - X^t_{CH_4} \right] P^s = \left[x_{CH_4}\left(P^t\right) - X^t_{CH_4} \right] P^t + c^{\delta}_{CH_4} \tag{3.5}$$

$$X^t_{CH_4} - X_{CH_4} = \left[X^t_{CH_4} - x_{CH_4}\left(P^t\right) \right] \frac{P^t}{P^s} - \frac{c^{\delta}_{CH_4}}{P^s} \tag{3.6}$$

such that the difference between the tropospheric and total column-averaged DMFs is a function of the two terms governing the stratospheric contribution to the total column: the gradient across the tropopause, $x_{CH_4}(P^t) - X^t_{CH_4}$, and stratospheric CH_4 loss, $c^{\delta}_{CH_4}$. The stratospheric contribution is thus a proxy for the impact of stratospheric variability on the total column of CH_4: given a constant tropospheric column, as the stratospheric contribution becomes larger the total column-averaged DMF becomes smaller.

acknowledgments This work was supported by NASA Headquarters under the NASA Earth and Space Science Fellowship Program grant NNX14AL30H and NASA's Carbon Cycle Science program. Park Falls, Lamont, and JPL are funded by NASA grants NNX14AI60G, NNX11AG01G, NAG5-12247, NNG05-GD07G, and NASA Orbiting Carbon Observatory Program; we are grateful to the DOE ARM program and Jeff Ayers for their technical support in Lamont and Park Falls, respectively. Darwin and Wollongong are funded by NASA grants NAG5-12247 and NNG05-GD07G and the Australian Research Council grants DP140101552, DP110103118, DP0879468, and LP0562346, and Nicholas Deutscher is supported by an Australian Research Council Fellowship, DE140100178; we are grateful to the DOE ARM program for technical support in Darwin. Bremen, Bialystok, and Orleans are funded by the EU projects InGOS and ICOS-INWIRE and by the Senate of Bremen. Réunion Island is funded by the EU FP7 project ICOS-INWIRE, the national Belgian support to ICOS and the AGACC-II project (Science for Sustainable Development Program), the Université de la Réunion, and the French regional and national organizations (INSU, CNRS). From 2004 to 2011 the Lauder TCCON program was funded by the New Zealand Foundation of Research Science and Technology contracts CO1X0204, CO1X0703, and CO1X0406. We thank Shuji Kawakami for his technical support in Saga. We thank Peter Bernath, Kaley Walker, and Chris Boone for their guidance using the ACE-FTS data, which were obtained through the Atmospheric Chemistry Experiment (ACE) mission, primarily funded by the Canadian Space Agency. We are grateful to Geoff Toon for his continuous efforts developing the GGG software, for providing the MkIV data, and his input on the manuscript. We thank Arlyn Andrews for providing the LEF surface flask data, which were generated by NOAA-ESRL, Carbon Cycle Greenhouse Gases Group. Baring Head NIWA surface data were provided courtesy of Gordon Brailsford, Dave Lowe, and Ross Martin. We also acknowledge the contributions of in situ vertical profiles from the AirCore, HIPPO, IMECC, INTEX, Learjet, and START08 campaigns. We are grateful to Kelvin Bates for providing monthly OH fields for the GEOS-Chem Updated OH sensitivity experiments. Lastly, we thank the three anonymous reviewers who provided feedback and suggestions.

Chapter 4

A REVERSAL IN NORTHERN HEMISPHERE MERIDIONAL GRADIENTS OF TROPOSPHERIC METHANE ASSOCIATED WITH THE CHANGE IN GLOBAL GROWTH RATE

4.1 Zonal Variability of Methane Growth in the Last Decade

The complexity of the global methane (CH_4) cycle makes diagnosing the mechanisms responsible for the recent increase in tropospheric concentrations poorly constrained, with data on various spatial and time scales providing too sparse of a picture for consensus. Since the "renewed growth" of CH_4 in the past decade (Nisbet et al. 2014, Fig. 4.1), almost as many explanations as CH_4 sources have emerged using several different measurement platforms (c.f., Bergamaschi et al. 2007; Dlugokencky et al. 2011; Turner et al. 2015), assumptions about tropospheric oxidation (c.f., Rigby et al. 2008; Rigby et al. 2017; Turner et al. 2017) and models of trace gas transport (c.f., Bergamaschi et al. 2013; Kirschke et al. 2013; Pison et al. 2013). These investigations have aggregated comprehensive datasets and applied sophisticated statistical techniques to attempt to capture the complexity of the global system. In representing that complexity, they have necessarily relied on an variety of often unconstrained assumptions. However, the crux of the puzzle of what has been driving atmospheric CH_4 trends can be synthesized in a basic, though still challenging, question: where has the atmospheric burden of CH_4 been increasing?

In situ data from the National Oceanic and Atmospheric Administration (NOAA) Earth System Research Laboratory (ESRL) Global Monitoring Division illustrate how the temporal variability of CH_4 growth rates has differed zonally since 2000 (Fig. 4.2). The implications of such a plot are that no latitude has demonstrated consistent growth or decline in CH_4 and that local fluxes experience considerable reversal on one- to two-year timescales. Furthermore, the substantial increase in 2014 seems to have originated in the Northern sub-tropics and dispersed to both poles within several months. While these measurements provide an important long-term record of surface concentrations, their sensitivity to boundary-layer dynamics and local fluxes can create an incomplete and somewhat confusing global picture when aggregated. Column measurements, which are sensitive to the free troposphere as well as the surface, are less susceptible to fluctuations due to vertical transport

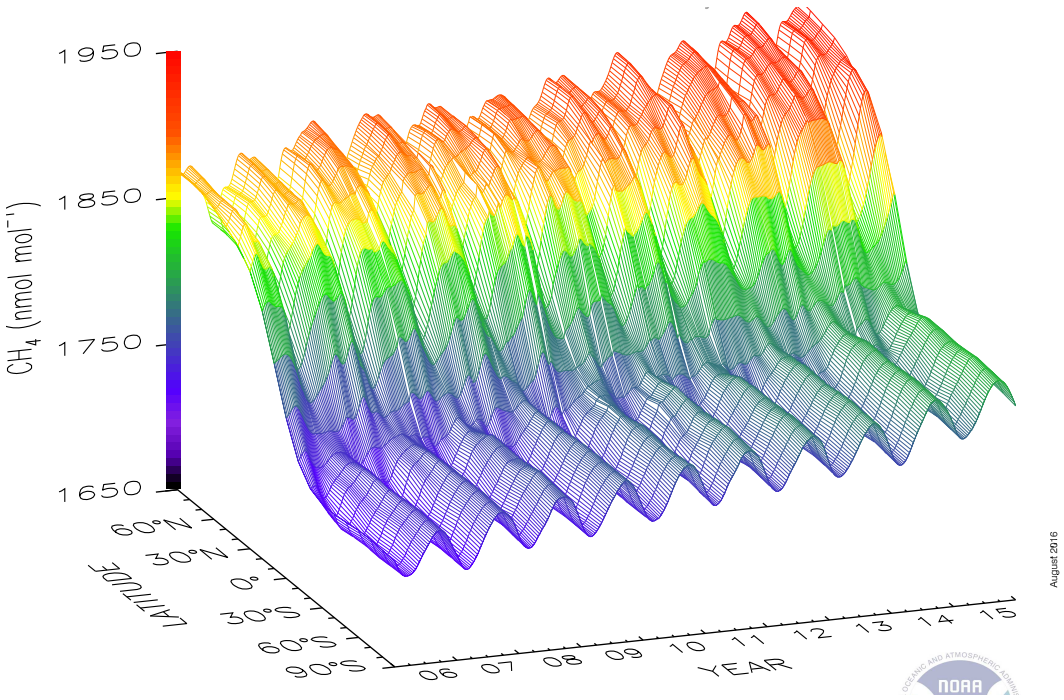

Figure 4.1: Zonal time series of CH_4 mole fractions (ppb) from 2006 through 2015, derived from in situ measurements in the marine boundary layer. (Image courtesy of NOAA ESRL Carbon Cycle/E. Dlugokencky, https://www.esrl.noaa.gov/gmd/ccgg/.)

and thus offer a potential contribution to disentangling mesoscale from regional variability (Yang et al. 2007). Total Carbon Column Observing Network (TCCON) pressure-weighted total column-averaged dry-air mole fractions (X_{gas}), for example, have improved the characterization of large-scale carbon dioxide (CO_2) gradients (Yang et al. 2007; Keppel-Aleks et al. 2011; Wunch et al. 2011b; Keppel-Aleks et al. 2012).

Meridional gradients of CH_4 columns may similarly contribute effective observational constraints on CH_4 fluxes. Figure 4.3 shows the time series of TCCON tropospheric partial columns of CH_4 ($X^t_{CH_4}$) at two mid-latitude sites within the continental United States: Lamont, Oklahoma (36°N) and Park Falls, Wisconsin (45°N). While $X^t_{CH_4}$ has increased at both locations, the seasonal cycles of the two time series exhibit different behavior at the beginning and end of the time series. In the two years between the summers of 2008 and 2010, $X^t_{CH_4}$ at Lamont and Park Falls coincide in the fall and winter, both in terms of concentration and variance (Fig. 4.3b). During the summer, however, the maximum at Lamont is about equal to the minimum at Park Falls, and the range is nearly 40 ppb, double that of Park

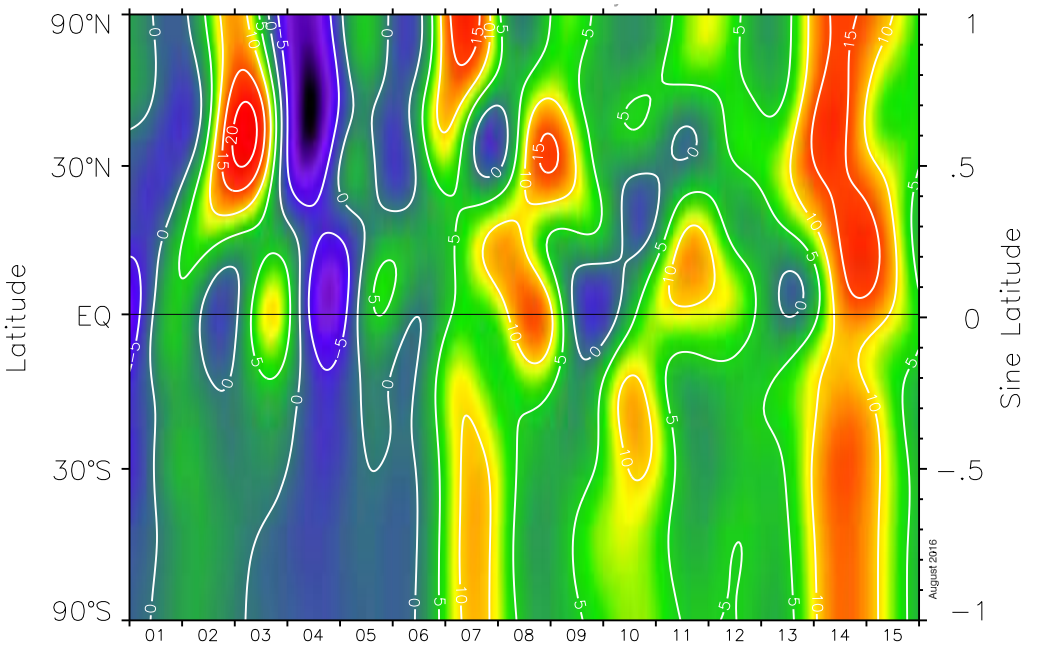

Figure 4.2: Zonal fluctuations of CH_4 growth rates (ppb yr^{-1}) from 2001 through 2015, derived from in situ surface measurements. Warmer colors correspond to anomalously high growth, and cooler colors correspond to anomalously low growth. (Image courtesy of NOAA ESRL Carbon Cycle/E. Dlugokencky, https://www.esrl.noaa.gov/gmd/ccgg/.)

Falls. By contrast, $X^t_{CH_4}$ values at these sites converge throughout 2013-2015, and the June-August range at Park Falls increases to about 30 ppb.

The seasonality of CH_4 at the surface reflects the balance of sinks and sources: tropospheric loss is greater in the summer when OH concentrations are higher, coincident with the peak in seasonally-varying emissions. The seasonality of trace gas columns is also governed by the variability of large-scale advection in the free troposphere, with relatively rapid mixing reducing meridional gradients in the winter (Keppel-Aleks et al. 2011). Keppel-Aleks et al. (2012) observed a similar relationship in X_{CO_2} at these two sites between July 2008 and February 2010 (Fig. 7 therein), which they attribute to seasonal differences in the balance between terrestrial fluxes and transport. Given that CH_4 also has a relatively long chemical lifetime compared to timescales of synoptic activity, we expect that the observed CH_4 gradient between these sites to be similarly modified by large-scale dynamics.

As with $X^t_{CH_4}$, the peak of the atmospheric sink of X_{CO_2}, boreal drawdown from vegetative growth, occurs in the summer. During these months, the sink depresses X_{CO_2} values at Park Falls, and the gradients of surface fluxes, coupled with the

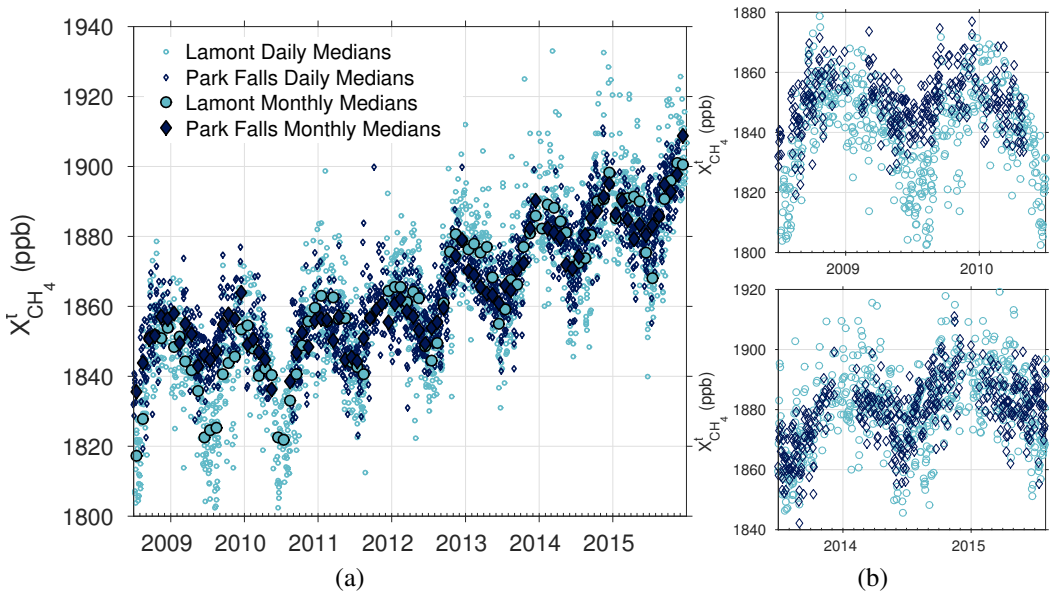

Figure 4.3: a) Daily (open) and monthly (filled) median TCCON $X^t_{\mathrm{CH_4}}$ at Park Falls and Lamont from July 2008 to January 2016. b) Enlargement of (a) over July 2008-July 2010 (top) and July 2013-July 2015 (bottom) with monthly medians excluded.

comparitively stagnant dynamical state of the atmosphere, causes the time series of the two sites to diverge (Figure 4.12). Furthermore, the range of values and the temporal variability increase, which Keppel-Aleks et al. (2012) attribute to the intermittent meridional transport of CO_2 between sites. Unlike $X_{\mathrm{CO_2}}$, $X^t_{\mathrm{CH_4}}$ only exhibits this larger variance at the site with the stronger sink. If we assume that the argument of Keppel-Aleks et al. (2012) applies to CH_4, the poleward advection of lower CH_4 concentrations would be balanced by some other process, such as local emissions, at Park Falls. Alternatively, stratospheric variability could drive the expanded range in $X_{\mathrm{CO_2}}$; however, the similarity in the summertime variance between $X_{\mathrm{CH_4}}$ and $X^t_{\mathrm{CH_4}}$ reduces that likelihood (Fig. 4.11). Rather, the gradients of $X^t_{\mathrm{CH_4}}$ seem to be sustained by the balance between sources and sinks.

As Keppel-Aleks et al. (2011) illustrate, the surface origins of air parcels, and the long-lived trace gases they transport, are difficult to discern solely from the meridional gradient defined using latitude. They instead relate the spatial distribution of $X_{\mathrm{CO_2}}$ to potential temperature (θ) in the free troposphere, effectively demonstrating that gradients in this tracer space relate more closely to the zonal origin of fluxes. We similarly evaluate the meridional gradients of $X^t_{\mathrm{CH_4}}$ using θ at 700 hPa (θ_{700}) as a dynamical tracer of synoptic-scale transport. We demonstrate that $X^t_{\mathrm{CH_4}}$ variability

in θ_{700} tracer space captures a component of the influence of advection on horizontal CH_4 gradients and, thus, better represents the geospatial distribution of fluxes than geographical location (Figure 4.4).

4.2 Tropospheric Columns Suggest the Recent Methane Increase has its Origin in the Northern Hemisphere Subtropics

4.2.1 Data Sources and Methods

TCCON $X^t_{CH_4}$ values are derived by removing the stratospheric contribution to the total column using the relationship between CH_4 and hydrogen fluoride (HF) in the stratosphere. This relationship is calculated using trace gas profiles from ACE-FTS satellite retrievals, as in Saad et al. (2014) and Saad et al. (2016), with revised zonal annual stratospheric CH_4-HF ratios calculated from ACE-FTS measurements as described in Section 2.5. TCCON sites used in this analysis are listed in Table 4.2. Potential temperature is calculated using National Centers for Environmental Protection and National Center for Atmospheric Research (NCEP/NCAR) 4x daily reanalysis temperature and pressure profiles (Kalnay et al. 1996), applying a tri-linear interpolation for site latitudes and longitudes over 6-hour mean intervals. TCCON $X^t_{CH_4}$ are averaged over each corresponding time interval for which a minimum of 10 measurements with errors less than 10% exist.

To isolate relevant modes of variability, we perform a time decomposition on the data. First, θ_{700} and $X^t_{CH_4}$ are smoothed with a 3-21 day fourth order zero-phase digital Butterworth bandpass filter to ensure signals represent synoptic-scale variability, following Keppel-Aleks et al. (2011) and Keppel-Aleks et al. (2012). $X^t_{CH_4}$ values are then detrended by subtracting the background long-term trend, determined from NOAA surface in situ measurements at Mauna Loa (Dlugokencky et al. 2016), shown in Figure 4.11. We estimate this trend by applying a 5 season (15 month) second order zero-phase digital Butterworth lowpass filter to daily mean values. We find that this type of filter removes seasonal information in the time series more effectively than a 13-month running average, thereby limiting the addition of seasonal bias to our analysis by the time decomposition. This analysis incorporates the daily-varying background trend to detrend $X^t_{CH_4}$; however, using an annual average changes the reported slopes by less than 0.4 ppb K^{-1}.

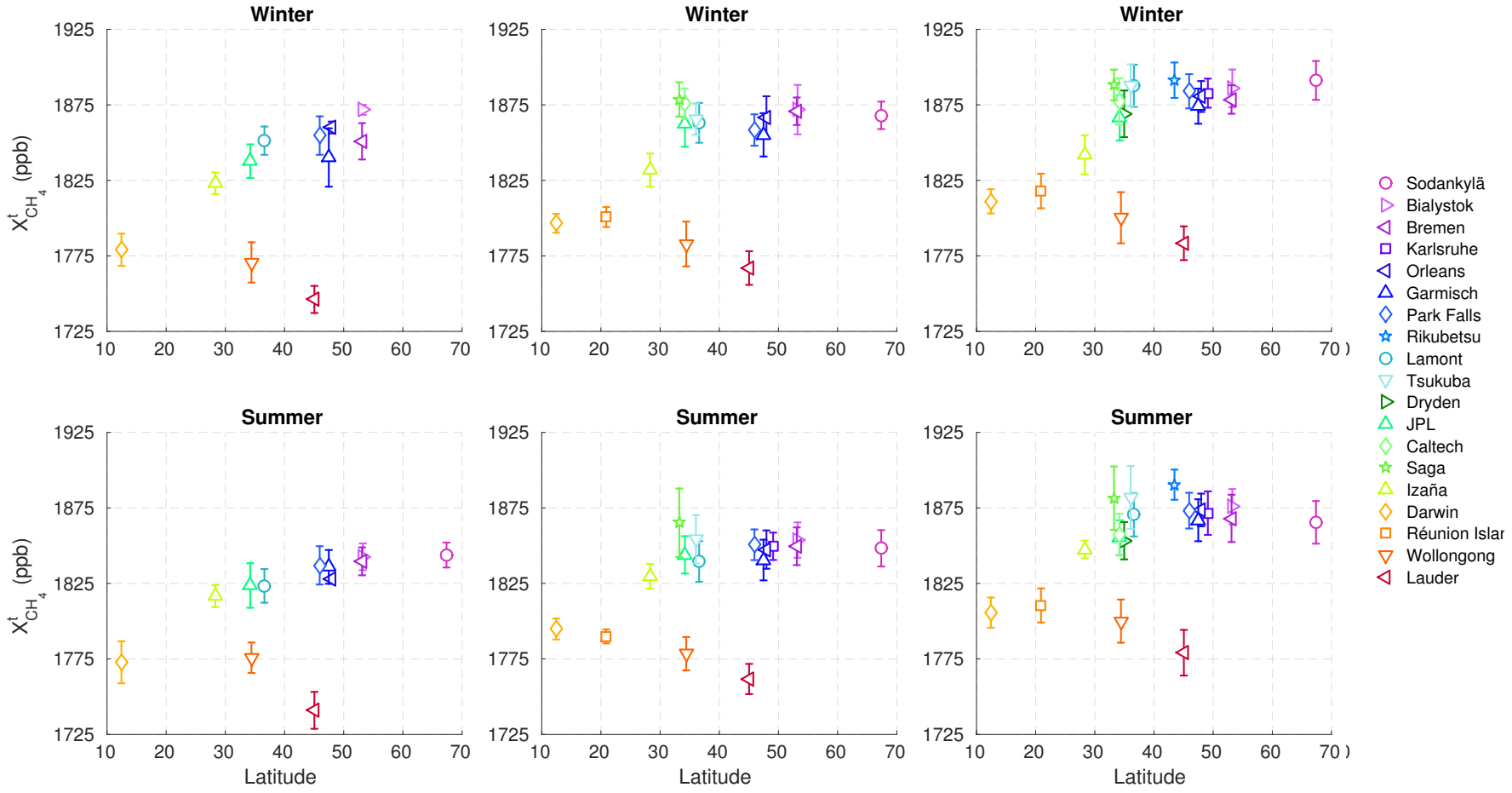

(a) 2007-2009 (b) 2010-2012 (c) 2013-2015

Figure 4.4: Seasonally averaged TCCON $X^t_{CH_4}$ vs. the absolute value of site latitude and their associated standard deviations. Cool and warm colors representing Northern and Southern Hemisphere sites, respectively.

We run York linear regressions on seasonally-averaged detrended $X^t_{CH_4}$ ($\widetilde{X}^t_{CH_4}$) and θ_{700}, weighted by corresponding standard deviations (York et al. 2004). Comparing mean statistics for each site minimizes potential representation bias resulting from different sample sizes, but also increases the statistical uncertainty of the regression. Repeating the comparison using various types of signal processing filters for synoptic and detrended time decompositions does not change temporal trends in the meridional gradients; we thus find the results to be robust to the chosen methodology.

4.2.2 Changing Distribution of CH_4 in θ-tracer Space

Figure 4.5 illustrates the relationship between $\widetilde{X}^t_{CH_4}$ and θ_{700} in winter (DJF in the Northern Hemisphere and JJA in the Southern Hemisphere) and summer (JJA in the Northern Hemisphere and DJF in the Southern Hemisphere). The effect of mixing on horizontal gradients is apparent in the winter; $\widetilde{X}^t_{CH_4}$ at sites north of Izaña fall within a range of about 25 ppb, and the standard deviations of θ_{700} are relatively large and overlap across sites. By contrast, in the summer, the narrower inter-site spread of θ_{700} and smaller individual Northern Hemisphere site standard deviations correspond to weaker meridional advection.

To assess whether these gradients have changed, we group these seasonal mean and variance plots into three time periods: 2007-2009, 2010-2012 and 2013-2015, which correspond to inflection points in the long-term trend of NOAA globally-averaged surface concentrations of CH_4. Comparing these set of plots, the relationship between $\widetilde{X}^t_{CH_4}$ and θ_{700} is broadly consistent across the Northern Hemisphere sites. The summertime trend, however, varies considerable over the nine years. In 2007-2009, a noticeable jump in $\widetilde{X}^t_{CH_4}$ exists between sites "north" of 307K, on average 32 ppb, and those "south" of 312K, on average 21 ppb. This jump is persistent in the subsequent time periods, but the behavior of the two clusters shifts: the meridional gradient at the sub-tropical sites becomes much steeper, and the difference in $\widetilde{X}^t_{CH_4}$ between the mid-latitudes and sub-tropics disappears. In 2010-2012, all sites poleward of 45°N decrease by 6 ppb on average; the only exception is Bialystok, which increases by the same difference. Although $\widetilde{X}^t_{CH_4}$ at JPL and Izaña decrease, Tsukuba and Saga, at 312K and 314K respectively, begin taking measurements, with values at the upper range of the mid-latitudes. In 2013-2015, $\widetilde{X}^t_{CH_4}$ at 45°N-50°N increases slightly, on average 3 ppb, but decreases or stays constant at the sites further north. $\widetilde{X}^t_{CH_4}$ increases at all sub-tropical sites, by contrast, with the largest increases at Lamont and Tsukuba. The Southern Hemisphere seasonal mean $\widetilde{X}^t_{CH_4}$ are consistent across the three time periods, excepting slightly higher 2007-2009

values at Darwin during winter and at Wollongong during summer.

By considering $\widetilde{X}^t_{CH_4}$ as a function of θ_{700}, we can better characterize the changing trend in the difference between the Park Falls and Lamont time series (Fig. 4.3). $\widetilde{X}^t_{CH_4}$ at Park Falls is on average 32 ppb in the summer and about 45 ppb the winter, except in 2010-2012 when $\widetilde{X}^t_{CH_4}$ drops to 39 ppb. Thus, $X^t_{CH_4}$ at Park Falls has generally tracked the global long-term trend since 2007. The changing gradient between these two sites appears to be driven by Lamont: $\widetilde{X}^t_{CH_4}$ increases 5 ppb in the winter and 13 ppb in the summer. $\widetilde{X}^t_{CH_4}$ at Tsukuba, which is only 6° south of Lamont, similarly increases from 2010-2012 to 2013-2015. In θ-tracer space, Tsukuba is dynamically poleward of Lamont (i.e. θ_{700} is colder), and in the winter, its $\widetilde{X}^t_{CH_4}$ values fall between those of Park Falls and Lamont. In the summer, however $\widetilde{X}^t_{CH_4}$ at Tsukuba is nearly equal that at Park Falls in 2010-2012 and considerably higher in 2013-2015. These differences support the hypothesis that a change in the distribution of tropospheric CH_4 causes the bifurcation between the sites equatorward of Lamont and the sites poleward of 40°N apparent in the summer plots. Any change in the spatial distribution could be the result of changing emissions, OH concentrations, or advection. If the differences observed in the relationship between Park Falls and Lamont were due to a change in transport, a similar shift would exist in the X_{CO_2} time series; however, the relationship between these sites remains fairly stable (Fig. 4.12).

Table 4.1: York Regression Slopes (ppb·K^{-1}) and Correlation Coefficients of $\widetilde{X}^t_{CH_4}$ vs. θ_{700} (Fig. 4.5)

	Winter					
	2007-2009	R^2	2010-2012	R^2	2013-2015	R^2
Northern Hemisphere	−1.5 ± 0.4	0.67	−1.4 ± 0.3	0.24	−1.9 ± 0.4	0.23
Continuous Sites	−1.7 ± 0.4	0.76	−1.8 ± 0.4	0.60	−2.2 ± 0.4	0.55
45°N-60°N	−2.4 ± 2.0	0.45	−4.1 ± 4.0	0.00	−1.1 ± 1.0	0.42
25°N-40°N	−3.5 ± 2.0	0.83	−3.0 ± 1.0	0.00	−3.3 ± 0.8	0.40
Southern Hemisphere	1.8 ± 0.5	0.79	1.3 ± 0.4	0.83	1.6 ± 0.4	0.80
	Summer					
	2007-2009	R^2	2010-2012	R^2	2013-2015	R^2
Northern Hemisphere	−1.2 ± 0.4	0.64	−1.2 ± 0.4	0.00	−1.7 ± 0.4	0.00
Continuous Sites	−1.3 ± 0.5	0.75	−1.5 ± 0.5	0.47	−1.5 ± 0.5	0.14
45°N-60°N	−0.8 ± 2.0	0.25	−6.6 ± 8.0	0.00	−0.9 ± 2.0	0.40
25°N-40°N	3.7 ± 7.0	0.40	−16.9 ± 20.0	0.00	−11.5 ± 9.0	0.71
Southern Hemisphere	3.4 ± 2.0	0.90	2.5 ± 1.0	0.93	2.9 ± 1.0	0.98

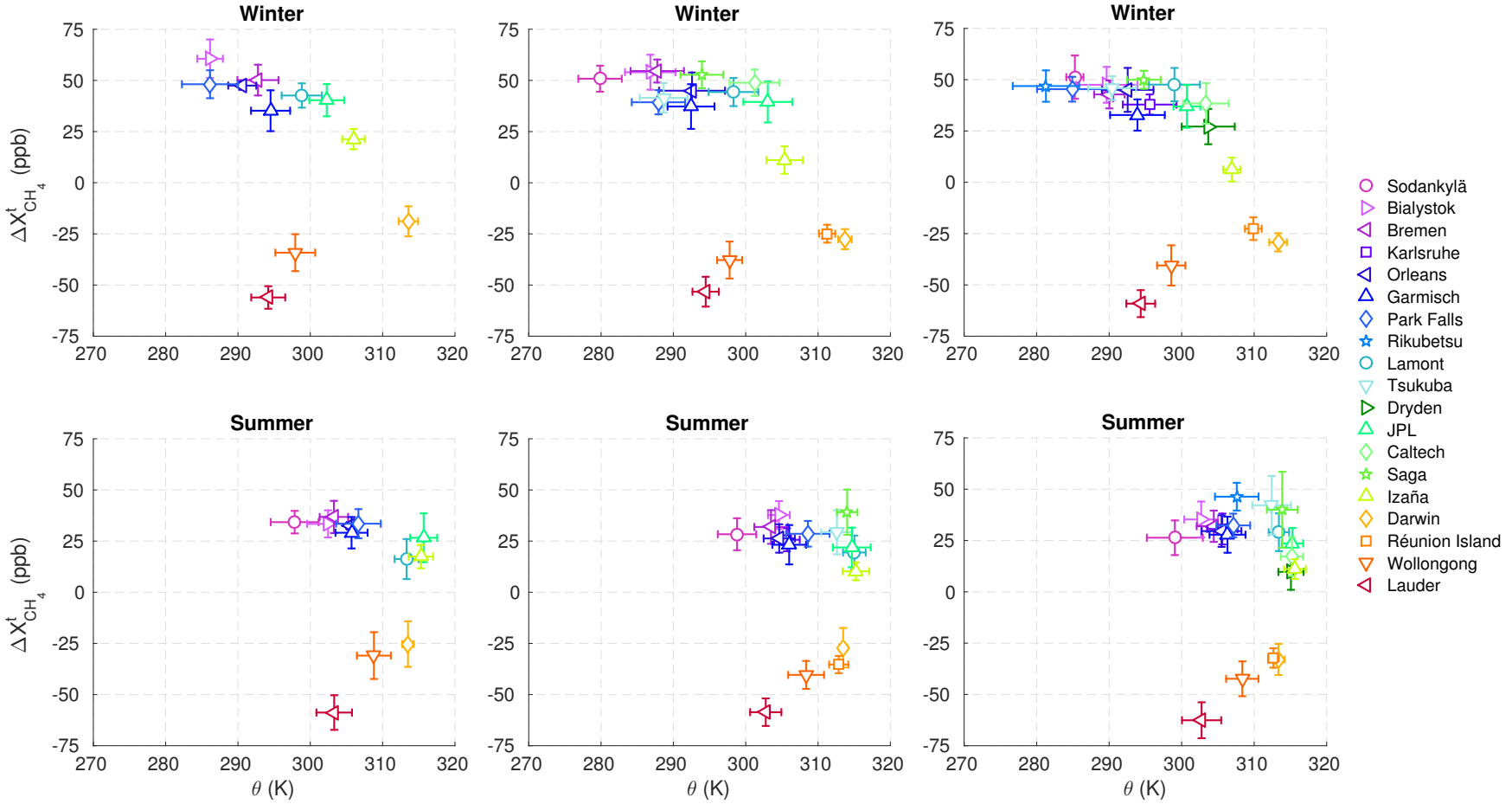

(a) 2007-2009 (b) 2010-2012 (c) 2013-2015

Figure 4.5: Seasonally averaged TCCON $\widetilde{X}^t_{CH_4}$ vs. θ_{700} and their associated standard deviations. Sites are sorted by latitude on a spectral color scale, with cool and warm colors representing Northern and Southern Hemisphere sites, respectively.

While zonal fluctuations are noteworthy findings, a shift in the meridional gradient with respect to θ_{700} presents a different signal of shifting horizontal gradients. Table 4.1 lists the slopes of the seasonal linear regression. Across the Northern Hemisphere, the slopes are relatively stable in both winter and summer. The 2013-2015 slopes are slightly steeper than previous years in both seasons, though they remain within the uncertainty. A comparison with the subset of sites that have at least one year of data in each of the three time periods (Sodankylä, Bialystok, Bremen, Orleans, Garmisch, Park Falls, Lamont and Izaña), which we term "continuous sites," corroborates the hypothesis that the inter-annual variability in the slopes is not driven by the addition of sites in the network. The higher R^2 values, however, likely reflect the expanded global coverage, as the later sites capture more of the spatial variability in the Northern Hemisphere, especially in the sub-tropics. Although the summer slopes across the continuous sites are stable, the R^2 values decrease with each time period, as a result of the differences between the mid-latitude and sub-tropical sites.

In the Northern Hemisphere, the mid-latitudes (40°N-70°N) and sub-tropics (25°N-40°N) have similar wintertime slopes throughout the three time periods. The sub-tropical slope is much more stable, likely mediated by Izaña, a high-altitude site in the Atlantic Ocean. The mid-latitude winter slope is quite variable, but the uncertainty is equivalent to the slope in each time period, which limit any conclusions that can be made about the decadal trend. Notably, in 2010-2012 $R^2 = 0$ for both the mid-latitudes and the sub-tropics, as opposed to at minimum 0.4 for the preceding and subsequent years. The implication is that θ_{700} explains none of the variance in $\widetilde{X}^t_{\mathrm{CH_4}}$ during this time period, which indicates that the processes governing $\mathrm{CH_4}$ trends in this time period are not captured by isolating the synoptic-scale variability. The 2010-2012 R^2 values are also 0 for both 45°N-60°N and 25°N-40°N in the summer, which suggests that the signal causing the unexplained variance may not have a seasonally-varying influence on $\widetilde{X}^t_{\mathrm{CH_4}}$. The anomalously low $\widetilde{X}^t_{\mathrm{CH_4}}$ in 2010-2012, described above, may be related to the unexplained variance.

Comparing the summer slopes of sites in these two zonal bands presents a starker contrast. The mid-latitude gradients are nearly equal (about $-1\,\mathrm{ppb\,K^{-1}}$), with equivalent uncertainties ($2\,\mathrm{ppb\,K^{-1}}$), in the first and last period; in 2010-2012, the slope is much more steep, -7 $\mathrm{ppb\,K^{-1}}$, which is driven by the $\widetilde{X}^t_{\mathrm{CH_4}}$ increase at Bialystok and the greater decrease in $\widetilde{X}^t_{\mathrm{CH_4}}$ across the European sites relative to the North American site of Park Falls.

In 2007-2009, the robustness of the sub-tropical summer slope suffers from the few number of sites; additionally, one of these, JPL, tends to have slightly high values of $\widetilde{X}^t_{CH_4}$ due to its proximity to the city of Los Angeles (Wunch et al. 2009). More telling is the equivalence in $\widetilde{X}^t_{CH_4}$ between Lamont and Izaña, which are separated by 8° latitude and 80° longitude, which suggests that the sub-tropical meridional gradient was relatively flat. The maxima of $\widetilde{X}^t_{CH_4}$ at Izaña occur in this time period, dropping from 21 to 11 ppb in the subsequent winter, and 17 to 10 ppb in the subsequent summer. A similar decline occurs at Darwin, from -21 in 2007-2009 to -28 ppb, in the following winter. This signal is consistent with the increase in the time series at Darwin through the beginning of 2009 (Fig. 4.14), as well as atmospheric inversions that attribute an increase to a tropical source (e.g. Bergamaschi et al. 2007; Dlugokencky et al. 2011). However, without additional observational constraints in the tropics, it is difficult to determine whether this increase was due to increased emissions or a weaker tropospheric sink.

The meridional gradients in the sub-tropics in the later years present the greatest evidence for the zonal origin for the changing distribution. The slopes in 2010-2012 and 2013-2015, -17 ppb K^{-1}, and -12 ppb K^{-1}, respectively, point to a large change in CH_4 fluxes in the sub-tropics, although the uncertainties in the slope remain very high. This gradient, supported by the additional measurements at Rikubetsu that help fill the data gap (Fig. 4.5c), indicate that the 2010-2012 and 2013-2015 increases in $X^t_{CH_4}$ is likely driven by changes in the balance between sources and sinks in the region of $\theta_{700} \approx 310K$.

4.2.3 Implications for the Spatial Distribution of Emissions

The region of $\theta_{700} = (310 \pm 2.5)K$ covers several areas recently associated with elevated CH_4 emissions (Fig. 4.6): the northern United States (Schneising et al. 2014; Peischl et al. 2016), Central and East Asia (Parker et al. 2011; Kim et al. 2015), and China in particular (Thompson et al. 2015). Over the United States specifically, the $\theta_{700} = (310 \pm 2.5)K$ region coincides with positive CH_4 anomalies derived from 2010-2014 Greenhouse gases Observing SATellite (GOSAT) measurements by Turner et al. (2016, ref. Figure 2), with the notable exceptions of the Northeast (strong positive anomaly) and Northern states (zero to weak positive anomaly). These differences may reflect the normalization scheme used to account for tropopause height or topography in the GOSAT data, although the latter would be less likely given the lack of prominent orographic features in these regions.

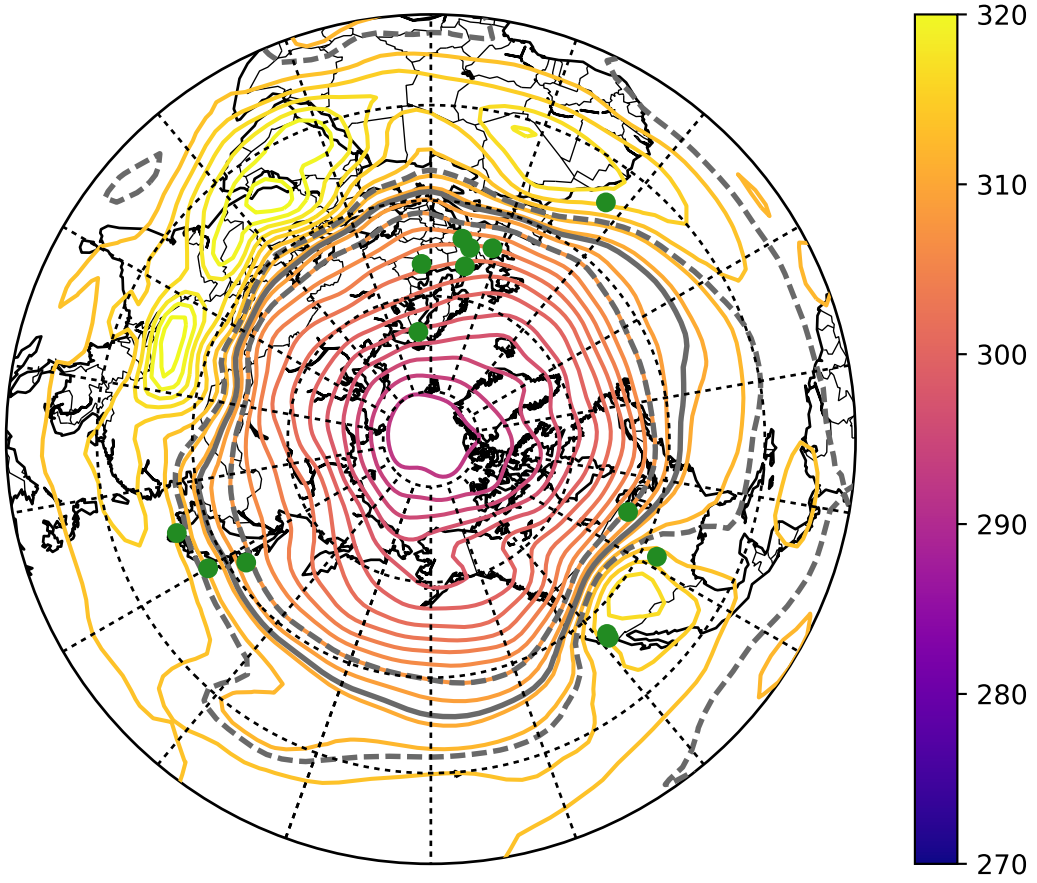

Figure 4.6: Contour map of Northern Hemisphere seasonal mean potential temperature (K), averaged for June-July-August over 2007-2015. Gray lines denote $\theta_{700} = 310K$ (solid) $\pm 2.5K$ (dashed). TCCON sites are marked in green. Latitude lines are in 20°increments from the equator to 80°N.

In isolating the influence of synoptic-scale transport on the spatial distribution of CH_4 over the period of global methane growth, we find that (1) the summertime meridional gradient of $X^t_{CH_4}$ is relatively constant in the Southern Hemisphere, and (2) the Northern Hemisphere gradient has become weaker in the past decade, reducing the divide between the mid-latitudes and subtropics. This shift in the gradient indicates that either CH_4 emissions have been increasing or OH has been decreasing in the Northern extratropics. An increasing source at $\theta_{700} = 310K$ is consistent with higher anthropogenic emissions in the central and northern United States and East Asia.

4.3 Relating Distributions of CH_4 Emissions and OH to Meridional Gradients of CH_4

4.3.1 Model Simulations and Methods

To identify possible drivers of the signal of a sub-tropical source, we compare the observed dependence of $\widetilde{X}^t_{CH_4}$ on θ_{700} to that of the GEOS-Chem chemical transport model (Bey et al. 2001; Wang et al. 2004; Wecht et al. 2014b). We run a base simulation from January 2005 through June 2013 as in Saad et al. (2016), using the base simulation's last CH_4 instantaneous fields as initial conditions, which eliminates the initial offset in the comparison with TCCON $X^t_{CH_4}$. To extend the time series, we apply the last year of available GFED3 biomass burning daily emissions (Mu et al. 2011; Werf et al. 2010), 2011, to subsequent years. Model smoothing and corrections are applied identically to the methodology described in Saad et al. (2016). GEOS-Chem $X^t_{CH_4}$ are detrended by subtracting the long-term trend, derived from the model grid box at the longitude, latitude and altitude of Mauna Loa. θ_{700} is calculated from the National Aeronautics and Space Administration Global Modeling and Assimilation Office (NASA/GMAO) Goddard Earth Observing System Model, Version 5 (GEOS5) temperature and pressure daily mean profiles used by the model and smoothed with the same 3-21 day bandpass filter as in Section 4.2.1.

4.3.2 Measurement-Model Agreement in CH_4 Meridional Gradients

Compared to those of TCCON, the meridional gradients of $\widetilde{X}^t_{CH_4}$ in the GEOS-Chem simulations are larger throughout the Northern Hemisphere and smaller in the Southern Hemisphere in 2007-2009 (Figure 4.7a, top). This trend persists in 2010-2012 (Figure 4.7b, top), although the measurement-model disagreement in the Northern Hemisphere gradients is less severe. In the summer, the GEOS-Chem Southern Hemisphere gradient in 2007-2009 is also smaller than the measurements; however, the Northern mid-latitude gradient agrees well with TCCON (Figure 4.7a, bottom). Notably, the best measurement-model agreement occurs in the 2010-2012 Southern Hemisphere summer (Figure 4.7b, bottom).

While the GEOS-Chem Northern Hemisphere summertime gradients are also too large in 2007-2009, they differ from TCCON less than during the winter of the same time period (Figure 4.7a, bottom). The largest deviation, excepting JPL, whose local sources are smoothed by the horizontal resolution of the model, is at Lamont: GEOS-Chem $\widetilde{X}^t_{CH_4}$ is about 7 ppb greater than TCCON. This difference decreases by half in 2010-2012; indeed, the summertime difference between TCCON and GEOS-Chem $\widetilde{X}^t_{CH_4}$ is within ±4 ppb across all sub-tropical sites, except for Saga. While $\widetilde{X}^t_{CH_4}$ at the

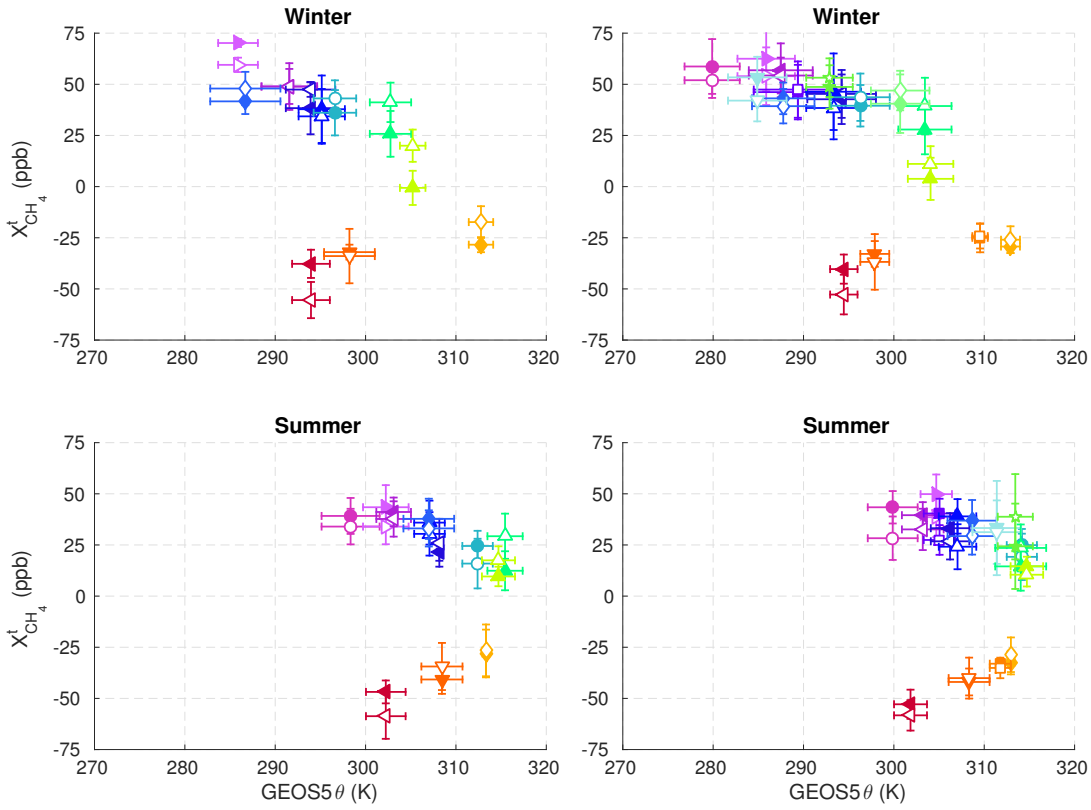

(a) 2007-2009 (b) 2010-2012

Figure 4.7: Seasonally averaged GEOS-Chem (filled) and TCCON (open) $\widetilde{X}^t_{\mathrm{CH_4}}$ vs. GEOS5 θ_{700}, and their associated standard deviations.

mid-latitude sites remain overestimated compared to the sub-tropics, the simulated meridional gradients do agree remarkably well with observations during this time period (Figure 4.7b, bottom). This suggests that either the spatial distribution of GEOS-Chem's a priori emissions, which has little interannual variability, or OH, which does not vary annually in the model, was not correct during the initial period of renewed CH_4 growth. However, in 2010-2012, although high latitude $\widetilde{X}^t_{\mathrm{CH_4}}$ still seem to be overestimated, the measurement-model agreement in the subtropics indicates that the balance of fluxes in these regions may be adequately represented.

4.3.3 Prior Emissions and OH Distributions Exhibit Covariance in Region of Increasing CH_4

Figure 4.8 shows the zonal monthly mean CH_4 emissions (Tg), averaged across all years of the simulation, with GEOS5 θ_{700} isolines superimposed. Throughout the year, the largest sources are in the grid boxes from 24°N–44°N. From late spring

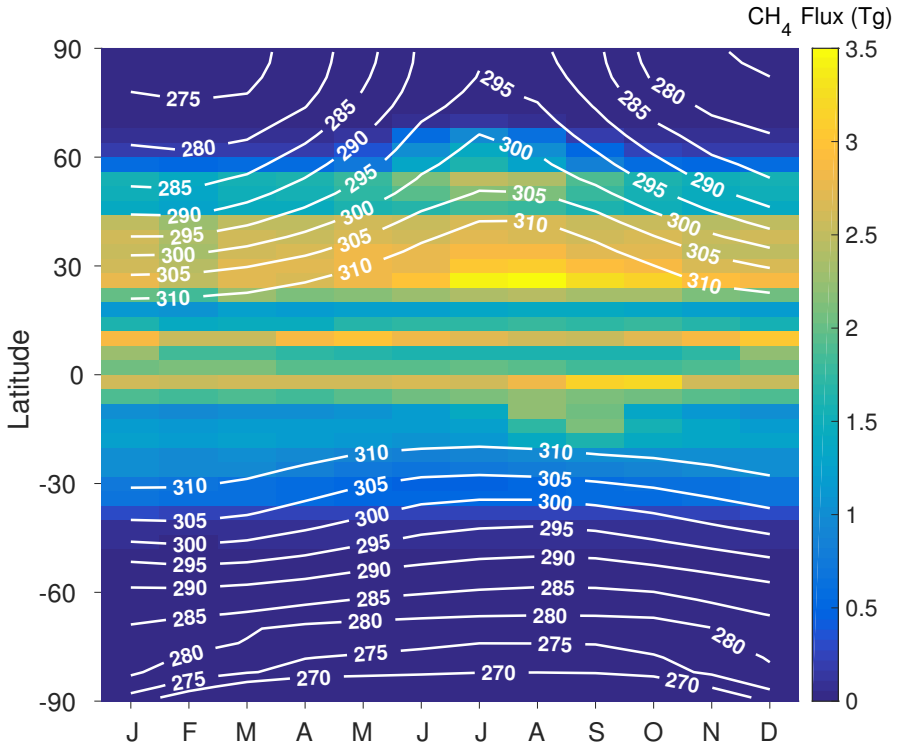

Figure 4.8: Monthly mean CH_4 emissions (Tg) in the GEOS-Chem simulations, averaged over 2005-2012, summed over each zonal band. Monthly zonal mean GEOS5 θ_{700} isolines, averaged over 2005-2012, are shown in white.

through early fall, this is also the zonal band where $\theta_{700} = (310 \pm 2.5)K$, although the highest emissions occur 10° south of the 310 K isoline.

While the agreement between the measured and simulated meridional gradients suggests that the model distribution of fluxes may be broadly correct in 2010-2012, the attribution to any one sector is problematic. First, the bottom-up estimates of emissions, on which a priori model values are based, vary widely in terms of both magnitude and distribution (Kirschke et al. 2013). Second, the largest peak in Northern Hemisphere emissions, as a function of GEOS5 θ_{700}, occurs at $\theta_{700} = 312K$ for nearly all emissions sectors in the model (Figure 4.9a). The shoulder at $\theta_{700} = 310K$ is much smaller, but slightly more constrained: livestock, coal, and to a lesser extent rice agriculture capture most of the increase.

In addition to the covariance between emission types, CH_4 emissions also covary with OH, further complicating attribution. Figure 4.9b shows the Northern Hemisphere CH_4 tropospheric column loss in the base simulation for each 1 K increment of θ_{700}. While the distribution dynamically poleward of the sub-tropics is much more flat than that of the total emissions, the most prominent feature is strikingly

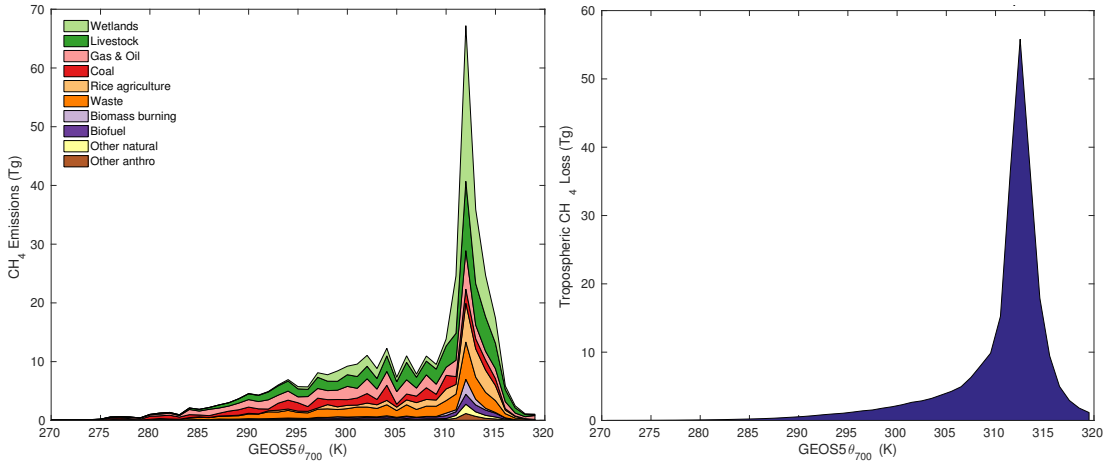

(a) (b)

Figure 4.9: Monthly mean Northern Hemisphere (a) CH_4 emissions and (b) tropospheric column CH_4 loss ($TgCH_4\,K^{-1}$) in the GEOS-Chem base simulation, averaged over 2007-2012, summed for θ_{700} in 1 K bins. Note the different vertical scales in (a) and (b).

similar: a peak at $\theta_{700} = 312K$ that accounts for most of the CH_4 flux globally.

Beyond this global, annual snapshot of the variability of fluxes with respect to θ, Figure 4.10 illustrates how the balance between emissions and loss ($E - L$) varies both zonally and seasonally. Positive $E - L$ values are for the most part contained in the Northern Hemisphere zonal band from the sub-tropics to the high mid-latitudes. Within this region, the seasonal trend exhibits a bifurcation at 52°N: poleward of this line, $E - L$ is larger in the summer versus winter, and equatorward, $E - L$ is smaller. The associated seasonally-varying meridional gradient results in the maximum $E-L$ values being centered on 54°N in the summer, when north-south mixing is weak. During winter, when meridional transport is strongest, the maximum $E-L$ values are in the sub-tropics. A second clear demarcation occurs at 44°N: meridional gradients increase poleward both south and north of this latitude. Although the more northern gradient does not appear in the TCCON observations, the sub-tropical gradient is consistent with the location of inferred CH_4 increase shown in Figure 4.6.

4.4 Conclusions

The summertime meridional gradient of tropospheric CH_4 has shifted in the past decade, reducing the divide between the Northern Hemisphere mid-latitudes and subtropics. These gradients have been decreasing concurrently with the increasing growth rate, indicating that the fluxes are shifting southward. We identify

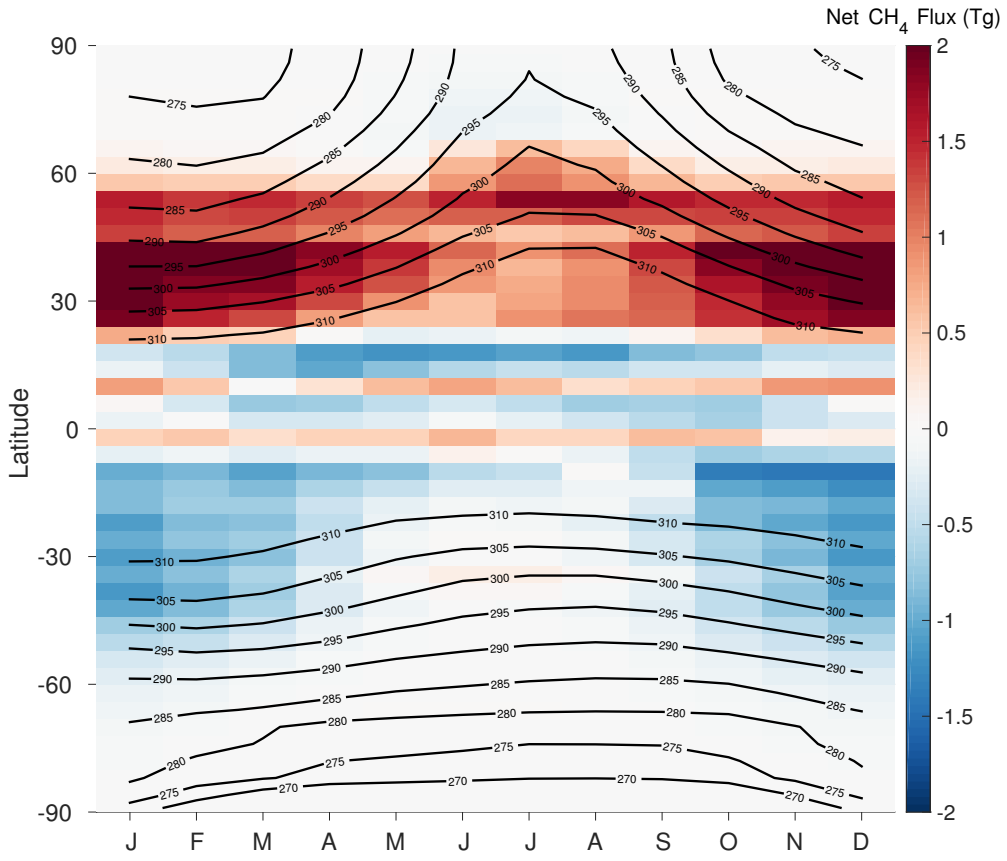

Figure 4.10: The monthly difference between CH_4 emissions and tropospheric column loss (Tg), summed over each zonal band and averaged over 2005-2012, in the GEOS-Chem base simulation. Monthly zonal mean GEOS5 θ_{700} isolines, averaged over 2005-2012, are shown in black.

$\theta_{700} = 310K$ as the probable zonal band in which OH has been decreasing or CH_4 emissions have been increasing, the latter of which would be consistent with increased anthropogenic emissions in the central and northern US and East Asia. However, the strong covariance between a priori emissions sectors, as well as OH distributions, in θ-tracer space renders any attempts to distinguishing between these fluxes ineffective, given the sparsity of CH_4 data. Thus, the problem of why CH_4 has been increasing in the last decade remains an open question.

This work has demonstrated the benefit of isolating the signals of synoptic-scale transport in observations to diagnose zonal trends. We find that the robust signal of the shifting meridional gradients tracking the increased global growth rate requires that any proposed solution to this problem must explain both trends. Ideally, models would provide a reliable sensitivity of meridional gradients to zonal perturbations in emissions and loss processes, so that model experiments could be used to compare

possible drivers of temporal shifts in gradients and to quantify the contribution to global atmospheric trends. However, the dynamics of models are currently insufficient to evaluate various explanations with adequate confidence. The ability to resolve the dependencies of CH_4 with respect to the spatial distribution of surface fluxes and chemical loss would be necessary for model-based source attribution to accurately describe trends in underlying processes.

The approach of using θ_{700} as a dynamical tracer would be substantially improved with denser spatial coverage of column measurements, especially those that can provide insight on whether these sites truly represent zonal means. In addition to adding observations in the tropics, we propose that constraining the variability in longitude is required to differentiate local hot spots from regional trends. Accurate satellite measurements that can resolve zonal gradients and disentangle the problems of model covariance will be critical to conclusively determining drivers of tropospheric CH_4 distributions, and thus trends.

Appendix A

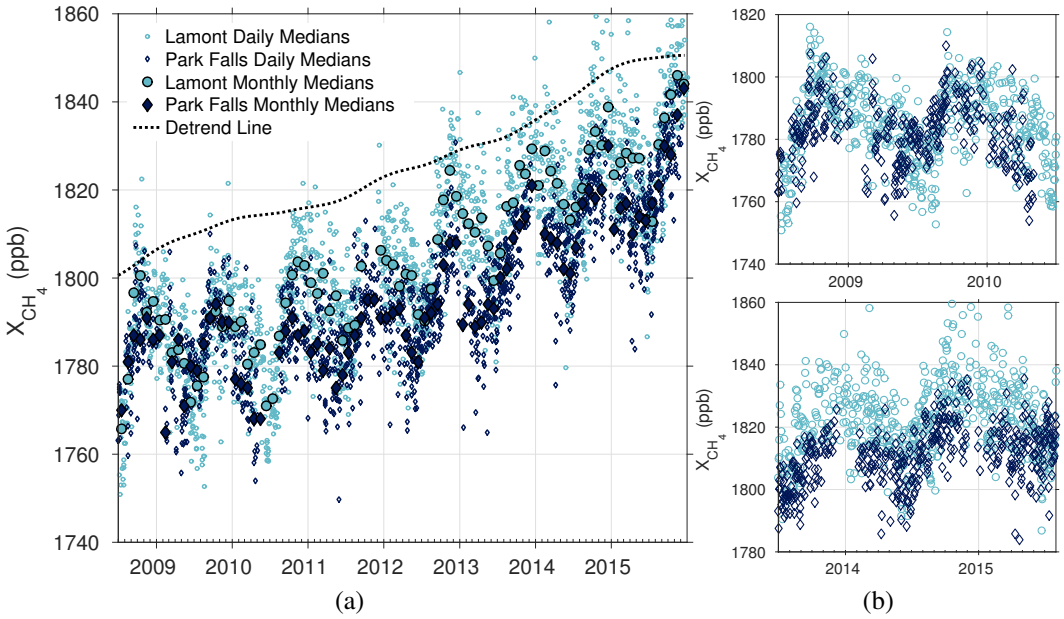

Figure 4.11: a) Daily (open) and monthly (filled) median TCCON X_{CH_4} at Park Falls and Lamont from July 2008 to January 2016, with long-term trend line (black) at Mauna Loa. b) Enlargement of (a) over July 2008-July 2010 (top) and July 2013-July 2015 (bottom) with monthly medians excluded.

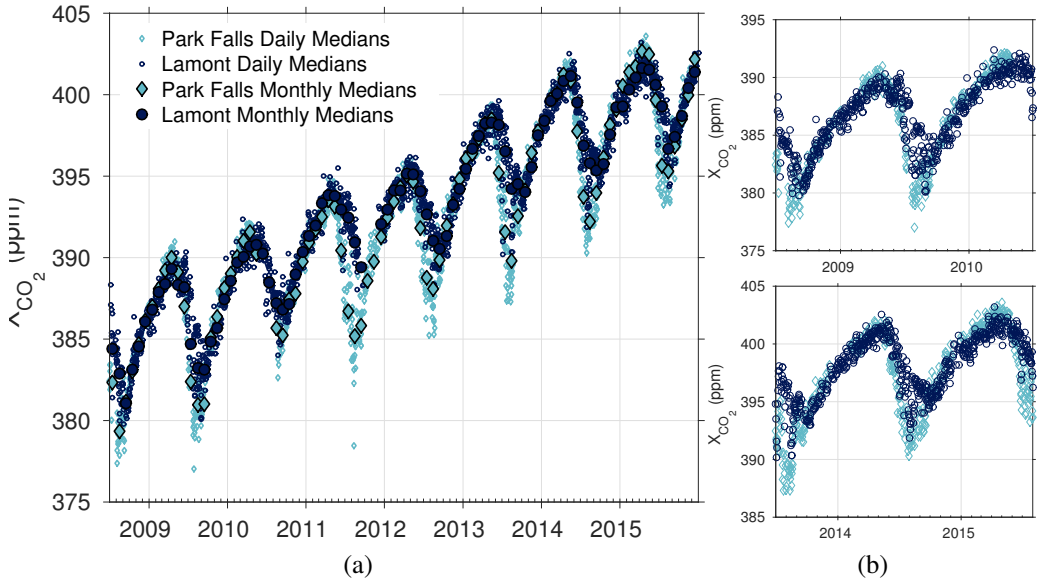

Figure 4.12: a) Daily (open) and monthly (filled) median TCCON X_{CO_2} at Park Falls and Lamont from July 2008 to January 2016. b) Enlargement of (a) over July 2008-July 2010 (top) and July 2013-July 2015 (bottom) with monthly medians excluded.

Table 4.2: TCCON sites, coordinates, altitudes, start date of measurements, and locations used in this analysis.

Site	Latitude (°)	Longitude (°)	Altitude (km)	Start date	Location	Data reference
Sodankylä	67.4	26.6	0.18	May 2009	Sodankylä, Finland	Kivi et al. (2014)
Bialystok	53.2	23.0	0.18	Mar 2009	Bialystok, Poland	Deutscher et al. (2014)
Bremen	53.1	8.9	0.03	Jan 2007	Bremen, Germany	Notholt et al. (2014)
Karlsruhe	49.1	8.4	0.11	Apr 2010	Karlsruhe, Germany	Hase et al. (2014)
Orleans	48.0	2.1	0.13	Aug 2009	Orleans, France	Warneke et al. (2014)
Garmisch	47.5	11.1	0.75	Jul 2007	Garmisch, Germany	Sussmann and Rettinger (2014)
Park Falls	45.9	−90.3	0.47	Jun 2004	Park Falls, WI, USA	Wennberg et al. (2014d)
Rikubetsu	43.5	143.8	0.36	Nov 2013	Rikubetsu, Japan	Morino et al. (2014b)
Lamont	36.6	−97.5	0.32	Jul 2008	Lamont, OK, USA	Wennberg et al. (2014c)
Tsukuba	36.0	140.1	0.03	Aug 2011	Tsukuba, Japan	Morino et al. (2014a)
Dryden	35.0	−117.9	0.70	Jul 2013	Dryden, CA, USA	Iraci et al. (2014)
JPL	34.2	−118.2	0.39	Jul 2007	Pasadena, CA, USA	Wennberg et al. (2014a) and Wennberg et al. (2014b)
Caltech	34.1	−118.1	0.23	Sep 2012	Pasadena, CA, USA	Wennberg et al. (2014e)
Saga	33.2	130.3	0.01	Jul 2011	Saga, Japan	Kawakami et al. (2014)
Izaña	28.3	−16.5	2.37	May 2007	Tenerife, Canary Islands	Blumenstock et al. (2014)
Darwin	−12.4	130.9	0.03	Aug 2005	Darwin, Australia	Griffith et al. (2014a)
Réunion Island	−20.9	55.5	0.09	Sep 2011	Saint-Denis, Réunion	De Maziere et al. (2014)
Wollongong	−34.4	150.9	0.03	Jun 2008	Wollongong, Australia	Griffith et al. (2014b)
Lauder	−45.0	169.7	0.37	Jun 2004	Lauder, New Zealand	Sherlock et al. (2014a, 2014b)

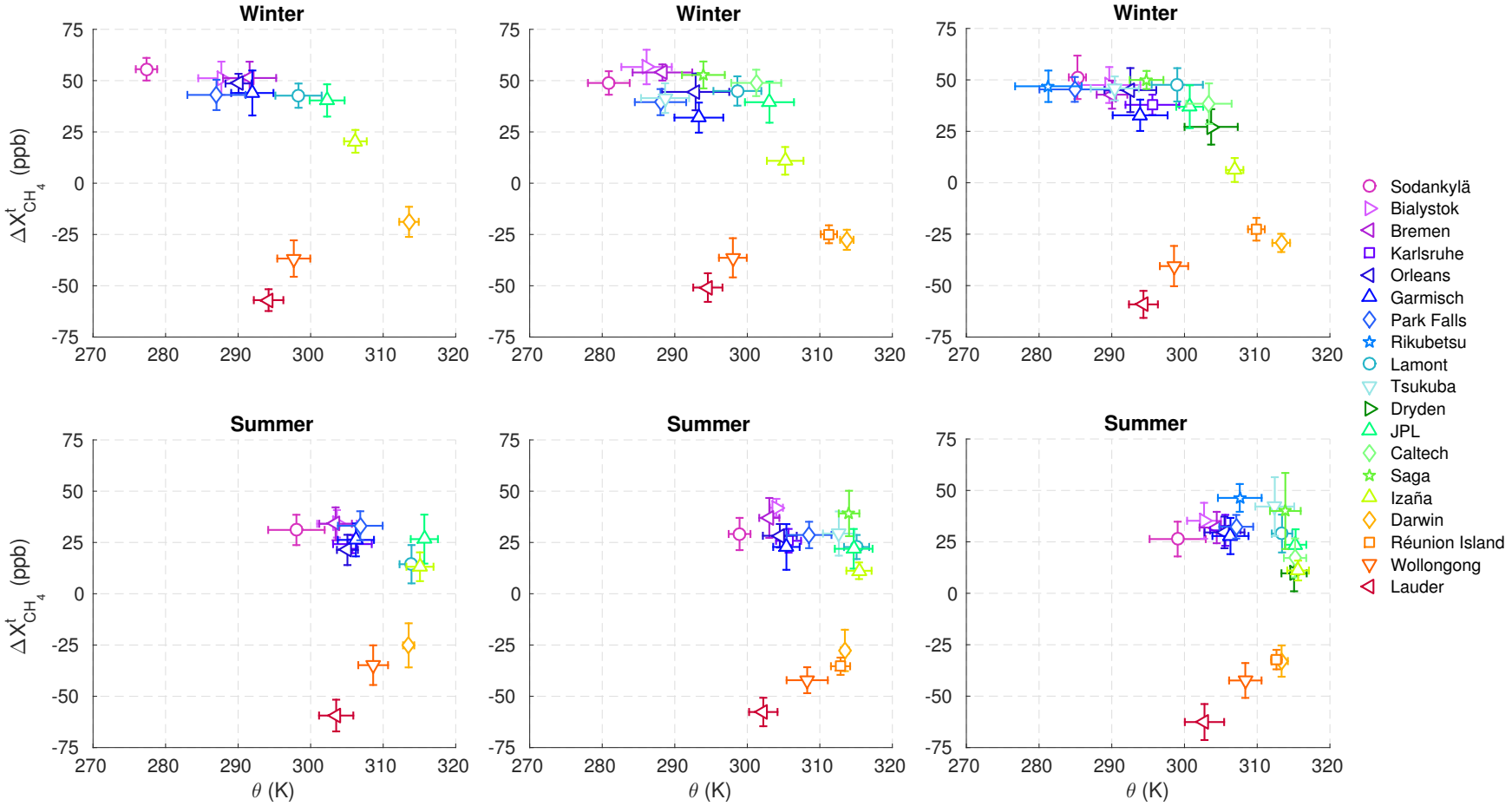

(a) 2007-2010 (b) 2011-2012 (c) 2013-2015

Figure 4.13: As Fig. 4.5, with seasonal averages over 2007-2010, 2011-2012, and 2013-2015.

Table 4.3: York Regression Slopes of $\widetilde{X}^t_{CH_4}$ vs. θ_{700} (Fig. 4.13)

	Winter					
	2007-2010	R^2	2011-2012	R^2	2013-2015	R^2
Northern Hemisphere	-1.1 ± 0.3	0.67	-1.5 ± 0.4	0.19	-1.9 ± 0.4	0.23
Continuous Sites	-1.2 ± 0.3	0.73	-1.8 ± 0.4	0.55	-2.2 ± 0.4	0.55
45°N-60°N	0.9 ± 2.0	0.00	-4.0 ± 3.0	0.23	-1.1 ± 1.0	0.42
25°N-40°N	-3.4 ± 2.0	0.79	-3.0 ± 1.0	0.00	-3.3 ± 0.8	0.40
Southern Hemisphere	1.9 ± 0.5	0.83	1.2 ± 0.4	0.82	1.6 ± 0.4	0.80
	Summer					
	2007-2010	R^2	2011-2012	R^2	2013-2015	R^2
Northern Hemisphere	-1.2 ± 0.5	0.40	-1.4 ± 0.4	0.00	-1.7 ± 0.4	0.00
Continuous Sites	-1.4 ± 0.6	0.65	-1.7 ± 0.4	0.30	-1.5 ± 0.5	0.14
45°N-60°N	-8.6 ± 10.0	0.00	-7.5 ± 6.0	0.00	-0.9 ± 2.0	0.40
25°N-40°N	9.8 ± 20.0	0.27	-15.2 ± 20.0	0.00	-11.5 ± 9.0	0.71
Southern Hemisphere	3.5 ± 2.0	0.95	2.2 ± 0.9	0.94	2.9 ± 1.0	0.98

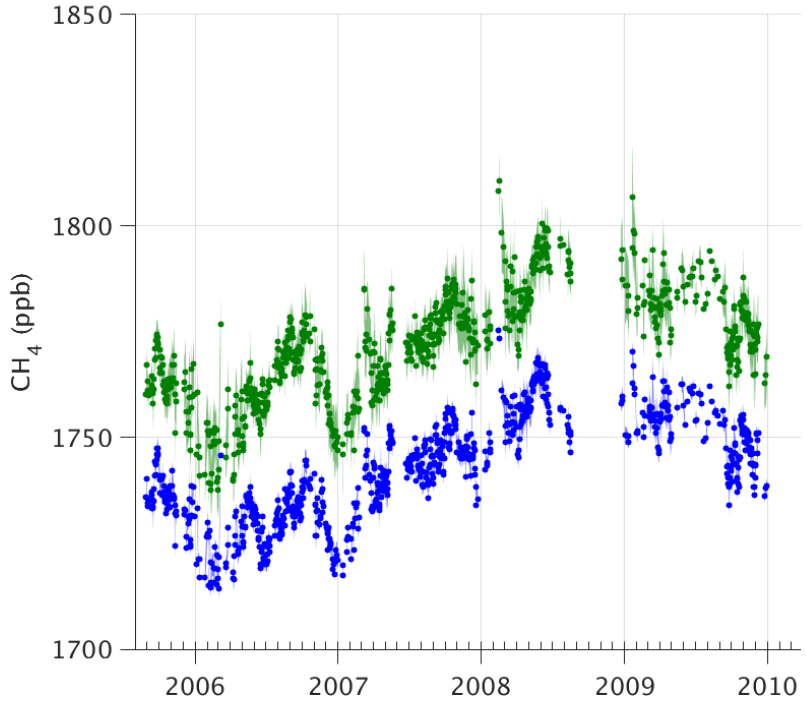

Figure 4.14: Daily median $X^t_{CH_4}$ and X_{CH_4} at Darwin from July 2006 to January 2010.

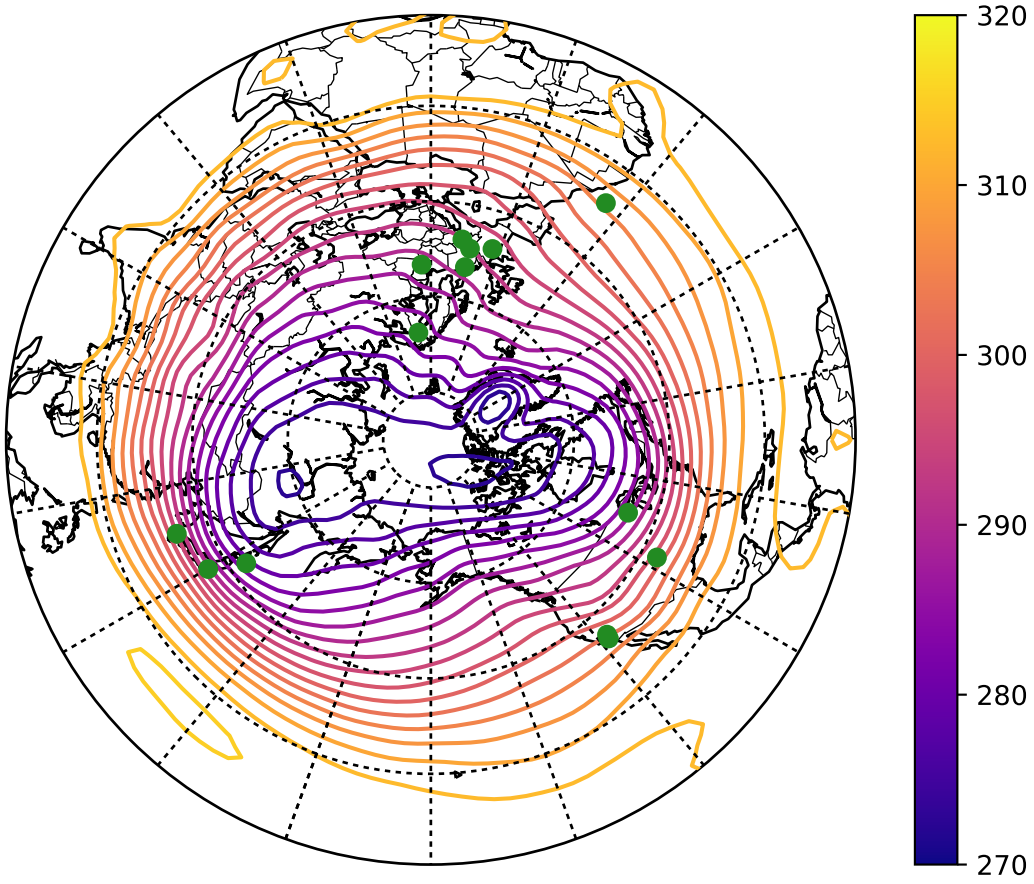

Figure 4.15: Contour map of Northern Hemisphere seasonal mean potential temperature (K), averaged for December-January-February over 2007-2015. TCCON sites are marked in green. Latitude lines are in 20°increments from the equator to 80°N.

Chapter 5

OUTLOOK

5.1 Improving Tropospheric Methane Partial Column Measurements

In developing a new dataset of tropospheric partial column-averaged dry-air mole fractions of CH_4, my research has involved synthesizing ground-based remote sensing measurements with satellite, aircraft and surface in situ data to contribute additional observational constraints to the global CH_4 budget. I have used these measurements to determine the ways in which model biases can alter our understanding of CH_4 trends, and investigate the influence of large-scale advection to the spatial distribution of CH_4.

This research has been one step in determining the relationship between CH_4 variability and its response to changing fluxes, to advance the much larger goal of resolving how those fluxes have been changing and could continue to change in the future. To reach that goal, these measurements of $X^t_{CH_4}$ can continually be improved, especially as more vertical profiles from in situ measurements allow us to assess the sensitivity of their accuracy to atmospheric conditions, such as stratospheric intrusions or pollution events. The inability to consider measurements with large HF errors resulting from strong H_2O features also poses a limitation that requires consideration in order to fully assess temporal variability on seasonal or shorter time scales, especially at sites in the tropics. Advancements in the total column retrievals will also improve the precision of the $X^t_{CH_4}$ measurements: for example, revising linelists, developing more accurate a priori profile shapes, correcting for temperature variability, and refining the quantification of airmass dependence. Such efforts will not only enhance observational constraints on the global CH_4 cycle, but will also allow for deeper examination on smaller spatial scales.

5.2 Distinguishing the Fossil-related Contribution to Methane Trends Chemical Tracers

Large urban areas provide a particular challenge to CH_4 source apportionment. The Los Angeles basin is a quintessential example of a difficult region to characterize, as it contains various fossil fuel and biogenic CH_4 sources, including petroleum production, natural gas pipelines, landfills, wastewater treatment facilities, and dairy farms (Wennberg et al. 2012). To differentiate between various anthropogenic and

biogenic CH_4 sources, non-methane hydrocarbons (NMHCs) and other trace gases can help differentiate between anthropogenic and biogenic emissions, which have distinct chemical compositions (Katzenstein et al. 2003; Xiao et al. 2008; Wunch et al. 2009; Hsu et al. 2010).

For example, lighter alkanes (C_2-C_4) are emitted from fuel degassing (natural gas and liquid petroleum gas); heavier alkanes (C_5-C_8) are emitted by unburned tailpipe emissions and evaporated fuel; and alkenes and alkynes are emitted by combustion processes (Baker et al. 2008). Natural gas accounts for most fossil-related ethane (C_2H_6) fluxes. Acetylene (C_2H_2), carbon monoxide (CO) and hydrogen cyanide (HCN) are all emitted during incomplete combustion: CO emissions are generally associated with agricultural waste and fossil fuels; C_2H_2 has been found to be mainly emitted by biofuel combustion; and the primary source of HCN is considered biomass burning (Xiao et al. 2007; Duflot et al. 2013).

The discovery of CH_4 occurred when Migeotte explored the suggestion of Sutherland and Callendar (1942) that "the 3.3μ region of the atmospheric spectrum was of special interest for the discovery of new compounds in the earth's atmosphere" (Migeotte 1948a), and the characterization of tropospheric CH_4 can be improved with measurements of other trace gases that also have signatures in this region. In addition to the InGaAs detector common to all TCCON sites, InSb detectors measure C_2H_6, C_2H_2, CO, and HCN, among other trace gases, in the 1850-5000cm^{-1} (mid-IR) spectral region. In comparing X_{CH_4} and $X_{C_2H_6}$ to the composition of natural gas distributed in Los Angeles, Wunch et al. (2016) have shown $X_{C_2H_6}$ to be an effective chemical tracer of fossil emissions of CH_4 in the Los Angeles basin, and we hypothesize that $X^t_{CH_4}$ will provide a stronger constraint.

The tropospheric partial column derivation methodology can be applied to these tracers as long as a stratospheric relationship with HF is obtained, and HCN in particular shows a robust correlation with HF in the ACE-FTS data. Previously, the HF-proxy method was determined unsuitable for calculating tropospheric C_2H_6 columns because ACE-FTS provided too few data points to determine the relationship with HF in the stratosphere, a limitation that was amplified by its low stratospheric abundance. However, as of late 2016, improvements in the satellite measurements have increased the available C_2H_6 data, and the development of climatological monthly mean zonal distributions have reintroduced the possibility of the development of a $X^t_{C_2H_6}$ dataset.

Additionally, a linelist for propane (C_3H_8) has been developed for the TCCON

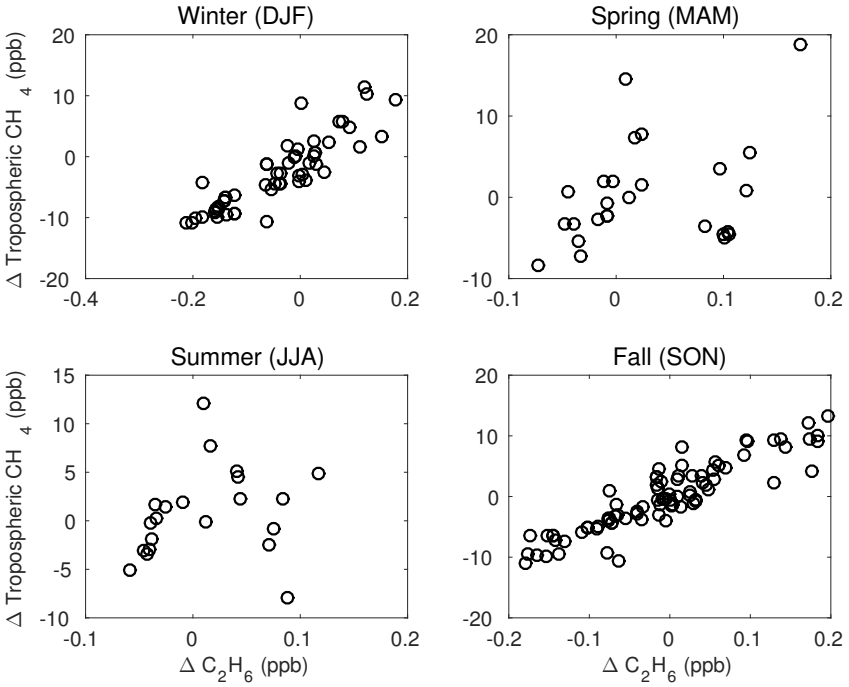

Figure 5.1: $X^t_{CH_4}$ and $X_{C_2H_6}$ daily anomalies over Pasadena, CA by season. Anomalies are calculated by subtracting DMFs at the same solar zenith angle (58°) before and after noon.

spectral fitting algorithm, GFIT, in the window centered around 2967 cm^{-1}. The second most abundant NMHC in the troposphere, C_3H_8 has a similar geospatial distribution to C_2H_6 but is more closely associated with liquefied petroleum gas emissions than natural gas; given its much shorter tropospheric lifetime (11 days), C_3H_8 is also less subject to long-range transport (Baker et al. 2008). Although measurements in this region are still susceptible to the H_2O vapor interference noted by Sutherland and Callendar (1942), initial spectral fits indicate that these measurements can provide additional constraints in polluted environments.

In order to isolate emission events from the long-term baseline, anomalies of each trace gas can be calculated and compared. Comparing daily anomalies, derived by subtracting DMFs at the same solar zenith angle before and after noon consistently with Wunch et al. (2009), isolates emission events from the long-term baseline, and basing the anomaly calculation on solar zenith angle minimizes the impact of airmass dependence on the measurements. CH_4 and C_2H_6 anomalies are well correlated during fall and winter, but are more scattered in summer and spring (Figure 5.1). By comparing more than two gases simultaneously, we can develop a more nuanced understanding of sources for clusters of measurements. For instance,

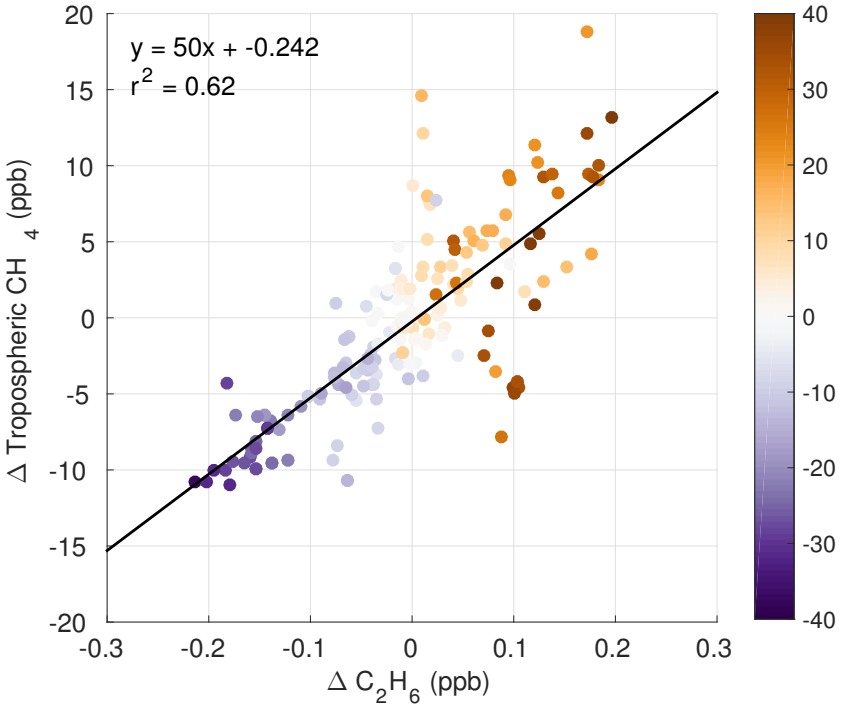

Figure 5.2: $X^{t}_{CH_4}$ and $X_{C_2H_6}$ daily anomalies over Pasadena, CA, calculated as in Figure 5.1, and colored by X_{CO} daily anomalies.

CO is emitted during incomplete combustion of biomass, agricultural waste, fossil fuels and biofuels, and larger deviations from the CH_4 versus C_2H_6 least squares line tend to occur during events with high positive CO (Figure 5.2).

The results from these comparisons will provide additional constraints on fossil emissions in Los Angeles, as well as allow us to characterize the temporal variability of CH_4 in an urban environment. These measurements can be combined with in situ surface and aircraft measurements of C_2H_6 and C_3H_8 near TCCON sites that do not measure these gases to compare urban from rural signatures.

These observations can then be fit into a wider context of how the natural gas trajectory has changed over this time period. Natural gas liquids such as C_2H_6 remain in the distribution system unless removed during production. Because fugitive emissions are estimated to enter the atmosphere throughout the natural gas life cycle (Brandt et al. 2014), the calculated loss rate of CH_4 from natural gas based on concurrent C_2H_6 emissions will vary depending on whether leaks occur before or after C_2H_6 processing and separation from commercial-grade natural gas. By comparing C_2H_6 observations to long-term changes in the natural gas trajectory, we can assess whether atmospheric concentrations are indicative of lower fugitive

emissions of CH_4 or the commercial viability of natural gas liquids such as C_2H_6 and C_3H_8.

Using the extensive datasets on natural gas production and the liquids extraction process from the US Energy Information Administration, the United States can provide an initial case study on whether higher levels of C_2H_6 have been removed from marketed natural gas over the same time period as CH_4 has been increasing in the troposphere. Preliminary work in analyzing the trajectory of natural gas in the United States using these inventories has revealed how the assumptions and reporting methodology in those dataset pose limitations in bottom-up estimates of energy-related emissions. Comparing the observations to the natural gas and petroleum inventories would provide a more detailed to understand the connection between fossil processing and distribution and fugitive emissions.

5.3 Future Directions in Observational Constraints

Increasing the spatial distribution of measurements will be paramount to monitoring changing emissions. Satellite missions such as Greenhouse gases Observing SATellite (GOSAT) (Parker et al. 2011) and the upcoming TROPOspheric Monitoring Instrument (TROPOMI) (Butz et al. 2012) can fill in gaps where ground measurements are sparse. Inversion studies that incorporate total column CH_4 data from the GOSAT satellite show a zonal bias in the mismatch (Turner et al. 2015), and discrepancies between GOSAT and TCCON CH_4 indicate that this could be caused in part to a bias in the satellite measurements (Parker et al. 2011). TCCON X_{CO_2} can be used to determine whether these discrepancies between the satellite measurements and model can be caused by airmass dependencies of the former. GOSAT CH_4 is calculated by multiplying the retrieved CH_4 to CO_2 ratio to coincident CO_2 mole fractions taken from the ACOS instrument on the same satellite or from a CTM simulation. Initial comparisons of TCCON CH_4 to GOSAT CH_4 derived from TCCON versus ACOS CO_2 show improved agreement with the ground-based data. Intercalibrating the TCCON and GOSAT CH_4 and CO_2 retrievals using their respective priors and averaging kernels will allow us to quantify the airmass dependence of GOSAT CH_4 as a function of latitude. The results of such work will have implications for the use of GOSAT total columns to correct modeled CH_4 concentrations.

The complexity of the global CH_4 cycle necessitates systematic and integrative approaches to distinguishing between biogenic and energy-related emissions con-

tributing to observed trends. Synthesizing sustained measurements with studies of system dynamics and model assessment will enhance our knowledge of the global CH_4 cycle, and the results will help inform communities involved in prediction and management policies.

BIBLIOGRAPHY

Allen, D., et al. 2010. "Impact of lightning NO emissions on North American photochemistry as determined using the Global Modeling Initiative (GMI) model." D22301, *Journal of Geophysical Research: Atmospheres* 115 (D22). doi:10.1029/2010JD014062. http://dx.doi.org/10.1029/2010JD014062.

Angelbratt, J., et al. 2011. "A new method to detect long term trends of methane (CH_4) and nitrous oxide (N_2O) total columns measured within the NDACC ground-based high resolution solar FTIR network." *Atmospheric Chemistry and Physics* 11, no. 13 (): 6167–6183. doi:10.5194/acp-11-6167-2011. http://www.atmos-chem-phys.net/11/6167/2011/.

Aselmann, I., and P. Crutzen. 1989. "Global distribution of natural freshwater wetlands and rice paddies, their net primary productivity, seasonality and possible methane emissions." *Journal of Atmospheric chemistry* 8 (4): 307–358.

Aydin, M., et al. 2011. "Recent decreases in fossil-fuel emissions of ethane and methane derived from firn air." *Nature* 476 (7359): 198–201. http://dx.doi.org/10.1038/nature10352.

Baker, A. K., et al. 2008. "Measurements of nonmethane hydrocarbons in 28 United States cities." *Atmospheric Environment* 42 (1): 170–182.

Baker, D. F., et al. 2006. "TransCom 3 inversion intercomparison: Impact of transport model errors on the interannual variability of regional CO2 fluxes, 1988–2003." GB1002, *Global Biogeochemical Cycles* 20 (1). doi:10.1029/2004GB002439. http://dx.doi.org/10.1029/2004GB002439.

Bates, D. R., and A. E. Witherspoon. 1952. "The Photo-Chemistry of Some Minor Constituents of the Earth's Atmosphere (CO2, CO, CH4, N2O)." *Monthly Notices of the Royal Astronomical Society* 112 (1): 101. doi:10.1093/mnras/112.1.101. http://dx.doi.org/10.1093/mnras/112.1.101.

Bates, K. H., et al. 2016. "Production and Fate of C4 Dihydroxycarbonyl Compounds from Isoprene Oxidation." *The Journal of Physical Chemistry A* 120 (1): 106–117. doi:10.1021/acs.jpca.5b10335. http://dx.doi.org/10.1021/acs.jpca.5b10335.

Bergamaschi, P., et al. 2007. "Satellite chartography of atmospheric methane from SCIAMACHY on board ENVISAT: 2. Evaluation based on inverse model simulations." D02304, *Journal of Geophysical Research: Atmospheres* 112 (D2). doi:10.1029/2006JD007268. http://dx.doi.org/10.1029/2006JD007268.

Bergamaschi, P., et al. 2013. "Atmospheric CH4 in the first decade of the 21st century: Inverse modeling analysis using SCIAMACHY satellite retrievals and NOAA surface measurements." *Journal of Geophysical Research: Atmospheres*

118 (13): 7350–7369. doi:10.1002/jgrd.50480. http://dx.doi.org/10.1002/jgrd.50480.

Bernath, P. F. 2005. "Atmospheric Chemistry Experiment (ACE): Mission overview." *Geophysical Research Letters* 32 (15): L15S01. doi:10.1029/2005GL022386. http://doi.wiley.com/10.1029/2005GL022386.

Bernath, P. 2017. "The Atmospheric Chemistry Experiment (ACE)." Satellite Remote Sensing and Spectroscopy: Joint ACE-Odin Meeting, October 2015, *Journal of Quantitative Spectroscopy and Radiative Transfer* 186:3–16. doi:http://dx.doi.org/10.1016/j.jqsrt.2016.04.006. //www.sciencedirect.com/science/article/pii/S0022407316300176.

Bey, I., et al. 2001. "Global modeling of tropospheric chemistry with assimilated meteorology: Model description and evaluation." *Journal of Geophysical Research-Atmospheres* 106, no. D19 (): 23073–23095. doi:10.1029/2001JD000807.

Blake, D. R., and F. S. Rowland. 1988. "Continuing Worldwide Increase in Tropospheric Methane, 1978 to 1987." *Science* 239, no. 4844 (): 1129. https://clsproxy.library.caltech.edu/docview/213532760?accountid=9841.

Blake, D. R., et al. 1982. "Global increase in atmospheric methane concentrations between 1978 and 1980." *Geophysical Research Letters* 9 (4): 477–480. doi:10.1029/GL009i004p00477. http://dx.doi.org/10.1029/GL009i004p00477.

Blumenstock, T., et al. 2014. *TCCON data from Izana, Tenerife, Spain, Release GGG2014R0*. http://dx.doi.org/10.14291/tccon.ggg2014.izana01.R0/1149295. doi:10.14291/tccon.ggg2014.izana01.R0/1149295.

Boering, K. A., et al. 1995. "Measurements of stratospheric carbon dioxide and water vapor at northern midlatitudes: Implications for troposphere-to-stratosphere transport." *Geophysical Research Letters* 22 (20): 2737–2740. doi:10.1029/95GL02337. http://dx.doi.org/10.1029/95GL02337.

Boering, K., et al. 1996. "Stratospheric Mean Ages and Transport Rates from Observations of Carbon Dioxide and Nitrous Oxide." *Science* 274 (5291): 1340–1343. doi:10.1126/science.274.5291.1340.

Boone, C. D., K. A. Walker, and P. F. Bernath. 2013. "Version 3 Retrievals for the Atmospheric Chemistry Experiment Fourier Transform Spectrometer (ACE-FTS)." In *The Atmospheric Chemistry Experiment ACE at 10: A Solar Occultation Anthology*, ed. by P. F. Bernath, 103–127. Hampton, Virginia, U.S.A.: A. Deepak Publishing.

Bousquet, P., et al. 2011. "Source attribution of the changes in atmospheric methane for 2006–2008." *Atmospheric Chemistry and Physics* 11 (8): 3689–3700. doi:10.5194/acp-11-3689-2011. http://www.atmos-chem-phys.net/11/3689/2011/.

Brandt, A. R., et al. 2014. "Methane Leaks from North American Natural Gas Systems." *Science* 343, no. 6172 (): 733–735. doi:10.1126/science.1247045. http://www.sciencemag.org/content/343/6172/733.full.

Brewer, A. 1949. "Evidence for a world circulation provided by the measurements of helium and water vapour distribution in the stratosphere." *Quarterly Journal of the Royal Meteorological Society* 75 (326): 351–363.

Buchwitz, M., et al. 2015. "The Greenhouse Gas Climate Change Initiative (GHG-CCI): Comparison and quality assessment of near-surface-sensitive satellite-derived CO_2 and CH_4 global data sets." *Remote Sensing of Environment* 162:344–362.

Burkholder, J., et al. 2015. *Chemical Kinetics and Photochemical Data for Use in Atmospheric Studies, Evaluation Number 18*. Tech. rep. JPL Publication 15-10. Jet Propulsion Laboratory, Pasadena, National Aeronautics and Space Administration. http://jpldataeval.jpl.nasa.gov.

Butz, A., et al. 2012. "TROPOMI aboard Sentinel-5 Precursor: Prospective performance of {CH4} retrievals for aerosol and cirrus loaded atmospheres." The Sentinel Missions - New Opportunities for Science, *Remote Sensing of Environment* 120:267–276. doi:http://dx.doi.org/10.1016/j.rse.2011.05.030. http://www.sciencedirect.com/science/article/pii/S003442571200082X.

Chang, T.-C., and S.-S. Yang. 2003. "Methane emission from wetlands in Taiwan." *Atmospheric Environment* 37 (32): 4551–4558.

Ciais, P., et al. 2013. "Carbon and Other Biogeochemical Cycles." Chap. 6 in *Climate Change 2013: The Physical Science Basis. Contribution of Working Group I to the Fifth Assessment Report of the Intergovernmental Panel on Climate Change*, ed. by T. Stocker et al., 465–570. Cambridge, United Kingdom and New York, NY, USA: Cambridge University Press. doi:10.1017/CBO9781107415324.015. www.climatechange2013.org.

Cicerone, R. J., J. D. Shetter, and C. C. Delwiche. 1983. "Seasonal variation of methane flux from a California rice paddy." *Journal of Geophysical Research: Oceans* 88 (C15): 11022–11024. doi:10.1029/JC088iC15p11022. http://dx.doi.org/10.1029/JC088iC15p11022.

Clarmann, T. von, et al. 2009. "Retrieval of temperature, H_2O, O_3, HNO_3, CH_4, N_2O, $ClONO_2$ and ClO from MIPAS reduced resolution nominal mode limb emission measurements." *Atmospheric Measurement Techniques* 2 (1): 159–175. doi:10.5194/amt-2-159-2009. http://www.atmos-meas-tech.net/2/159/2009/.

Connor, B. J., et al. 2008. "Orbiting Carbon Observatory: Inverse method and prospective error analysis." *Journal of Geophysical Research* 113:1–14. doi:10.1029/2006JD008336.

Considine, D. B., J. A. Logan, and M. A. Olsen. 2008. "Evaluation of near-tropopause ozone distributions in the Global Modeling Initiative combined stratosphere/troposphere model with ozonesonde data." *Atmospheric Chemistry and Physics* 8 (9): 2365–2385.

Crozier, C., I. Devai, and R. DeLaune. 1995. "Methane and reduced sulfur gas production by fresh and dried wetland soils." *Soil Science Society of America Journal* 59 (1): 277–284.

Crutzen, P. J., I. Aselmann, and W. Seiler. 1986. "Methane production by domestic animals, wild ruminants, other herbivorous fauna, and humans." *Tellus B* 38B (3-4): 271–284. doi:10.1111/j.1600-0889.1986.tb00193.x. http://dx.doi.org/10.1111/j.1600-0889.1986.tb00193.x.

Crutzen, P. J., et al. 1979. "Biomass burning as a source of atmospheric gases CO, H2, N2O, NO, CH3Cl and COS." *Nature* 282:253–256.

De Maziere, M., et al. 2014. *TCCON data from Reunion Island (La Reunion), France, Release GGG2014R0*. http://dx.doi.org/10.14291/tccon.ggg2014.reunion01.R0/1149288. doi:10.14291/tccon.ggg2014.reunion01.R0/1149288.

De Mazière, M., et al. 2008. "Validation of ACE-FTS v2.2 methane profiles from the upper troposphere to the lower mesosphere." *Atmospheric Chemistry and Physics* 8 (9): 2421–2435. doi:10.5194/acp-8-2421-2008. http://www.atmos-chem-phys.net/8/2421/2008/.

Deutscher, N., et al. 2014. *TCCON data from Bialystok, Poland, Release GGG2014R1*. http://dx.doi.org/10.14291/tccon.ggg2014.bialystok01.R1/1183984. doi:10.14291/tccon.ggg2014.bialystok01.R1/1183984.

Dlugokencky, E. J. 2005. "Conversion of NOAA atmospheric dry air CH_4 mole fractions to a gravimetrically prepared standard scale." *Journal of Geophysical Research* 110 (D18): D18306. doi:10.1029/2005JD006035. http://doi.wiley.com/10.1029/2005JD006035.

Dlugokencky, E. J., et al. 2009. "Observational constraints on recent increases in the atmospheric CH4 burden." *Geophys. Res. Lett.* 36, no. 18 (): L18803. doi:10.1029/2009GL039780. http://doi.wiley.com/10.1029/2009GL039780.

Dlugokencky, E. J., et al. 2011. "Global atmospheric methane: budget, changes and dangers." *Philosophical Transactions of the Royal Society of London A: Mathematical, Physical and Engineering Sciences* 369 (1943): 2058–2072. doi:10.1098/rsta.2010.0341. http://rsta.royalsocietypublishing.org/content/369/1943/2058.

Dlugokencky, E., et al. 2016. *Atmospheric Methane Dry Air Mole Fractions from the NOAA ESRL Carbon Cycle Cooperative Global Air Sampling Network, 1983-2015*. ftp://aftp.cmdl.noaa.gov/data/trace_gases/ch4/flask/surface/. Version 2016-01-04 T16:28:31.

Dobson, G. 1956. "Origin and distribution of the polyatomic molecules in the atmosphere." *Proceedings of the Royal Society of London. Series A, Mathematical and Physical Sciences* 236 (1205): 187–193.

Dohe, S., et al. 2013. "A method to correct sampling ghosts in historic near-infrared Fourier transform spectrometer (FTS) measurements." *Atmospheric Measurement Techniques* 6 (8): 1981–1992.

Duflot, V., et al. 2013. "Measurements of hydrogen cyanide (HCN) and acetylene (C_2H_2) from the Infrared Atmospheric Sounding Interferometer (IASI)." *Atmospheric Measurement Techniques* 6 (4): 917–925. doi:10.5194/amt-6-917-2013. http://www.atmos-meas-tech.net/6/917/2013/.

Eastham, S. D., D. K. Weisenstein, and S. R. Barrett. 2014. "Development and evaluation of the unified tropospheric–stratospheric chemistry extension (UCX) for the global chemistry-transport model GEOS-Chem." *Atmospheric Environment* 89:52–63. doi:http://dx.doi.org/10.1016/j.atmosenv.2014.02.001. http://www.sciencedirect.com/science/article/pii/S1352231014000971.

Ehhalt, D. H. 1974. "The atmospheric cycle of methane." *Tellus* 26 (1-2): 58–70. doi:10.1111/j.2153-3490.1974.tb01952.x. http://dx.doi.org/10.1111/j.2153-3490.1974.tb01952.x.

Ehhalt, D. H., and U. Schmidt. 1978. "Sources and sinks of atmospheric methane." *pure and applied geophysics* 116 (2): 452–464. doi:10.1007/BF01636899. http://dx.doi.org/10.1007/BF01636899.

EIA. 2016. *International Energy Outlook 2016 (IEO2016)*. Report DOE/EIA-0484(2016). United States Energy Information Agency (US EIA). http://www.eia.gov/outlooks/ieo/pdf/0484(2016).pdf.

European Commission Joint Research Centre, Netherlands Environmental Assessment Agency. 2011. *Emission Database for Global Atmospheric Research (EDGAR)*. http://edgar.jrc.ec.europa.eu. Version 4.2. Available at http://edgar.jrc.ec.europa.eu.

Fiore, A. M., et al. 2008. "Characterizing the tropospheric ozone response to methane emission controls and the benefits to climate and air quality." *Journal of Geophysical Research: Atmospheres* 113 (D8).

Franco, B., et al. 2016. "Evaluating ethane and methane emissions associated with the development of oil and natural gas extraction in North America." *Environmental Research Letters* 11 (4): 044010. http://stacks.iop.org/1748-9326/11/i=4/a=044010.

Fraser, A., et al. 2011. "The Australian methane budget: Interpreting surface and train-borne measurements using a chemistry transport model." D20306, *Journal of Geophysical Research: Atmospheres* 116 (D20). doi:10.1029/2011JD015964. http://dx.doi.org/10.1029/2011JD015964.

Fraser, A., et al. 2013. "Estimating regional methane surface fluxes: the relative importance of surface and GOSAT mole fraction measurements." *Atmospheric Chemistry and Physics* 13 (11): 5697–5713. doi:10.5194/acp-13-5697-2013. http://www.atmos-chem-phys.net/13/5697/2013/.

Fraser, P. J., et al. 1981. "Trends of atmospheric methane in the southern hemisphere." *Geophysical Research Letters* 8 (10): 1063–1066. doi:10.1029/GL008i010p01063. http://dx.doi.org/10.1029/GL008i010p01063.

Fung, I., et al. 1991a. "Three-dimensional model synthesis of the global methane cycle." *Journal of Geophysical Research* 96 (D7): 13033–13065. doi:10.1029/91JD01247.

Fung, I., et al. 1991b. "Three-dimensional model synthesis of the global methane cycle." *Journal of Geophysical Research: Atmospheres* 96 (D7): 13033–13065.

Geibel, M. C., et al. 2012. "Calibration of column-averaged CH_4 over European TCCON FTS sites with airborne in-situ measurements." *Atmospheric Chemistry and Physics* 12 (18): 8763–8775. doi:10.5194/acp-12-8763-2012. http://www.atmos-chem-phys.net/12/8763/2012/.

Gentner, D. R., et al. 2014. "Emissions of organic carbon and methane from petroleum and dairy operations in California's San Joaquin Valley." *Atmospheric Chemistry and Physics* 14 (10): 4955–4978. doi:{10.5194/acp-14-4955-2014}.

Goldberg, L. 1951. "The Abundance and Vertical Distribution of Methane in the Earth's Atmosphere." *The Astrophysical Journal* 113 (): 567. doi:10.1086/145426.

Goldberg, L., and E. A. Müller. 1953. "The Vertical Distribution of Nitrous Oxide and Methane in the Earth's Atmosphere." *J. Opt. Soc. Am.* 43, no. 11 (): 1033–1036. doi:10.1364/JOSA.43.001033. http://www.osapublishing.org/abstract.cfm?URI=josa-43-11-1033.

Graedel, T. E., and J. E. McRae. 1980. "On the possible increase of the atmospheric methane and carbon monoxide concentrations during the last decade." *Geophysical Research Letters* 7 (11): 977–979. doi:10.1029/GL007i011p00977. http://dx.doi.org/10.1029/GL007i011p00977.

Griffith, D. W. T., et al. 2014a. *TCCON data from Darwin, Australia, Release GGG2014R0*. http://dx.doi.org/10.14291/tccon.ggg2014.darwin01.R0/1149290. doi:10.14291/tccon.ggg2014.darwin01.R0/1149290.

Griffith, D. W. T., et al. 2014b. *TCCON data from Wollongong, Australia, Release GGG2014R0*. http://dx.doi.org/10.14291/tccon.ggg2014.wollongong01.R0/1149291. doi:10.14291/tccon.ggg2014.wollongong01.R0/1149291.

Hartmann, D., et al. 2013. "Observations: Atmosphere and Surface." Chap. 2 in *Climate Change 2013: The Physical Science Basis. Contribution of Working Group I to the Fifth Assessment Report of the Intergovernmental Panel on Climate Change*, ed. by T. Stocker et al., 159–254. Cambridge, United Kingdom and New York, NY, USA: Cambridge University Press. doi:10.1017/CBO9781107415324.008. www.climatechange2013.org.

Hase, F., et al. 2014. *TCCON data from Karlsruhe, Germany, Release GGG2014R1*. http://dx.doi.org/10.14291/tccon.ggg2014.karlsruhe01.R1/1182416. doi:10.14291/tccon.ggg2014.karlsruhe01.R1/1182416.

Hoaglin, D. C., F. Mosteller, and J. W. Tukey. 1983. *Understanding robust and exploratory data analysis*. Vol. 3. Wiley New York.

Houweling, S., et al. 1999. "Inverse modeling of methane sources and sinks using the adjoint of a global transport model." *Journal of Geophysical Research: Atmospheres* 104 (D21): 26137–26160. doi:10.1029/1999JD900428. http://dx.doi.org/10.1029/1999JD900428.

Hsu, Y.-K., et al. 2010. "Methane emissions inventory verification in southern California." *Atmospheric Environment* 44 (1): 1–7.

Iraci, L., et al. 2014. *TCCON data from Armstrong Flight Research Center, Edwards, CA, USA, Release GGG2014R0*. http://dx.doi.org/10.14291/tccon.ggg2014.edwards01.R0/1149289. doi:10.14291/tccon.ggg2014.edwards01.R0/1149289.

Jones, A., et al. 2012. "Technical Note: A trace gas climatology derived from the Atmospheric Chemistry Experiment Fourier Transform Spectrometer (ACE-FTS) data set." *Atmospheric Chemistry and Physics* 12 (11): 5207–5220. doi:10.5194/acp-12-5207-2012. http://www.atmos-chem-phys.net/12/5207/2012/.

Kai, F. M., et al. 2011. "Reduced methane growth rate explained by decreased Northern Hemisphere microbial sources." *Nature* 476 (7359): 194–197. doi:10.1038/nature10259. %3CGo%20to%20ISI%3E://WOS:000293731900033.

Kalnay, E., et al. 1996. "The NCEP/NCAR 40-year reanalysis project." *Bulletin of the American Meteorological Society* 77 (3): 437–471.

Katzenstein, A. S., et al. 2003. "Extensive regional atmospheric hydrocarbon pollution in the southwestern United States." *Proceedings of the National Academy of Sciences* 100 (21): 11975–11979.

Kawakami, S., et al. 2014. *TCCON data from Saga, Japan, Release GGG2014R0*. http://dx.doi.org/10.14291/tccon.ggg2014.saga01.R0/1149283. doi:10.14291/tccon.ggg2014.saga01.R0/1149283.

Keller, C. A., et al. 2014. "HEMCO v1.0: a versatile, ESMF-compliant component for calculating emissions in atmospheric models." *Geoscientific Model Development* 7 (4): 1409–1417. doi:10.5194/gmd-7-1409-2014. http://www.geosci-model-dev.net/7/1409/2014/.

Keller, M., et al. 1983. "Production of nitrous oxide and consumption of methane by forest soils." *Geophysical Research Letters* 10 (12): 1156–1159. doi:10.1029/GL010i012p01156. http://dx.doi.org/10.1029/GL010i012p01156.

Keppel-Aleks, G., P. O. Wennberg, and T. Schneider. 2011. "Sources of variations in total column carbon dioxide." *Atmospheric Chemistry and Physics* 11, no. 8 (): 3581–3593. doi:10.5194/acp-11-3581-2011. http://www.atmos-chem-phys.net/11/3581/2011/.

Keppel-Aleks, G., et al. 2012. "The imprint of surface fluxes and transport on variations in total column carbon dioxide." *Biogeosciences* 9, no. 3 (): 875–891. doi:10.5194/bg-9-875-2012. http://www.biogeosciences.net/9/875/2012/.

Khalil, M. A. K., and R. A. Rasmussen. 1983. "Sources, sinks, and seasonal cycles of atmospheric methane." *Journal of Geophysical Research: Oceans* 88 (C9): 5131–5144. doi:10.1029/JC088iC09p05131. http://dx.doi.org/10.1029/JC088iC09p05131.

– . 1985. "Causes of increasing atmospheric methane: Depletion of hydroxyl radicals and the rise of emissions." *Atmospheric Environment (1967)* 19 (3): 397–407. doi:http://dx.doi.org/10.1016/0004-6981(85)90161-1.

Kim, H.-S., et al. 2015. "Decadal trends of atmospheric methane in East Asia from 1991 to 2013." *Air Quality, Atmosphere & Health* 8 (3): 293–298. doi:10.1007/s11869-015-0331-x. http://dx.doi.org/10.1007/s11869-015-0331-x.

Kirschke, S., et al. 2013. "Three decades of global methane sources and sinks." *Nature Geoscience* 6 (10): 813–823.

Kivi, R., P. Heikkinen, and E. Kyro. 2014. *TCCON data from Sodankyla, Finland, Release GGG2014R0*. http://dx.doi.org/10.14291/tccon.ggg2014.sodankyla01.R0/1149280. doi:10.14291/tccon.ggg2014.sodankyla01.R0/1149280.

Kley, D. 1997. "Tropospheric Chemistry and Transport." *Science* 276 (5315): 1043–1044. doi:10.1126/science.276.5315.1043. http://science.sciencemag.org/content/276/5315/1043.

Lamontagne, R. A., et al. 1973. "Methane concentrations in various marine environments." *Journal of Geophysical Research* 78 (24): 5317–5324. doi:10.1029/JC078i024p05317. http://dx.doi.org/10.1029/JC078i024p05317.

Levy, H. 1971. "Normal Atmosphere: Large Radical and Formaldehyde Concentrations Predicted." *Science* 173 (3992): 141–143. doi:10.1126/science.173.3992.141. http://science.sciencemag.org/content/173/3992/141.

Lovelock, J. E. 1977. "Methyl chloroform in the troposphere as an indicator of OH radical abundance." *Nature* 267 (5606): 32–32.

Lowe, D. C., et al. 1991. "Determination of the isotopic composition of atmospheric methane and its application in the Antarctic." *Journal of Geophysical Research* 96 (D8): 15455. doi:10.1029/91JD01119. http://doi.wiley.com/10.1029/91JD01119.

Luo, M., R. J. Cicerone, and J. M. Russell. 1995. "Analysis of Halogen Occultation Experiment HF versus CH4 correlation plots: Chemistry and transport implications." *Journal of Geophysical Research: Atmospheres* 100 (D7): 13927–13937. doi:10.1029/95JD00621. http://dx.doi.org/10.1029/95JD00621.

Luo, M., et al. 1994. "Observations of stratospheric hydrogen fluoride by halogen occultation experiment (HALOE)." *Journal of Geophysical Research* 99 (D8): 16691–16705.

MacFarling Meure, C., et al. 2006. "Law Dome CO2, CH4 and N2O ice core records extended to 2000 years BP." L14810, *Geophysical Research Letters* 33 (14). doi:10.1029/2006GL026152. http://dx.doi.org/10.1029/2006GL026152.

Mahieu, E., et al. 2008. "Validation of ACE-FTS v2.2 measurements of HCl, HF, CCl_3F and CCl_2F_2 using space-, balloon- and ground-based instrument observations." *Atmospheric Chemistry and Physics* 8 (20): 6199–6221. doi:10.5194/acp-8-6199-2008. http://www.atmos-chem-phys.net/8/6199/2008/.

Mayer, E. W., et al. 1982. "Methane: Interhemispheric concentration gradient and atmospheric residence time." *Proceedings of the National Academy of Sciences* 79 (4): 1366–1370. http://www.pnas.org/content/79/4/1366.abstract.

McMath, R. R., O. C. Mohler, and L. Goldberg. 1949. "Telluric Bands of CH_{4} in the Solar Spectrum." *The Astrophysical Journal* 109 (): 17. doi:10.1086/145100.

Messerschmidt, J., et al. 2010. "Side by side measurements of CO2 by ground-based Fourier transform spectrometry (FTS)." *Tellus B* 62 (5): 749–758.

Messerschmidt, J., et al. 2011. "Calibration of TCCON column-averaged CO_2: the first aircraft campaign over European TCCON sites." *Atmospheric Chemistry and Physics* 11 (21): 10765–10777. doi:10.5194/acp-11-10765-2011. http://www.atmos-chem-phys.net/11/10765/2011/.

Migeotte, M. V. 1948a. "Methane in the Earth's Atmosphere." *The Astrophysical Journal* 107 (): 400. doi:10.1086/145024.

Migeotte, M. V. 1948b. "Spectroscopic Evidence of Methane in the Earth's Atmosphere." *Phys. Rev.* 73 (5): 519–520. doi:10.1103/PhysRev.73.519.2. http://link.aps.org/doi/10.1103/PhysRev.73.519.2.

Montzka, S. A., et al. 2011. "Small interannual variability of global atmospheric hydroxyl." *Science* 331 (6013): 67–69. doi:10.1126/science.1197640.

Morino, I., T. Matsuzaki, and A. Shishime. 2014a. *TCCON data from Tsukuba, Ibaraki, Japan, 125HR, Release GGG2014R1*. http://dx.doi.org/10.14291/tccon.ggg2014.tsukuba02.R1/ doi:10.14291/tccon.ggg2014.tsukuba02.R1/1241486.

Morino, I., et al. 2014b. *TCCON data from Rikubetsu, Hokkaido, Japan, Release GGG2014R1*. http://dx.doi.org/10.14291/tccon.ggg2014.rikubetsu01.R1/1242265. doi:10.14291/tccon.ggg2014.rikubetsu01.R1/1242265.

Mote, P. W., et al. 1996. "An atmospheric tape recorder: The imprint of tropical tropopause temperatures on stratospheric water vapor." *Journal of Geophysical Research: Atmospheres* 101 (D2): 3989–4006. doi:10.1029/95JD03422. http://dx.doi.org/10.1029/95JD03422.

Mu, M., et al. 2011. "Daily and 3-hourly variability in global fire emissions and consequences for atmospheric model predictions of carbon monoxide." D24303, *Journal of Geophysical Research: Atmospheres* 116 (D24). doi:10.1029/2011JD016245. http://dx.doi.org/10.1029/2011JD016245.

Murray, L. T., et al. 2012. "Optimized regional and interannual variability of lightning in a global chemical transport model constrained by LIS/OTD satellite data." D20307, *Journal of Geophysical Research: Atmospheres* 117 (D20). doi:10.1029/2012JD017934. http://dx.doi.org/10.1029/2012JD017934.

Myhre, G., et al. 2013. "Anthropogenic and Natural Radiative Forcing." Chap. 8 in *Climate Change 2013: The Physical Science Basis. Contribution of Working Group I to the Fifth Assessment Report of the Intergovernmental Panel on Climate Change*, ed. by T. Stocker et al., 659–740. Cambridge, United Kingdom and New York, NY, USA: Cambridge University Press. doi:10.1017/CBO9781107415324.018. www.climatechange2013.org.

Nisbet, E. G., et al. 2016. "Rising atmospheric methane: 2007–2014 growth and isotopic shift." *Global Biogeochemical Cycles* 30 (9): 1356–1370. doi:10.1002/2016GB005406. http://dx.doi.org/10.1002/2016GB005406.

Nisbet, E. G., E. J. Dlugokencky, and P. Bousquet. 2014. "Methane on the Rise—Again." *Science* 343:493–495. doi:10.1126/science.1247828.

Notholt, J., et al. 2014. *TCCON data from Bremen, Germany, Release GGG2014R0*. http://dx.doi.org/10.14291/tccon.ggg2014.bremen01.R0/1149275. doi:10.14291/tccon.ggg2014.bremen01.R0/1149275.

Ostler, A., et al. 2014. "Multistation intercomparison of column-averaged methane from NDACC and TCCON: impact of dynamical variability." *Atmospheric Measurement Techniques* 7 (12): 4081–4101. doi:10.5194/amt-7-4081-2014. http://www.atmos-meas-tech.net/7/4081/2014/.

Ostler, A., et al. 2016. "Evaluation of column-averaged methane in models and TCCON with a focus on the stratosphere." *Atmospheric Measurement Techniques* 9 (9): 4843–4859. doi:10.5194/amt-9-4843-2016. http://www.atmos-meas-tech.net/9/4843/2016/.

Park, R. J., et al. 2004. "Natural and transboundary pollution influences on sulfate-nitrate-ammonium aerosols in the United States: Implications for policy." D15204, *Journal of Geophysical Research: Atmospheres* 109 (D15). doi:10.1029/2003JD004473. http://dx.doi.org/10.1029/2003JD004473.

Parker, R., et al. 2011. "Methane observations from the Greenhouse Gases Observing SATellite: Comparison to ground-based TCCON data and model calculations." L15807, *Geophysical Research Letters* 38 (15). doi:10.1029/2011GL047871. http://dx.doi.org/10.1029/2011GL047871.

Patra, P. K., et al. 2011. "TransCom model simulations of CH_4 and related species: linking transport, surface flux and chemical loss with CH_4 variability in the troposphere and lower stratosphere." *Atmospheric Chemistry and Physics* 11 (24): 12813–12837. doi:10.5194/acp-11-12813-2011. http://www.atmos-chem-phys.net/11/12813/2011/.

Patra, P. K., et al. 2014. "Observational evidence for interhemispheric hydroxyl-radical parity." *Nature* 513 (7517): 219–223.

Payne, V. H., et al. 2009. "Information-centered representation of retrievals with limited degrees of freedom for signal: Application to methane from the Tropospheric Emission Spectrometer." *Journal of Geophysical Research* 114, no. D10 (): D10307. doi:10.1029/2008JD010155. http://doi.wiley.com/10.1029/2008JD010155.

Peischl, J., et al. 2016. "Quantifying atmospheric methane emissions from oil and natural gas production in the Bakken shale region of North Dakota." *Journal of Geophysical Research: Atmospheres* 121 (10): 6101–6111.

Pickett-Heaps, C. A., et al. 2011. "Magnitude and seasonality of wetland methane emissions from the Hudson Bay Lowlands (Canada)." *Atmospheric Chemistry and Physics* 11 (8): 3773–3779. doi:10.5194/acp-11-3773-2011. http://www.atmos-chem-phys.net/11/3773/2011/.

Pison, I., et al. 2013. "Stable atmospheric methane in the 2000s: key-role of emissions from natural wetlands." *Atmospheric Chemistry and Physics* 13, no. 23 (): 11609–11623. doi:10.5194/acp-13-11609-2013. http://www.atmos-chem-phys.net/13/11609/2013/.

Prather, M. J. 2007. "Lifetimes and time scales in atmospheric chemistry." *Philosophical Transactions of the Royal Society of London A: Mathematical, Physical and Engineering Sciences* 365 (1856): 1705–1726. doi:10.1098/rsta.2007.2040. http://rsta.royalsocietypublishing.org/content/365/1856/1705.

Prather, M. J., C. D. Holmes, and J. Hsu. 2012. "Reactive greenhouse gas scenarios: Systematic exploration of uncertainties and the role of atmospheric chemistry." *Geophysical Research Letters* 39, no. 9 (). doi:10.1029/2012GL051440. http://doi.wiley.com/10.1029/2012GL051440.

Rasmussen, R. A., and M. A. K. Khalil. 1981a. "Atmospheric methane (CH4): Trends and seasonal cycles." *Journal of Geophysical Research: Oceans* 86 (C10): 9826–9832. doi:10.1029/JC086iC10p09826. http://dx.doi.org/10.1029/JC086iC10p09826.

– . 1984. "Atmospheric methane in the recent and ancient atmospheres: Concentrations, trends, and interhemispheric gradient." *Journal of Geophysical Research: Atmospheres* 89 (D7): 11599–11605. doi:10.1029/JD089iD07p11599. http://dx.doi.org/10.1029/JD089iD07p11599.

Rasmussen, R., and M. Khalil. 1981b. "Increase in the concentration of atmospheric methane." *Atmospheric Environment (1967)* 15 (5): 883–886. doi:http://dx.doi.org/10.1016/0004-6981(81)90298-5. http://www.sciencedirect.com/science/article/pii/0004698181902985.

Rasmussen, R., and M. Khalil. 1983. "Global production of methane by termites." *Nature* 301:700–702.

Rigby, M., et al. 2017. "Role of atmospheric oxidation in recent methane growth." *Proceedings of the National Academy of Sciences*. doi:10.1073/pnas.1616426114. http://www.pnas.org/content/early/2017/04/11/1616426114.abstract.

Rigby, M., et al. 2008. "Renewed growth of atmospheric methane." *Geophysical Research Letters* 35 (22). doi:10.1029/2008GL036037.

Ringeval, B., et al. 2010. "An attempt to quantify the impact of changes in wetland extent on methane emissions on the seasonal and interannual time scales." *Global Biogeochemical Cycles* 24 (2).

Rodgers, C. D., and B. J. Connor. 2003. "Intercomparison of remote sounding instruments." *Journal of Geophysical Research* 108:4116. doi:10.1029/2002JD002299.

Saad, K. M., et al. 2014. "Derivation of tropospheric methane from TCCON CH_4 and HF total column observations." *Atmospheric Measurement Techniques* 7 (9): 2907–2918. doi:10.5194/amt-7-2907-2014. http://www.atmos-meas-tech.net/7/2907/2014/.

Saad, K. M., et al. 2016. "Seasonal variability of stratospheric methane: implications for constraining tropospheric methane budgets using total column observations." *Atmospheric Chemistry and Physics* 16 (21): 14003–14024. doi:10.5194/acp-16-14003-2016. http://www.atmos-chem-phys.net/16/14003/2016/.

Santoni, G. W., et al. 2014. "Evaluation of the airborne quantum cascade laser spectrometer (QCLS) measurements of the carbon and greenhouse gas suite - CO2, CH4, N2O, and CO - during the CalNex and HIPPO campaigns." *Atmospheric Measurement Techniques* 7 (6): 1509–1526. doi:{10.5194/amt-7-1509-2014}.

Saunois, M., et al. 2016. "The growing role of methane in anthropogenic climate change." *Environmental Research Letters* 11 (12): 120207. http://stacks.iop.org/1748-9326/11/i=12/a=120207.

Schaefer, H., et al. 2016. "A 21st-century shift from fossil-fuel to biogenic methane emissions indicated by 13CH4." *Science* 352 (6281): 80–84. doi:10.1126/science.aad2705. http://science.sciencemag.org/content/352/6281/80.

Schneising, O., et al. 2014. "Remote sensing of fugitive methane emissions from oil and gas production in North American tight geologic formations." *Earth's Future* 2 (10): 548–558.

Schwietzke, S., et al. 2016. "Upward revision of global fossil fuel methane emissions based on isotope database." *Nature* 538 (7623): 88–91.

Sepúlveda, E., et al. 2012. "Long-term validation of tropospheric column-averaged CH_4 mole fractions obtained by mid-infrared ground-based FTIR spectrometry." *Atmospheric Measurement Techniques* 5, no. 6 (): 1425–1441. doi:10.5194/amt-5-1425-2012. http://www.atmos-meas-tech.net/5/1425/2012/amt-5-1425-2012.html.

Sepúlveda, E., et al. 2014. "Tropospheric CH_4 signals as observed by NDACC FTIR at globally distributed sites and comparison to GAW surface in situ measurements." *Atmospheric Measurement Techniques* 7 (7): 2337–2360. doi:10.5194/amt-7-2337-2014. http://www.atmos-meas-tech.net/7/2337/2014/.

Sheese, P. E., C. D. Boone, and K. A. Walker. 2015. "Detecting physically unrealistic outliers in ACE-FTS atmospheric measurements." *Atmospheric Measurement Techniques* 8 (2): 741–750. doi:10.5194/amt-8-741-2015. http://www.atmos-meas-tech.net/8/741/2015/.

Sherlock, V., et al. 2014a. *TCCON data from Lauder, New Zealand, 120HR, Release GGG2014R0*. http://dx.doi.org/10.14291/tccon.ggg2014.lauder01.R0/1149293. doi:10.14291/tccon.ggg2014.lauder01.R0/1149293.

– . 2014b. *TCCON data from Lauder, New Zealand, 125HR, Release GGG2014R0*. http://dx.doi.org/10.14291/tccon.ggg2014.lauder02.R0/1149298. doi:10.14291/tccon.ggg2014.lauder02.R0/1149298.

Shindell, D. T., et al. 2009. "Improved Attribution of Climate Forcing to Emissions." *Science* 326 (5953): 716–718. doi:10.1126/science.1174760. http://www.sciencemag.org/content/326/5953/716.abstract.

Simpson, I. J., et al. 2002. "Implications of the recent fluctuations in the growth rate of tropospheric methane." *Geophysical Research Letters* 29 (10): 117-1–117-4. doi:10.1029/2001GL014521. http://dx.doi.org/10.1029/2001GL014521.

Singh, S., K. Kulshreshtha, and S. Agnihotri. 2000. "Seasonal dynamics of methane emission from wetlands." *Chemosphere - Global Change Science* 2 (1): 39–46. doi:http://dx.doi.org/10.1016/S1465-9972(99)00046-X. http://www.sciencedirect.com/science/article/pii/S146599729900046X.

Smith, L. K., and W. M. Lewis. 1992. "Seasonality of methane emissions from five lakes and associated wetlands of the Colorado Rockies." *Global Biogeochemical Cycles* 6 (4): 323–338.

Stephens, B. B., et al. 2007. "Weak Northern and Strong Tropical Land Carbon Uptake from Vertical Profiles of Atmospheric CO2." *Science* 316 (5832): 1732–1735. doi:10.1126/science.1137004. http://science.sciencemag.org/content/316/5832/1732.

Strong, K., et al. 2014. *TCCON data from Eureka, Canada, Release GGG2014R0*. http://dx.doi.org/10.14291/tccon.ggg2014.eureka01.R0/1149271. doi:10.14291/tccon.ggg2014.eureka01.R0/1149271.

Sussmann, R., and M. Rettinger. 2014. *TCCON data from Garmisch, Germany, Release GGG2014R0*. http://dx.doi.org/10.14291/tccon.ggg2014.garmisch01.R0/1149299. doi:10.14291/tccon.ggg2014.garmisch01.R0/1149299.

Sussmann, R., et al. 2012. "Renewed methane increase for five years (2007–2011) observed by solar FTIR spectrometry." *Atmospheric Chemistry and Physics* 12 (11): 4885–4891. doi:10.5194/acp-12-4885-2012. http://www.atmos-chem-phys.net/12/4885/2012/.

Sutherland, G. B. B. M., and G. S. Callendar. 1942. "The infra-red spectra of atmospheric gases other than water vapour." *Reports on Progress in Physics* 9 (1): 18. http://stacks.iop.org/0034-4885/9/i=1/a=304.

Takeuchi, W., M. Tamura, and Y. Yasuoka. 2003. "Estimation of methane emission from West Siberian wetland by scaling technique between {NOAA} {AVHRR} and {SPOT} {HRV}." *Remote Sensing of Environment* 85 (1): 21–29. doi:http://dx.doi.org/10.1016/S0034-4257(02)00183-9. http://www.sciencedirect.com/science/article/pii/S0034425702001839.

Thompson, R. L., et al. 2015. "Methane emissions in East Asia for 2000–2011 estimated using an atmospheric Bayesian inversion." 2014JD022394, *Journal of Geophysical Research: Atmospheres* 120 (9): 4352–4369. doi:10.1002/2014JD022394. http://dx.doi.org/10.1002/2014JD022394.

Toon, G. C., and D. Wunch. 2014. *A stand-alone a priori profile generation tool for GGG2014*. http://dx.doi.org/10.14291/tccon.ggg2014.priors.R0/1221661. Pasadena. doi:10.14291/tccon.ggg2014.priors.R0/1221661.

Turner, A. J., et al. 2015. "Estimating global and North American methane emissions with high spatial resolution using GOSAT satellite data." *Atmospheric Chemistry and Physics* 15 (12): 7049–7069. doi:10.5194/acp-15-7049-2015. http://www.atmos-chem-phys.net/15/7049/2015/.

Turner, A. J., et al. 2016. "A large increase in US methane emissions over the past decade inferred from satellite data and surface observations." *Geophysical Research Letters*.

Turner, A. J., et al. 2017. "Ambiguity in the causes for decadal trends in atmospheric methane and hydroxyl." *Proceedings of the National Academy of Sciences*. doi:10.1073/pnas.1616020114. http://www.pnas.org/content/early/2017/04/18/1616020114.abstract.

Tyler, S. C., D. R. Blake, and F. S. Rowland. 1987. "13C/12C ratio in methane from the flooded Amazon forest." *Journal of Geophysical Research: Atmospheres* 92 (D1): 1044–1048. doi:10.1029/JD092iD01p01044. http://dx.doi.org/10.1029/JD092iD01p01044.

Vaghjiani, G. L., and A. R. Ravishankara. 1991. "New Measurement of the Rate Coefficient of the Reaction of OH with Methane." *Nature* 350, no. 6317 (): 406.

Wang, J., et al. 2004. "A 3-D model analysis of the slowdown and interannual variability in the methane growth rate from 1988 to 1997." *GLOBAL BIOGEOCHEMICAL CYCLES* 18, no. 3 (). doi:10.1029/2003GB002180.

Wang, Z., D. Zeng, and W. H. Patrick. 1996. "Methane emissions from natural wetlands." *Environmental Monitoring and Assessment* 42 (1): 143–161.

Wang, Z., et al. 2014. "Retrieval of tropospheric column-averaged CH_4 mole fraction by solar absorption FTIR-spectrometry using N_2O as a proxy." *Atmospheric Measurement Techniques* 7 (10): 3295–3305. doi:10.5194/amt-7-3295-2014. http://www.atmos-meas-tech.net/7/3295/2014/.

Warneke, T., et al. 2014. *TCCON data from Orleans, France, Release GGG2014R0*. http://dx.doi.org/10.14291/tccon.ggg2014.orleans01.R0/1149276. doi:10.14291/tccon.ggg2014.orleans01.R0/1149276.

Washenfelder, R. A., P. O. Wennberg, and G. C. Toon. 2003. "Tropospheric methane retrieved from ground-based near-IR solar absorption spectra." *Geophysical Research Letters* 30 (23): 2226. doi:10.1029/2003GL017969. http://doi.wiley.com/10.1029/2003GL017969%20http://dx.doi.org/10.1029/2003GL017969.

Washenfelder, R. A., et al. 2006. "Carbon dioxide column abundances at the Wisconsin Tall Tower site." *Journal of Geophysical Research: Atmospheres* 111 (D22): D22305. doi:10.1029/2006JD007154. http://dx.doi.org/10.1029/2006JD007154.

Waugh, D., and T. Hall. 2002. "Age of Stratospheric Air: Theory, Observations, and Models." 1010, *Reviews of Geophysics* 40 (4): 1-1–1-26. doi:10.1029/2000RG000101. http://dx.doi.org/10.1029/2000RG000101.

Waymark, C., et al. 2014. "ACE-FTS version 3.0 data set: validation and data processing update." *Annals of Geophysics* 56 (0). http://www.annalsofgeophysics.eu/index.php/annals/article/view/6339.

Wecht, K. J., et al. 2014a. "Spatially resolving methane emissions in California: constraints from the CalNex aircraft campaign and from present (GOSAT, TES) and future (TROPOMI, geostationary) satellite observations." *Atmospheric Chemistry and Physics* 14 (15): 8173–8184. doi:10.5194/acp-14-8173-2014. http://www.atmos-chem-phys.net/14/8173/2014/.

Wecht, K. J., et al. 2014b. "Mapping of North American methane emissions with high spatial resolution by inversion of SCIAMACHY satellite data." 2014JD021551, *Journal of Geophysical Research: Atmospheres* 119 (12): 7741–7756. doi:10.1002/2014JD021551. http://dx.doi.org/10.1002/2014JD021551.

Wennberg, P. O., et al. 2012. "On the Sources of Methane to the Los Angeles Atmosphere." *Environmental Science & Technology* 46 (17): 9282–9289. doi:10.1021/es301138y. http://dx.doi.org/10.1021/es301138y.

Wennberg, P. O., et al. 2014a. *TCCON data from Jet Propulsion Laboratory, Pasadena, California, USA, Release GGG2014R0*. http://dx.doi.org/10.14291/tccon.ggg2014.jpl01.R0/1 doi:10.14291/tccon.ggg2014.jpl01.R0/1149163.

Wennberg, P. O., et al. 2014b. *TCCON data from Jet Propulsion Laboratory, Pasadena, California, USA, Release GGG2014R0*. http://dx.doi.org/10.14291/tccon.ggg2014.jpl02.R0/1 doi:10.14291/tccon.ggg2014.jpl02.R0/1149297.

Wennberg, P. O., et al. 2014c. *TCCON data from Lamont, Oklahoma, USA, Release GGG2014R0*. http://dx.doi.org/10.14291/tccon.ggg2014.lamont01.R0/1149159. doi:10.14291/tccon.ggg2014.lamont01.R0/1149159.

Wennberg, P. O., et al. 2014d. *TCCON data from Park Falls, Wisconsin, USA, Release GGG2014R0*. http://dx.doi.org/10.14291/tccon.ggg2014.parkfalls01.R0/1149161. doi:10.14291/tccon.ggg2014.parkfalls01.R0/1149161.

Wennberg, P. O., et al. 2014e. *TCCON data from California Institute of Technology, Pasadena, California, USA, Release GGG2014R1*. http://dx.doi.org/10.14291/tccon.ggg2014.pasadena0 doi:10.14291/tccon.ggg2014.pasadena01.R1/1182415.

Werf, G. R. van der, et al. 2010. "Global fire emissions and the contribution of deforestation, savanna, forest, agricultural, and peat fires (1997-2009)." *Atmospheric Chemistry and Physics* 10 (23): 11707–11735. doi:10.5194/acp-10-11707-2010. http://www.atmos-chem-phys.net/10/11707/2010/.

Whiting, G. J., and J. P. Chanton. 1993. "Primary production control of methane emission from wetlands." *Nature* 364:794.

Wilson, J. O., et al. 1989. "Seasonal variation of methane emissions from a temperate swamp." *Biogeochemistry* 8 (1): 55–71.

Wofsy, S. C. 1976. "Interactions of CH4 and CO in the Earth's atmosphere." *Annual Review of Earth and Planetary Sciences* 4 (1): 441–469.

Wunch, D., et al. 2011a. "The Total Carbon Column Observing Network." *Philosophical transactions. Series A, Mathematical, physical, and engineering sciences* 369, no. 1943 (): 2087–2112. doi:10.1098/rsta.2010.0240. http://www.ncbi.nlm.nih.gov/pubmed/21502178.

Wunch, D., et al. 2015. *The Total Carbon Column Observing Network's GGG2014 Data Version*. Tech. rep. Carbon Dioxide Information Analysis Center, Oak Ridge National Laboratory, Oak Ridge, Tennessee, U.S.A. doi: 10.14291/tccon.ggg2014.documentation.R0/1221662. doi:10.14291/tccon.ggg2014.documentation.R0/1221662. http://dx.doi.org/10.14291/tccon.ggg2014.documentation.R0/1221662.

Wunch, D., et al. 2009. "Emissions of greenhouse gases from a North American megacity." *Geophysical Research Letters* 36 (15): L15810. doi:10.1029/2009GL039825. http://dx.doi.org/10.1029/2009GL039825.

Wunch, D., et al. 2010. "Calibration of the Total Carbon Column Observing Network using aircraft profile data." *Atmospheric Measurement Techniques* 3, no. 5 (): 1351–1362. doi:10.5194/amt-3-1351-2010. http://www.atmos-meas-tech.net/3/1351/2010/.

Wunch, D., et al. 2011b. "A method for evaluating bias in global measurements of CO2 total columns from space." *Atmospheric Chemistry and Physics* 11, no. 23 (): 12317–12337. doi:10.5194/acp-11-12317-2011. http://www.atmos-chem-phys.net/11/12317/2011/acp-11-12317-2011.html.

Wunch, D., et al. 2016. "Quantifying the loss of processed natural gas within California's South Coast Air Basin using long-term measurements of ethane and methane." *Atmospheric Chemistry and Physics* 16 (22): 14091–14105. doi:10.5194/acp-16-14091-2016. http://www.atmos-chem-phys.net/16/14091/2016/.

Xiao, Y., D. J. Jacob, and S. Turquety. 2007. "Atmospheric acetylene and its relationship with CO as an indicator of air mass age." *Journal of Geophysical Research: Atmospheres* 112:D12305. doi:10.1029/2006JD008268. http://dx.doi.org/10.1029/2006JD008268.

Xiao, Y., et al. 2008. "Global budget of ethane and regional constraints on U.S. sources." *J. Geophys. Res.* 113, no. D21 (): D21306. doi:10.1029/2007JD009415. http://doi.wiley.com/10.1029/2007JD009415.

Yang, Z., et al. 2007. "New constraints on Northern Hemisphere growing season net flux." *Geophysical Research Letters* 34, no. 12 (): L12807. doi:10.1029/2007GL029742. http://doi.wiley.com/10.1029/2007GL029742.

York, D., et al. 2004. "Unified equations for the slope, intercept, and standard errors of the best straight line." *American Journal of Physics* 72, no. 3 (): 367. doi:10.1119/1.1632486. http://adsabs.harvard.edu/abs/2004AmJPh..72..367Y.